Jorge A. Robles
October 2011
Physics

Z boson measurement in the dimuon channel in PbPb collisions with the CMS experiment

Abstract

The unprecedented center of mass energy available at the LHC offers unique opportunities for studying the properties of the strongly-interacting QCD matter created in PbPb collisions at extreme temperatures and very low parton momentum fractions. With its high precision, large acceptance for tracking, and a trigger scheme that allows analysis of each minimum-bias PbPb events. CMS is especially suited to measure high-p_T dimuons, even in the high multiplicity environment of heavy-ion collisions. The Z boson is cleanly reconstructed in the dimuon channel. Such probes are especially relevant for these studies since they are produced at early times and propagate through the medium, mapping its evolution. Precise measurements of Z production in heavy-ion collisions can help to constrain nuclear PDFs as well as serve as a standard candle of the initial state in PbPb collisions at the LHC energies. From the PbPb run at at a $\sqrt{s} = 2.76$ TeV, the inclusive and differential measurements of the Z boson yield in the muon decay channel are presented. Making used of the pp reference run at the same center-of-mass energy, the nuclear modification factor, R_{AA}, is calculated. The value of the $R_{AA} = 1.03 \pm 25\%(stat)[+4.0\%, -5.0\%](syst)$ is found to be consistent with the expectation that no modification is observed with respect to next-to-leading order pQCD calculations, scaled by the number of incoherent

nucleon-nucleon collisions

Manuel Calderón de la Barca Sánchez, PhD
Dissertation Committee Chair

Z boson measurement in the dimuon channel in PbPb collisions with the CMS experiment

By

JORGE A. ROBLES
M.S (University of California at Davis)

DISSERTATION

Submitted in partial satisfaction of the requirements for the degree of

DOCTOR OF PHILOSOPHY

in

Physics

in the

OFFICE OF GRADUATE STUDIES

of the

UNIVERSITY OF CALIFORNIA

DAVIS

Approved:

Dr. Daniel Cebra

Dr. Ramona Vogt

2011

xxxx

Acknowledgments

xxxxxxx

Contents

List of Figures

List of Tables

Abstract

The unprecedented center of mass energy available at the LHC offers unique opportunities for studying the properties of the strongly-interacting QCD matter created in PbPb collisions at extreme temperatures and very low parton momentum fractions. With its high precision, large acceptance for tracking, and a trigger scheme that allows analysis of each minimum-bias PbPb events. CMS is especially suited to measure high-p_T dimuons, even in the high multiplicity environment of heavy-ion collisions. The Z boson is cleanly reconstructed in the dimuon channel. Such probes are especially relevant for these studies since they are produced at early times and propagate through the medium, mapping its evolution. Precise measurements of Z production in heavy-ion collisions can help to constrain nuclear PDFs as well as serve as a standard candle of the initial state in PbPb collisions at the LHC energies. From the PbPb run at at a $\sqrt{s} = 2.76$ TeV, the inclusive and differential measurements of the Z boson yield in the muon decay channel are presented. Making used of the pp reference run at the same center-of-mass energy, the nuclear modification factor, R_{AA}, is calculated. The value of the $R_{AA} = 1.03 \pm 25\%(stat)[+4.0\%, -5.0\%](syst)$ is found to be consistent with the expectation that no modification is observed with respect to next-to-leading order pQCD calculations, scaled by the number of incoherent nucleon-nucleon collisions

Chapter 1

Introduction

Heavy-Ion collisions are most promising way to study the Quark Gluon Plasma (QGP). At the center stage of the measurements in Heavy-Ion collisions are the modification suffered by probes that traverse the QGP. From the modifications suffered by these probes, qualities of the QGP can be inferred. The hot-dense-colored plasma created in Heavy-Ion collisions is not present in *pp* collisions. Thus, a comparison of the observables in these two systems, using *pp* as a baseline, provides with information about the QGP. From the relative modifications observed qualitative and quantitative statements about the hot medium can be made. Such effects can be the observed 'jet-quenching' in central Heavy-Ion collisions or quarkonium dissociation in Heavy-Ion collisions. These measurements are done using a statistical approach. A sample of events in Heavy-Ion collisions is compared to an equivalent sample of events in *pp* collisions. Form the statistical differences a physical observable is deduced. A better approach would be to study the effects in the same event as a 'control' probe is observed. In order to study the effects of a hot-dense-colored medium created in Heavy-Ion collisions, the control probe would need to be insensitive to it. Before the start of the Heavy-Ion program at the Large Hadron Collider (LHC), direct photons played that role. Photons traverse the medium unaffected by the QGP. However, great challenges must be faced to extract a clean direct photon signal from a high multiplicity environment. A γ-tagged jet approach also shows a promising future, but must deal with some of the same issues as the direct photons.

With the leap in center-of-mass in energy with respect to the one achieved by the Relativistic Heavy Ion Collider (RHIC), the LHC can provide enough energy to reach the electroweak scale in Heavy-Ion collisions. With this, a new set of probes are at hand. The Z^0 emerges as the obvious candidate to act as a control probe. The Z^0 being a weak boson does not interact with the QGP. CMS, an experiment designed to reconstruct high-p_T probes is especially suited for muons, making the Z $\rightarrow \mu^+\mu^-$ decay channel an easy choice to be used as a control probe. It is expected that neither the Z^0 boson, nor the decay muons interact with the hot medium. However, cold nuclear matter (CNM) effects are expected to account for smaller deviations. It is the purpose of this thesis to measure the yields of the Z $\rightarrow \mu^+\mu^-$ channel in $PbPb$ collisions at $\sqrt{s_{NN}} = 2.76$ TeV and compare them to the yields obtained from a pp reference sample at the same center-of mass energy.

The outline of this thesis is as follows: Chapter two describes the theoretical background relevant to this thesis topic. A brief overview of the standard model, signatures of the QGP and electroweak probes in Heavy-Ion collisions are discussed. Chapter three briefly describes the the LHC apparatus and outlines the relevant geometry of the CMS detector. Specific sub-detectors, relevant to this measurement, are described. In chapter four, a description of the simulation and MC sample used is given. A description of the Heavy-Ion reconstruction algorithms is included. An overview of the Monte Carlo matching and data-driven methods to calculate efficiencies is also included. Chapter five describes the detail of the Heavy-Ion setup adopted by CMS and the selections (online and offline) used to select the data sample used for this analysis. Chapter six includes the results from the $PbPb$ run as well as the pp from the reference run. The final systematic uncertainties are discussed along with the obtained yields compared to the relevant theoretical models. Using the pp reference run, the nuclear modification factor, R_{AA} was calculated. The result is compared to the available models.

Chapter 2

Theory Overview

2.1 Standard Model

The current understanding of the forces that describe the interactions of particles and fields is known as the standard model (SM). The strong, weak and electromagnetic interactions are understood as arising due to the exchange of various spin-one bosons amongst the spin-half particles that make up the matter. In other words, the SM is composed of particles that arise from excitations of the different fields, and force carriers that mediate the interaction between particles. Gravity is not yet included in our 'standard' model. Efforts are geared towards achieving a Theory of Everything (ToE) that would include all the known forces to the moment. Figure 2.1 shows a schematic of the particles that compose our understanding at the elementary level. Elementary particles can be identified by a set of quantum numbers, such as mass, charge, color, flavor. Spin is an intrinsic property that adds an extra degree of freedom to the set of quantum numbers that define a particle. Spin-1/2 particles are known as fermions. In the SM, these fermions can be either leptons or quarks. Leptons and quarks come in three generations. A total of six different quarks are known to the moment, the six different species are known as 'flavors', and are up (u), down (d), charm (c), strange (s), top (t) and bottom (b) and their anti-particles. The leptons are, electron (e), muon (μ), tau (τ) and electron neutrino (ν_e), muon neutrino (ν_μ) and tau neutrino (ν_τ), all these with the anti-particle counter part. The spin-1 particles that compose the SM are force mediators for the electromagnetic force, the photon (γ); the weak force, $W^{\pm}/Z$ bosons; and the strong force, the gluon (g). Not listed, but predicted and sought after, is the Higgs boson (H^0) to complete the picture of the SM. From the interactions with the Higgs field arise the mass of the particles. The standard model is one of the most significant achievements of the physics community. Since 1978 it has met every experimental test.

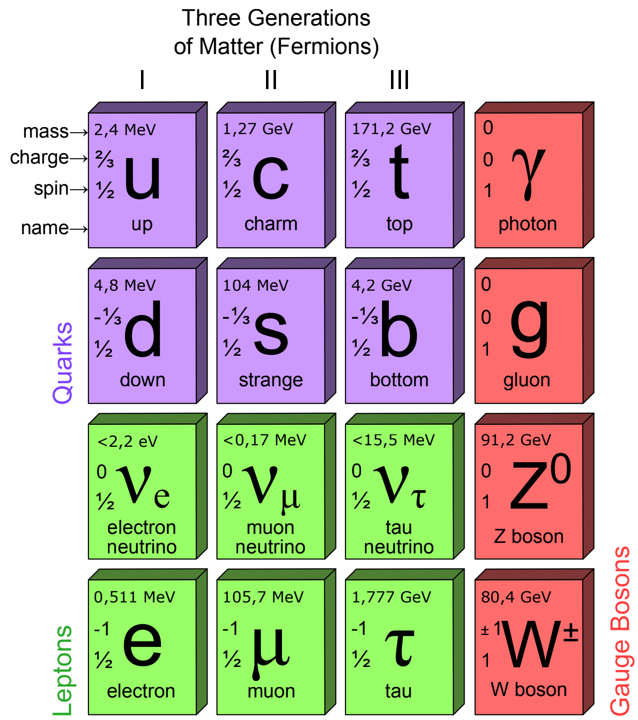

Figure 2.1: Elementary particles of the standard model

2.2 Electroweak Theory

The phenomena of electromagnetism formulated as a quantum field theory is known as Quantum ElectroDynamics (QED). QED describes how light and matter interact, it describes all phenomena involving the electrically charged particles interacting by means of the exchange of photons. The strength of electromagnetic interactions is given by the fine structure constant, $\alpha = e^2/4\pi\epsilon_0\hbar c$. The main characteristic of this interaction is that the force decreases as $1/r^2$, where r is the distance between electrically charged particles.

The weak interaction is the 'weakest' force of the ones included in the SM. It is caused by the exchange of massive W and Z bosons, the large mass of the gauge bosons accounts for the short range of the interaction. This force is responsible for the radioactive decay of subatomic particles. Its unique property is that it induces flavor changing currents. This allows quarks to swap their *flavors*. The weak interaction is the only one that violates parity symmetry and charge-parity symmetry. Parity symmetry refers to the property of particles to reman the same after a sign flip in the spatial dimensions.

The idea of an unified description of the electromagnetic and weak forces was first suggested by Glashow in 1961. The first evidence that would support the existence of these processes came in 1973 in the Gargamelle [2] bubble experiment at CERN, culminating with the discovery of the W and Z bosons in 1983 [3, 4] in the Supper Proton Anti-Proton Synchrotron ($Sp\bar{p}S$). These massive bosons are described by a SU(2) gauge theory, but they should be massless under a gauge theory. Such is the case of the photon which is described by a U(1) gauge theory.

The unification of the the weak force and electromagnetic was under $\mathrm{SU}(2)_L \otimes \mathrm{U}(1)_Y$ gauge group. In general, the SU(2) denotes a group of unitary 2×2 matrices with determinant 1. In general a SU(n) group has n^2 -1 free parameters with n^2 -1 generators. The SU(2) symmetry is connected to the conservation of a charge called weak-isospin (analogous to the isospin but it applies to quarks, leptons and electroweak bosons instead of hadrons). There are 3 spin-one bosons associated with this group, and one with a factor $U_Y(1)$, where Y denotes the hypercharge. The four bosons associated with $\mathrm{SU}(2)_L \otimes \mathrm{U}(1)_Y$ are related with the $W^{\pm}$ and Z^0 (after spontaneous symmetry braking), and the photon from QED. The $\mathrm{U}(1)_Y$ is the group of unitary 1-dimensional matrices. It stands for the space-time dependent rotation in a complex plane so that the multiplication of the state equation of a particle by a member of this group produces a phase change. The invariance under phase changes leads to the conservation of weak hypercharge Y. Y is the generator of the U(1) group.

In the 90's, experiments at the LEP and SLC colliders based their programs around the exploration of the Z resonance. Precision studies were carried out at the 0.1% level of the mass of the Z, M_Z, its line-shape and its branching ratios [5]. The second phase of the LEP program moved towards the exploration of the $W^{\pm}$ bosons. Given the the energy regime and the performance of the accelerator, the LEP apparatus was able to deliver thousands of Z events to each of the four experiments, which earned it the name: "Z factory" [6]. The center-of-mass milestone reached with the available technology at the time had opened a new door towards precision measurements of electroweak processes.

The production of electroweak probes in hadron colliders comes mainly from $q\bar{q} \rightarrow Z^0$ and $q\bar{q}' \rightarrow$ W. These processes are sensitive the quarks' parton distribution functions (PDF) in the colliding hadrons. Studies of the PDF were pursued at the Tevatron, and currently carried out at the LHC.

2.3 Quantum Chromodynamics

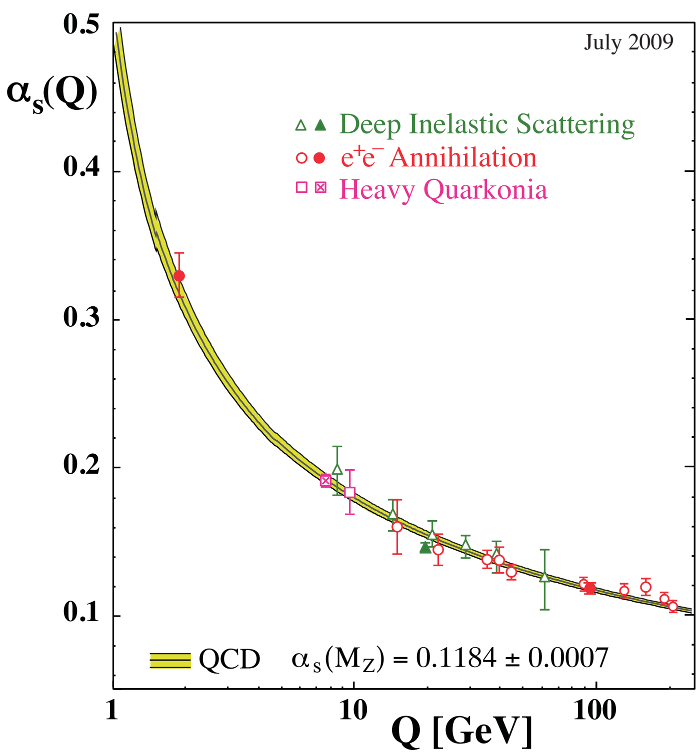

Figure 2.2: Measurements of the QCD coupling constant as a function of energy.

The theory of Quantum ChromoDynamics (QCD) was first formulated in the years 1972-73 by Murray Gell-Mann [7] and Steven Weinberg. It is described by an SU(3) gauge theory, more specifically a non-Abelian gauge theory. A unique feature of non-Abelian theories is the correlation between the strength of interaction and distance scales. In QCD these characteristics lead to confinement and asymptotic freedom. Confinement of color charges is due to the fact that the force between quarks increases as the distance between them gets larger. This suggests that it would take and infinite amount of energy to isolate a single quark. This keeps the quarks bound 'inside' hadrons. Now, in short ranges the color force decreases. This allows the quarks and gluons to behave as if they were essentially free, inside a hadron. In order to probe distances $\sim 1\ fm$ or less, a very-high momentum particle is required. At asymptotically high energies the quarks can be probed as if they were free. The prediction of such behavior in 1970 granted a Nobel Prize in to Politzer, Wilczek and Gross [8]. The strong interaction is regulated by a coupling constant, α_s. The α_s constant behaves as in Eq. 2.1 [9]. Where α_0 is the coupling constant for the momentum transfer μ and n_f is the number of flavors and q^2 is the momentum transfer in a 2-2 process. Figure 2.2 shows the behavior of α_s as a function of energy. It can be observed that the strength of the coupling decreases at higher energies, while it diverges in the low-energy end. Deep Inelastic Scattering (DIS) measurements of α_s, with e^+e^- and heavy quarkonia in a wide range of energies are shown. The value at the Z pole, $\alpha_s(m_Z)$ is found to be 0.1184 $\pm$0.0007 [10].

$$\alpha_s(q^2) = \frac{\alpha_0}{1 + \alpha_0 \frac{(33-2n_f)}{12\pi} \ln(\frac{-q^2}{\mu^2})} \tag{2.1}$$

The strong force is the responsible for internal degree of freedom in known as *color*. Gluons are the mediator bosons that act between quarks. In a quark-antiquark interaction, a particle with three possible types of color charges interacts with another one with three possible color charges. There can be in principle nine types of gluons belonging to a color singlet state in the U(1) group and a color octate state in a SU(3) group. The color singlet state would not carry a color charge and therefore will be colorless. A colorless and massless gluon would lead to a long range interaction between color singlet hadrons. Since this interaction is not observed in nature, the color singlet gluon state is forbidden. There are, thus, only eight gluons as members of the color octet, all of which carry color charges. In contrast with QED, where the mediator particle (photon) cannot interact with itself, in QCD gluons can interact with quarks as well as with other gluons. The observation of three-jet events in e^+e^- collisions [11] provided the first experimental observation of the gluon.

QCD describes the interactions of matter in the sub-atomic scale and describes the physics of the strong interaction. Quarks and gluons make up hadrons, which are color-singlet states. Deep Inelastic Scattering is the one direct way to obtain evidence of the existence of quarks. A high energy electron can probe deep inside the proton. The scattering pattern from the collisions suggests a point-like structure within the nucleus, thus suggesting an interaction with an elementary particle. The top quark, the last piece of the SM to be found, was discovered at Fermilab in 1995 by the CDF and D0 collaborations [12, 13].XXX needs transition perturbative approach

2.4 Physics of the QGP

QCD is the only sector of the SM whose full *collective* behavior is accessible to study in the laboratory. At low energies, partons (quarks and gluons) are confined inside hadrons. At high densities, in the non-perturbative region of QCD, a strongly interacting matter in thermal equilibrium at a finite temperature is created [14]. Heavy-Ion collisions are expected to produce hot and dense medium, consisting of de-confined quark and gluons, known as the Quark Gluon Plasma (QGP). The study of the of the many-body dynamics of high-density QCD covers a vast range of fundamental physics problems, described below [15]:

- De-confinement and chiral symmetry restoration: Lattice QCD calculations [15] predict a new form of matter at energy densities well above the critical density, $\epsilon_c \approx 1$ GeV/fm^3 consisting of an extended volume of de-confined and bare-mass quarks and gluons, the QGP [16]. The exploration of this phase of matter (equation of state, order of the phase transition, transport properties) promises to shed light on basic aspect of the strong interaction.

- Early universe cosmology: The quark-hadron phase transition took place some 10 μs after the Big-Bang, and is believed to be the most important event between the electr-weak transition and the Big-Bang nucleosynthesis. Several cosmological implications follow, such as formation of strangelets, cold dark matter or baryon fluctuations. For a review see Ref. [17] .

- Proton structure and evolution at small-x: At high energies, hadrons consist of a very dense system of gluons with small (Bjorken) momentum $x = p_{parton}/p_{hadron}$. At low x, the probability to emit an extra gluon is large, and gg fusion processes play an increasing role. At $x < 10^{-2}$ hadrons are more appropriately described in the context of the Color Glass Condensate (CGC) [18, 15]

- Gauge-string duality: Theoretical applications of the Anti-de Sitter/Conformal-Field-Theory (AdS/CFT) duality provide results in strongly coupled gauge theories[19, 15]. Applications of this formalism for QCD-like theories have led to the determination of transport properties, such as QGP viscosity [20], the 'jet quenching' parameter $\langle \hat{q} \rangle$ [21], or the heavy quark diffusion coefficient [22].

- Compact object astrophysics: At high baryon densities, the attractive force between quarks can lead to the formation of Cooper pairs. Cold dense matter is expected to behave as a color super-conductor [23]. This may be realized in the core of neutron stars, and be open to astronomical observation.

2.4.1 Experimental probes of hot QCD matter

The only experimental way to reproduce a hot and dense colored medium is via collisions of heavy-ions at ultra-relativistic energies. Information about the properties of the strongly interactive medium, created in Heavy-Ion collision, is commonly inferred from a comparison to baseline system. The baseline can be established with measurements in pp or pA collisions. The comparison of pA with pp collisions allows to identify cold nuclear matter effects; while the comparison of AA with pp collisions can shed light on hot QCD processes. The observation is presented in the form of ratios. The suppression or enhancement of yields and/or spectra are linked to properties of the medium. For the QGP to be formed in ultra-relativistic Heavy-Ion collisions, the initial temperatures and energy densities must be larger than the critical temperature ($T_c \approx 170$ MeV) [24] and the critical density ϵ_c. An estimation of the formation time of the plasma, τ_0, by Bjorken is found to be 1 fm/c [25]. Various estimates place the particle production time at about the same range τ_{pro} = 0.4-1.2 fm/c [9]. There are several ways in which the QGP can look different than a simple superposition of hadronic interactions and can reveal some of its high density or high temeperature properties.

2.4.2 Signatures of the Quark Gluon Plasma

After a QGP has been formed a subsequent cooling a phase allows the matter to return to a hadronic phase. Particles that arise from the interactions between constituents of the plasma will provide information about the state of the QGP. There is no single unequivocal way to identify the creation of a QGP state. It is the combination of data from measurements of different observables that may indicate the presence of a de-confined state.

Dilepton Formation

In the QGP, a quark can interact with an antiquark to form a virtual photon that will decay into a di-lepton. Leptons interact with the particles in the interaction region only via the electromagnetic force, but not via the strong force. Therefore, the production rate, and momentum distributions of the produced l^+l^- pairs carry information of the thermodynamical state of the medium at at the moment of their production [9]. The invariant mass spectra can render information about the temperature of the system. For these measurements the dynamical evolution of the system, radial flow and others sources of di-lepton background, must be properly taken into account. The dominant non-QGP production of di-leptons comes from Drell-Yan ($q\bar{q} \rightarrow \gamma \rightarrow l^-l^+$) processes. It is interesting to inquire about the di-lepton yield arising from the produced matter in the QGP. In the region below and invariant mass of 1 GeV/c^2, the decay from ρ, ω and ϕ dominate the production of l^+l^-pairs arising from a possible formation of the QGP[26]. The di-lectron mass spectra from the CERES collaboration at the CERN SPS [27], show an invariant mass spectra from Pb+Au collisions that does not match the ‘hadronic cocktail’ used to describe p+Be data. This is confirmed in the di-muon channel in In+In collisions in the same mass range by the NA60 collaboration[28], and more recently by the PHENIX collaboration [29] . A similar excess below the mass of the ρ is observed. Some modifications to the low mass vector boson are expected from the QGP formation, but a full quantitative understanding is still out of our grasp at the moment.

Quarkonium suppression

One of the most striking signatures of the presence of a state of de-confinement and at high temperature, is the suppression of the quarkonium states [30]. The force tying together the $Q\bar{Q}$ pair, is screened by the quarks and gluons around them. The suppression is is predicted to occur above a critical temperature, T_c, and subsequently in order of the binding energy of the quarkonium state. The Υ(1S) is the strongest bound quarkonium state, and is expected to melt last. Some models associate dissociation of states with temperatures ranges with respect to T_c. The melting of the Upsilon states is taken as an indicative of temperatures in the range of 1-3 T_c, Similarly, the melting of charmonium states indicate a temperature range of 1-1.2 T_c [31]. Other mechanisms that affect the measured yields may be at play. These include cold nuclear matter effects that can reduce the production without the presence of a QGP[32, 33] or recombination mechanisms that enhance the production via statistical recombination[34, 35, 36], mainly for the J/psi.

Jet Quenching

The study of jets in Heavy-Ion collisions is of great interest given that jets are believed to result from quark and gluons, thus, carrying information about the QGP. The definition of a jet is algorithm-dependent, but can be loosely defined as a an attempt to recover the kinematics of scattered partons. The general approach is to attempt to group together particles that are close in phase-space around a ‘leading particle’. Ideally, jets are a collection of hadrons, therefore sensitive the the strongly interacting field. It has been found that jets in the opposite side (in ϕ), to that of a leading hadron, show a different a pattern in AuAu collisions than in d+Au and p+p collisions [37] In the most central events the jet in the a away side disappears. The observed absorption of jets as a function of the geometry of the collision suggest the possibility of the use of *jet tomography* as a tool to investigate the densities within the plasma. This can be done with a 'control' probe in place, such as can be the the photon and Z^0 .

Flow

In the hydrodynamic expansion following the Heavy-Ion collision, the matter develops a correlated emission pattern known as *flow*. This is a collective phenomenon that was already observed at low energies. The flow pattern is related to the equation of state of the system through the dependence of the pressure on the temperature and energy density [38]. The experimental observations show a correlated emission of particles, that develops an anisotropic pattern in the distribution of particles in the azimuthal angle. Given the periodic nature of the correlation a Fourier expansion is used decompose the observation into modes. The second mode, v_2, is closely related to the amount of energy that flows out-of-plane with respect to the collision geometry. It is found that with initial conditions, which assume a superposition of nucleons according to measured nuclear-density profiles, suitably generalized to account for the longitudinal structure of the initial fireball[39], hadronic dissipation is sufficient to explain the data obtained at $\sqrt{s} = 200$ GeV[40].

2.5 Heavy Ion Collisions at LHC

The study of *PbPb* collisions at the LHC opens a previously inaccessible regime for Heavy-Ion physics. The factor of 14× increase in center-of-mass energy, compared to previous ion accelerations, opens a new set of probes to study the hot dense medium at unprecedented values of energy density. The capabilities of the CMS detector allow for very clean measurements even in the busy environment of Heavy-Ion collisions. The production rates for hard probes will allow to carry out a measurement of high-Q^2 processes. Hard probes include jets, high-p_T hadrons, heavy quarks, quarkonia and weak bosons. These are of crucial importance because they originate from initial hard scattering and are directly coupled to the fundamental QCD degrees of freedom. Their production timescale is short $\tau \approx 1/p_T \leq 0.1$ fm/c allowing them to propagate through and potentially be affected by the medium. Also, their cross-sections can be theoretically predicted using the perturbative QCD (pQCD) framework [41]. In light of this, hard probes can provide precise *tomographic* information about the hottest and densest phases of the reaction. Perturbative probes that do not couple to the colored partons, such as direct photons, di-leptons, Z^0 and $W^{\pm}$ bosons, are not affected by final state interactions. They can provide direct information about the parton distribution functions of the colliding ions. Furthermore, these weakly interacting probes can be used as undistorted references when produced in a recoil with jets. Fig 2.3 [42] shows the $PbPb$ cross-sections for hard processes as a function of the center-of-mass energy of the colliding system. The $PbPb$ cross-section, σ_{PbPb}, is obtained by scaling the cross-section of a given process at NLO in pp collisions, by a factor of A^2 to account for the scaling of the nuclear geometry. This is knows as 'binary collision scaling', and it assumes that each possible nucleon-nucleaon collisions can contribute equally to the production cross-section. Akin to the assumption that the yields in PbPb are given by an incoherent superposition of the total number of possible nucleon-nucleon collisions. It can be observed that processes like Υ, Z^0 , $W^{\pm}$ and hard jets are non-existent or marginal at best at RHIC energies.

2.5.1 High transverse momenta

Particles emitted at high transverse momenta (p_T) are believed to come from hard scattering processes, and the yield of high-p_T particles is expected to scale with the number of binary collisions, N_{coll}. Medium effects can certainly modify this scaling. The deviations from this scaling are quantified by the nuclear modification factor, R_{AA}. In the soft part of the spectra, $p_T \leq$ 2-3 GeV/c an enhancement is seen. This is due to the fact that in this regime particle yields scale with number of participants. Measurements comparing the nuclear modification factor for direct photons with π^0 and η show opposite effects: a suppression of the π^0 and η as a function of p_T, while the R_{AA} of the direct photons is found to be 1 at $p_T \geq 2$ GeV/c [43, 44]. The high-p_T photons play the role of "control" probe, in the sense that they go thorough the medium unmodified. Photons do not interact with the colored medium. Given the high multiplicity nature of Heavy-Ion collisions the measurement of direct photons poses a great challenge. The background for this type of

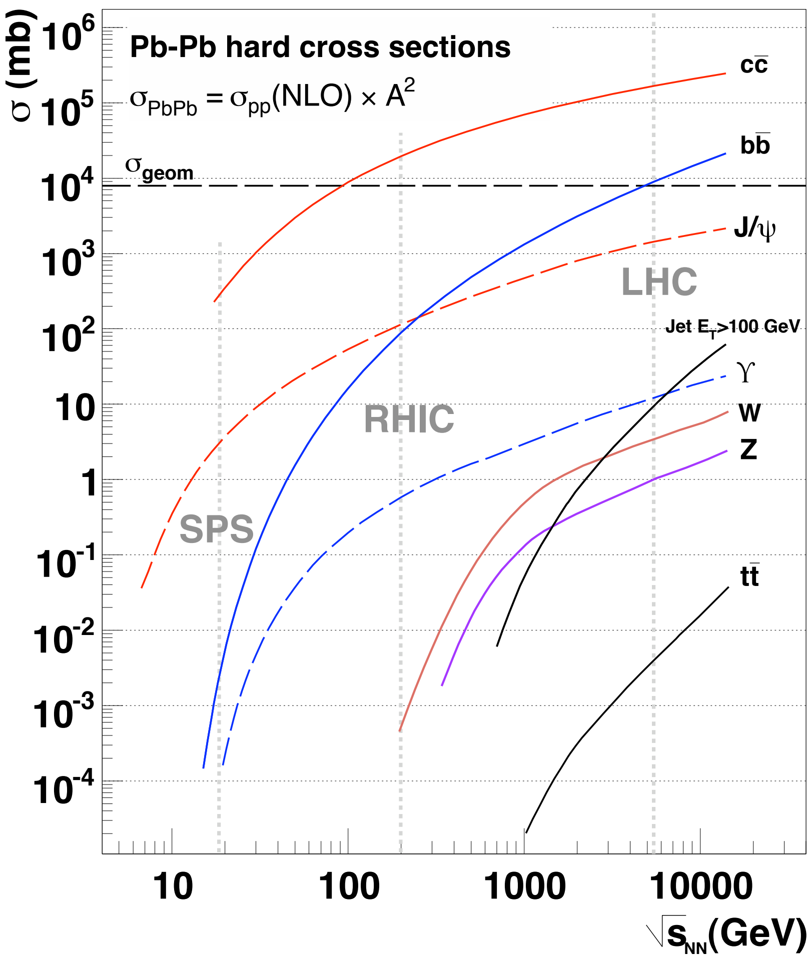

Figure 2.3: *PbPb* cross-section as a function of $\sqrt{s_{NN}}$ for high-Q^2 processes

measurement is copiously produced by: the decay of π^0's, and other mesons. It requires a careful identification and rejection of photons from other sources in order to extract a proper nuclear modification factor. A better approach would be to use an non-interactive probe that can be cleanly identified. This is the case of the Z^0 in the dimuon channel, which will be discussed in the next section.

2.6 Electroweak Probes in Heavy Ion Collisions

At the LHC, the center-of mass energy allows access to the electroweak probes (EWK). EWK processes are therefore available for the first time in Heavy-Ion collisions. The

Z^0 and $W^{\pm}$ are massive gauge bosons that can traverse the hot QCD medium unaffected. The $W^{\pm}$ and Z^0 decay quickly after the collision. The reconstruction of these particles can be carried out in their lepton and di-lepton channels respectively. The decay lepton also traverses the plasma unaffected by the strong interactions. The CMS detector is especially suited for analyses of high-p_T muon channels. Given that a pair of high-p_T muons can be efficiently and cleanly reconstructed, this steers us towards the use of the Z $\rightarrow \mu^+\mu^-$ channel as a benchmark for hot nuclear effects. In order to take the Z^0 boson as a benchmark probe, a few effects need to be taken into account. The energy loss suffered by the muons have been estimated in [45] to have 2% effect. This is due to multiple scattering of the muons with electrically charged particles in the hot medium. Cold nuclear matter effects can also affect the yields. At the LHC, the probed x region ~ 0.02 is sensitive to isospin effects that arise from the change of quark composition of colliding systems. Different quark compositions that make up Pb-ions, (protons and neutrons) compared to only protons, give way to the sampling of different PDFs. The isospin effects are estimated to be on the order of 3% [46]. The phenomenon that is expected to have the largest effect is shadowing. The modification of the PDFs as a function of x is known as shadowing [47]. This effect is expected to modify the expected cross-section by 10-20% [46]. It is important to first understand cold nuclear effects such as shadowing, to study other medium effect by comparing leptonic and hadronic decay channels [47]. The branching ratio to hadronic decays is $\approx 70\%$, while the total leptonic decay is estimated to be $\approx$10%.

A perhaps more powerful approach can be taken by studying a Z^0 -tagged jets. The production channels of these events are $q\bar{q} \rightarrow Z^0 g$ and $qg \rightarrow Z^0 q$ while the subsequent decay will be a di-lepton and a jet. Thus providing with an *in-situ* probe to quantify the energy losses suffered by the jets. However, Ref. [48] indicates that NLO effect for Z^0 -tagged jets can cause a 25% $p_T$smearing that will have an effect over the 'jet-balancing'.

By making use of a beautifully designed detector, optimized for detection of high-$p_T$muons (among other things) it is possible measure processes that can act as a 'baseline' to study Heavy-Ion collsions. The Z $\rightarrow \mu^+\mu^-$ decay can be used as a control to quantify hot nuclear effect, when compared to the $Z \rightarrow q + \bar{q}$ channel. Where the only difference (modulo the branching ratio) in the measured yields would come from the interaction of the quarks with the medium. The Z^0 can also be use as an '*in-situ*' probe to quantify effects that an 'opposite-side' jet might suffer. Both of these measurement rely on an assumption that must be confirmed first. It must be shown that the Z^0 indeed follows predictions, of non-interaction with the colored medium. The Z $\rightarrow \mu^+\mu^-$ channel must be established as an unmodified probe. The dimuon channel in CMS allows for a very clean extraction that aids the measurement. By corroborating the expectations that prescribe no interaction between the QGP and an electroweak probe reconstructed in the dimuon channel, it can be established that Z $\rightarrow \mu^+\mu^-$ as a 'standard candle' in Heavy-Ion collisions.

Chapter 3

LHC and CMS Detector

3.1 LHC

3.1.1 LHC layout

The Large Hadron Collider (LHC) is a particle accelerator complex part of the European Center for Nuclear Research (CERN). The accelerator has a 26 659 meter circumference that goes under the French-Swiss border, and is on average 100 meters underground. It crosses the the French-swiss border at four different points. The accelerator tunnel is the one once occupied by the Large Electron-Positron Collider (LEP). It is a 3.8 m. in diameter concrete lined tunnel. The LHC is a synchrotron designed to collide two opposing beams. The accelerator complex is made up of 9300 magnets. The two counter-rotating beams cross at four different points, with a detector built around each of point. The experiments, shown in Fig 3.1, built around the interaction points are: A Toroidal Large LHC ApparatuS (ATLAS, at point-1), A Large Ion Collider Experiment (ALICE, at point-2), the Compact Muon Solenoid (CMS, at point-5) and the LHC Beauty experiment (LHCb, at point-8).

LHC parameters

The nominal center-of-mass energy for the LHC in proton-proton collisions is $\sqrt{s_{NN}} = 14$ TeV. For other nuclear species, the center of mass energy scales with Z/A, where Z and A are the proton and mass numbers, respectively. In the case of $PbPb$ col-

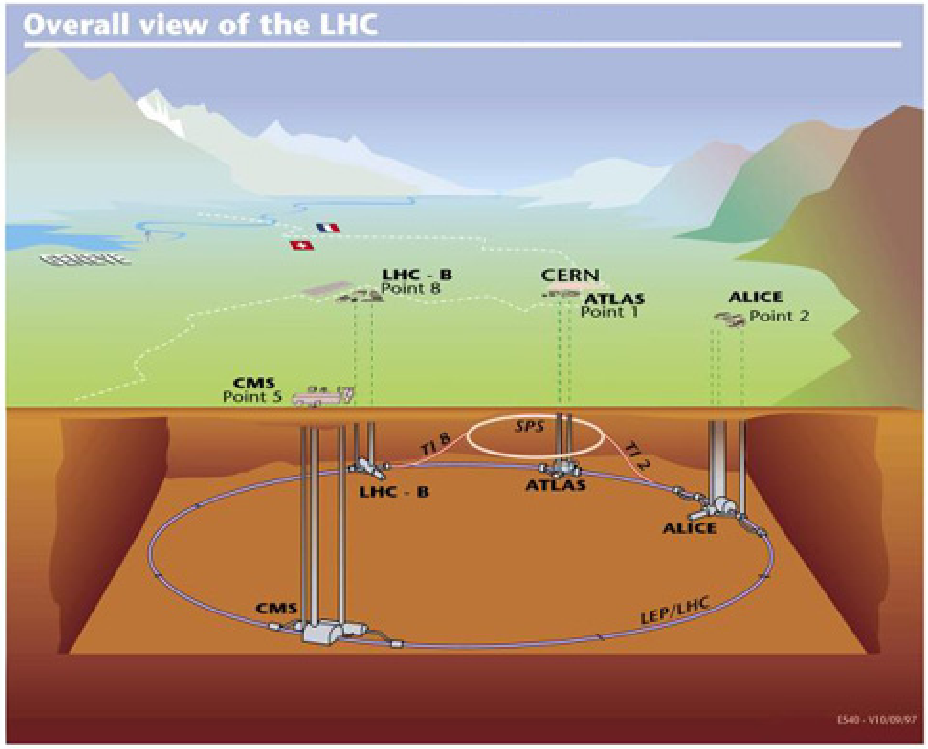

Figure 3.1: LHC layout.

lisions, we use ${}^{208}_{82}Pb$ nuclei, which can therefore be collided at $sqrts_{NN} = 5.5$ TeV. The event rate generated in the LHC is given by Eq. 3.1:

$$dN/dt = L\sigma_{event} \tag{3.1}$$

where σ_{event} is the cross section for the event under the study and the L the machine luminosity. The machine luminosity depends only on the beam parameters and can be written for a Gaussian beam distribution.

$$L = \frac{N_b^2 n_b f_{rev} \gamma_r}{4\pi \epsilon_n \beta^*} F \tag{3.2}$$

where the N_b is the number of particles per bunch, n_b the number of bunches per beam, f_{rev} is the revolution frequency, γ_r the relativistic gamma factor, ϵ_n the normalized transverse beam emittance, β^*, the beta-star function at the collision point, and F the geometric luminosity reduction factor due to the crossing angle at the interaction point (IP):

$$F = \left(1 + \left(\frac{\theta_c \sigma_z}{2\sigma*}\right)^2\right)^{-1/2} \quad (3.3)$$

Where θ_c is the full crossing angle at the IP, σ_z the RMS bunch length, and σ^* the transverse RMS beam size at the IP. The above expression assumes beams with circular profile in the direction plane transverse to the mean direction, with $\sigma_z \ll \beta$, and with equal beam parameters for both beams.

The LHC was designed as a proton-proton collider, as opposed to a proton-anitproton one. From this derives the requirement that the two counter-rotating beams make use of opposite magnetic dipole fields in each ring. The two beams share an approximately 130 m long common beam pipe along the IRs. There is not enough room for two separate rings of magnets in the LHC tunnel, for this reason the LHC uses twin bore magnets that consist of two sets of coils and beam channels within the same mechanical structure and cryostat.

The maximum particle density per bunch is limited by the non-linear beam-beam interaction that each particle experiences when the bunches of both beams collide with each other. The beam-beam interaction is measure by the linear tune shift, and is given by Eq. 3.4:

$$\xi = \frac{N_b r_p}{4\pi\epsilon_n} \quad (3.4)$$

in which r_p is the classical proton radius $r_p = e^2/(4\pi\epsilon_0 m_p c^2)$. Experience with existing hadron collider indicates that the total linear tune shift summed over all IPs should not exceed 0.015 [?]. With three proton experiments requiring head-on collisions, this implies that the linear beam-beam tune shift for each IP should satisfy $\xi < 0.005$ [49].

The luminosity lifetime in the LHC is not constant over a physics run, it decays due to degradation of intensities and emittances of the circular beams, the main cause of beam loss is from collision. The initial decay time of bunch intensity due to this effect is defined in:

$$\tau_{nuclear} = \frac{N_{tot,0}}{L\sigma_{tot}k} \quad (3.5)$$

where $N_{tot,0}$ is the initial beam intensity, L the initial luminosity, σ_{tot} the total cross-section and k the number of IPs. Assuming an initial peak luminosity of L = $10^{-34} cm^{-2} s{-}1$ and two high luminosity experiments, the above expression yields an initial decay time of τ = 44.85 h. Equation 3.5 results in the following decay of the beam intensity and luminosity functions of time:

$$N_{tot}(t) = \frac{N_{tot,0}}{1 + t/\tau_{nuclear}} \tag{3.6}$$

$$L(t) = \frac{L_0}{(1 + t/\tau_{nuclear})^2} \tag{3.7}$$

the time required to reach $1/e$ of the initial luminosity is given by:

$$t_{1/e} = (\sqrt{e} - 1)\tau \tag{3.8}$$

yielding a luminosity decay time of $\tau_{nuclear,1/e}$ = 29h. Other contributions come from Toucheck scattering and from particle losses due to a slow emittance blow-up.

The integrated luminosity over one run yields

$$L_{int} = L_0 \tau_L \left[1 - e^{-T_{run}/\tau_L}\right] \tag{3.9}$$

where T_{run} (14.9 h) is the total length of the luminosity run.

3.1.2 LHC design

The LHC complex itself is made up of other subsystems that work to ionize, store, transfer and ramp up the energy of the beams. The LHC is therefore designed as a proton-proton collider with separate magnet elds and vacuum chambers in the main arcs and with common sections only at the insertion regions where the experimental detectors are located. The LHC is supplied with protons from the injector chain Linac2 - Proton Synchrotron Booster (PSB) - Super Proton Synchrotron(SPS) as shown in Fig. 3.2. The main challenges for the PS complex are (i) the unprecedented transverse beam brightness (intensity/emittance), almost twice that which the PS produced in the past and (ii) the production of a bunch train with the LHC spacing of $25 ns$ before extraction from the PS. The Linac2 generates 50 MeV protons, which are fed to the PSB. These protons get accelerated to 1.4 GeV and sent into the PS where they get ramped up to 26 GeV. After that, the SPS takes them to an energy of 450 GeV to later be injected in the LHC. In the main ring the bunches are accumulated, and accelerated to reach the peak energy for collisions.

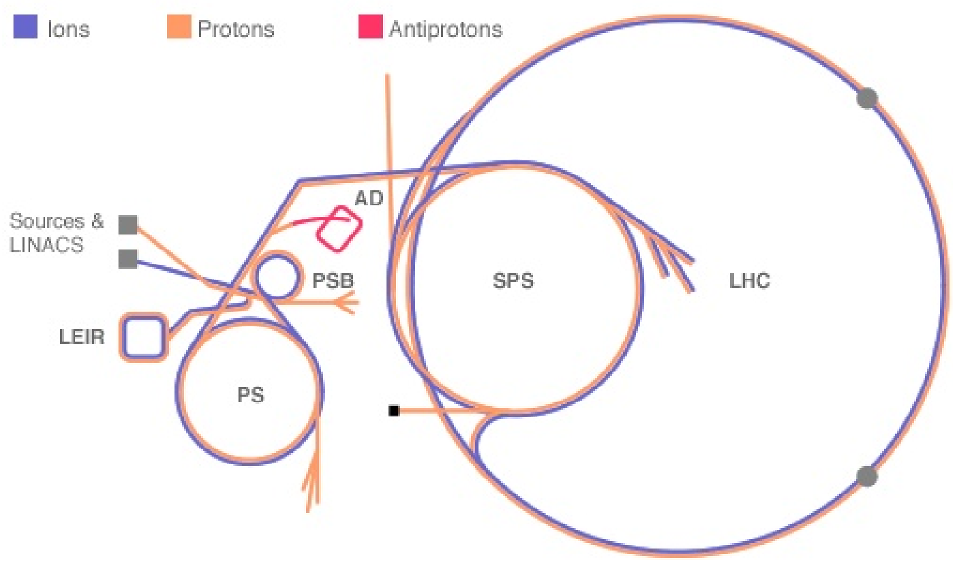

Figure 3.2: LHC injection complex.

3.1.3 LHC as an ion collider

Heavy-Ion collisions were included in the conceptual design of the LHC from an early stage. The nominal magnetic field of 8.33 T in the dipole magnets will allow for a beam energy of 2.76 TeV/nucleon yielding a total center-of-mass energy of 1.15 PeV and design luminosity of $1.0{\times}10^{27}cm^{-1}s^{-1}$. Currently, the magnets are operating at half the designed field. Achieving a, have a total center-of-mass energy of 2.76 TeV/nucleaon. While major hardware systems of the LHC ring appear compatible with Heavy-Ion operation the beam dynamics and performance limits are quite different than for *pp* collisions. Some of the aspects of Heavy-Ion beams are similar to those in proton beams, such as the emittance which has been chosen so that the ion beams have the same geometric size as the *pp* ones.

The lead ions are produced from a highly purified lead sample heated to a temperature of about 550° C. Many different charge states are produced with a maximum around

Pb^{+27}. These ions are selected and accelerated to 4.2 MeV per nucleon by the Linear Accelerator (Linac3) before passing thorough a carbon foil, which strips most of them to Pb^{+54}. The Pb^{+54} beam is accumulated, then accelerated to 72 MeV per nucleon into the Low Energy Ion Ring (LEIR). Subsequently, the ions get transfered to the PS and reach the energy of 5.9 GeV per nucleon. Then, later get sent to the SPS after first passing them through a second foil where they get fully stripped to Pb^{+82}. The SPS accelerates them to 177 GeV per nucleon and sends the beam to the LHC to reach an energy of 2.76 TeV per nucleon.

Nuclear interaction on ion beams at the LHC

When ultra-relativistic lead ions collide at LHC energies, numerous processes of nuclear fragmentation and particle production can occur. Some of these have direct consequences as performance limits for the collider. Besides the hadronic nuclear interactions due to direct nuclear overlap Ultra Peripheral Collisions (UPC) of the form

$$^{208}_{82}Pb +^{208}_{82} Pb \overset{nuclear}{\longrightarrow} X \tag{3.10}$$

yield a cross-section of $\sigma_H \approx 8$ barn which gives way to the longer range electromagnetic interactions. For the total cross-section, all the contributions will affect the the total loss rate and the resulting beam lifetime. However, certain processes cause concentrated particle losses. These can produce heating in localized section of the LHC which can in turn result in a magnet quench. One of the processes is electron capture from pair production (EECP). Another effect can be electromagnetic dissociation (EMD), in which the lead ion makes a transition to an excited state and then decays with the emission of a neutron, leaving a lighter isotope. The total cross-section for removal of an ion from the beam is

$$\sigma_{\text{Total}} = \sigma_{\text{hadronic}} + \sigma_{\text{EECP}} + \sigma_{\text{EMD}} \tag{3.11}$$

Synchrotron radiation

The LHC is not only the first proton storage ring in which synchrotron radiation plays a noticeable role, but also the first Heavy-Ion ring in which synchrotron radiation has a significant effect on beam dynamics. Surprisingly, some of these effects are stronger for lead ions than for protons because charges in the ions behave coherently. Quantities such as the energy loss per turn from synchrotron radiation, and the radiation damping time for ions, are obtained from the familiar formulae for electrons by replacing the classical electron radius and the mass by those of the ions. It is noticed that radiation damping for heavy ions such as lead is about twice as fast as for protons, and that the emittance-damping times are comparable with the growth times from intra-beam scattering [50].

3.2 CMS detector

3.2.1 Overview

The Compact Muon Solenoid (CMS) is one of the four experiments that are part of the LHC. It is located in the LHC main ring at point-5, 100 meters underground, in Cessy, France. CMS, as well as ATLAS, is one of the two multipurpose experiments at the LHC. The CMS program can span many areas of High-Energy and Heavy-Ion physics, but it is especially suited for the high-$p_T$regime. As a discovery machine, one of the main areas of interest comprises the search for Higgs Boson(s) in the Standard Model and its extensions, such as the search for SUperSYmmetry (SUSY) evidence, and extra dimensions. At the center of the Heavy-Ion program is the study of strongly interacting matter produced in $PbPb$ collisions at the highest energy densities ever reached in the laboratory. To achieve this, CMS makes use of various types of technologies that compliment each other and ensure a robust measurements. Very good tracking resolution, a wide calorimetric coverage, great muon identification, a fast triggering system and a 4 Tesla magnetic field are some of the key components that make up a state-of-the art-detector. The main requirements for CMS to meet the physics goals are:

- Good muon identification and momentum resolution over a wide range of momenta and angles, good dimuon mass resolution($\approx$ 1% at 100 GeV), and the ability to determine unambiguously the charge of muons with p_T< 1 TeV/c.

- Good charged particle momentum resolution and reconstruction efficiency in the inner tracker. Efficient triggering and offline tagging of τ's and b-jets requiring a pixel detector close to the interaction point.

- Good electromagnetic energy resolution, good diphoton and dielectron mass resolution ($\approx$ 1% at 100 GeV), wide geometric coverage, π^0 identification and eventually rejection, and efficient photon and lepton isolation at high luminosity.

- Good missing-transverse-energy and jet-energy resolution, requiring hadronic calorimeters with large (nearly hermetic) geometric coverage and with fine lateral segmentation.

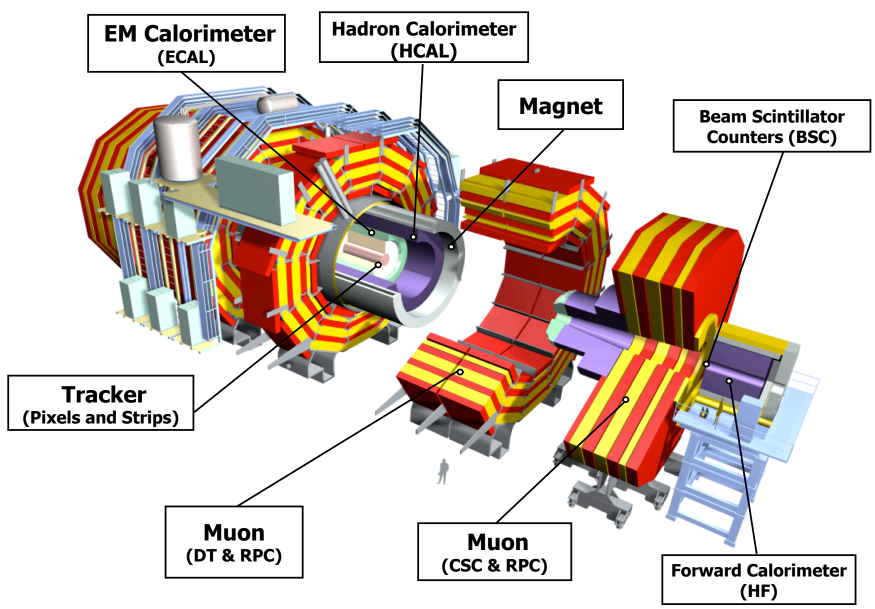

Figure 3.3: CMS detectors

A reference set of coordinates was adopted by the CMS collaboration in which the origin is at the center of the detector where collisions are expected to occur. The z-axis point along the beam axis towards the Jura mountains, the y-axis points vertically straight up, and the positive x-axis points inward towards the center of the LHC. A more "detector friendly" set of coordinates is the cylindrical set, in which the z-coordinate is the same as the z-axis, the ϕ-coordinate is azimuthal around the z-axis, the radial coordinate increases around the z-axis. In collider physics it is more useful to define the variable η, known as pseudorapidity and defined in Eq 3.12. It a variable defined with respect to the center of the detector, where the collisions occur.

$$\eta = -\ln\left[\tan(\theta/2)\right] \tag{3.12}$$

The CMS detector is roughly 22 m in length,15 m in diameter and 12 500 metric tons in weight. A complete description of the construction and performance can be found in [51]. The central feature is a 4 Tesla solenoid, 13 meters in length and 6 meters in diameter. A silicon tracker, utilizing both pixel and micro-strip technologies, is the inner-most detector sub-system in the central rapidity region. An electromagnetic calorimeter (ECAL) with a coverage of $|\eta| < 3$ and a hadronic calorimeter (HCAL) $|\eta| < 5$ are located within the magnet solenoid. The outermost subsystems are muon detectors with a coverage of $|\eta| < 2.4$, embedded in the return yoke, three different technologies are used for muon detection. The Cathode Strip Chambers (CSC) and Resistive Plate Chambers (RPC) cover the endcaps, while the RPCs and Drift Tubes (DT) span the barrel region. Three other detectors are located in the forward region. The CASTOR detector in $5.3 < |\eta| < 6.6$, and a a zero-degree calorimeter (ZDC) covers $|\eta| > 8.3$. To complement CMS, the TOTEM experiment will measure the total pp cross-section with the luminosity independent method and study elastic and diffractive scattering at the LHC.

3.2.2 Inner tracker

The inner tracker is comprised of two technologies. Radially, the inner-most is a silicon pixel tracker (PIX), followed by the silicon strips tracker (ST). The PIX is the closest detector to the interaction region, and therefore subject to the largest particle flux. The size of a pixel is $\approx 100 \times 150\ \mu m^2$ giving an occupancy of about 10^{-4} per pixel per

LHC crossing in the *pp* collision scenario. In the intermediate region (20 < r < 55 *cm*) the particle flux is low enough to make use of larger pitch microstrips with an occupancy ≈ 2-5% per LHC crossing. While in the outermost region (r≤ 55 *cm*) the occupancy of ≈1% allows for the use of larger silicon strip of size 25 *cm* × 180 μm. In *PbPb* collisions the occupancy is expected to be kept at ≈ 1% in the pixels, while in the silicon strip is expected to be at around 20%.

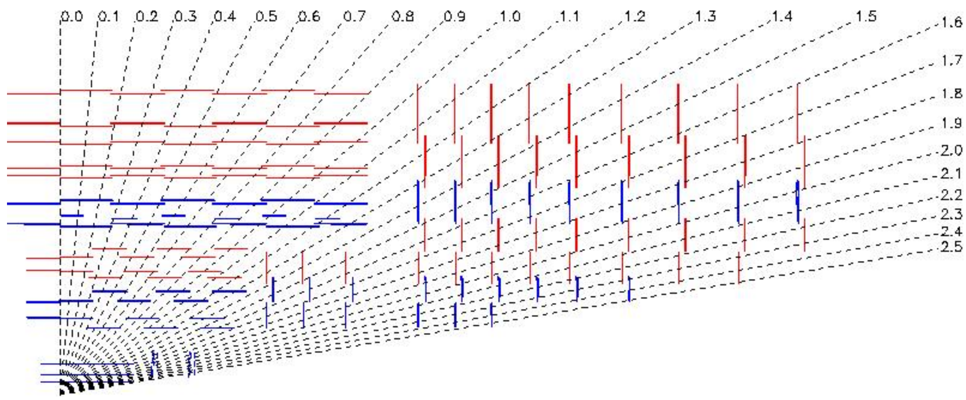

Figure 3.4: Quarter view of inner tracker. The coverage extends up to 2.5 units in η. The inner-most layers are the silicon pixels. The outer layers are the silicon strips.

The PIX detector is made up of three layers at radii of 4, 7 and 11 cm in the barrel region, and in the endcap there are two layers of pixels. The silicon strip detectors are placed at r between 20 and 110 cm, while in the forward region there are 9 microstrip layers. Fig 3.4 shows a quarter view of the inner tracker layers. The total area of the pixel detector is ≈1 m^2 while the silicon strips span an area of ∼ 200 m^2 with a coverage up to $|\eta|$ <2.4.The inner tracker comprises 66 million pixels and 9.6 million silicon strips[52].f In order to achieve optimal vertex position resolution, an almost square pixel shape of 100 × 150 μm^2 in both the (r, ϕ) and the z-coordinate were adopted. The barrel region od the tracker comprises 768 pixel modules arranged into half-ladders of 4 identical modules each. The large Lorentz effect (Lorentz angle 23°) improves the r-ϕ resolution through charge sharing. The endcap disks are assembled in a turbine-like geometry with blades rotated by 20° to also benefit from the Lorentz effect.

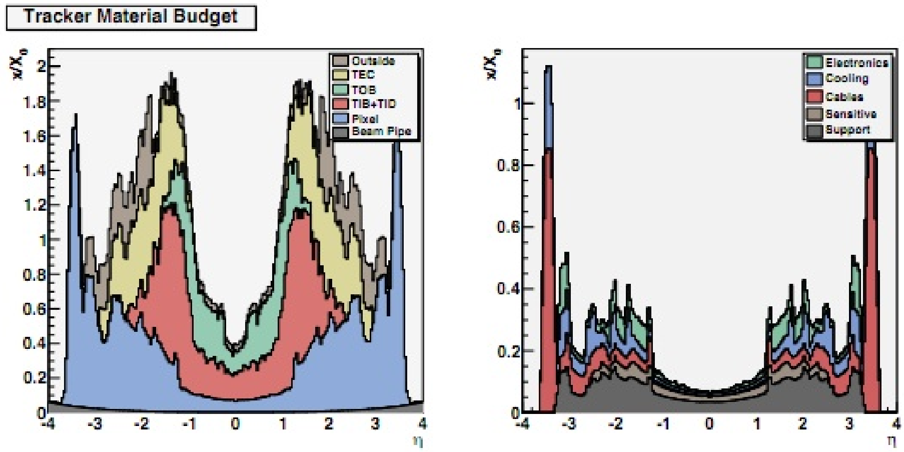

Figure 3.5: Material budget of tracker system and pixel detector

3.2.3 ECAL

The ECAL is a hermetic, homogeneous calorimeter comprising 61200 lead tungstate ($PbWO_4$) crystals mounted in the central barrel, complemented by 7324 crystal in each of the endcaps. The crystals have a short radiation lengths, $\chi_0 = 0.89$ cm, and have a $Moli\grave{e}re$ radius of 2.2 cm. The crystals are fast, 80% of the light is emitted within 25 ns, and are radiation hard, up to 10 Mrad. Avalanche photodiodes (APDs) are used as photodetectors in the barrel and vacuum photo-triodes (VPTs) in the endcaps.

The barrel section has an inner radius of 129 cm. It is structured as 35 identical “supermodules”, each covering half the barrel length and corresponding to a pseudorapidity interval of $0 < |\eta| < 1.479$. The crystals have a front face cross-section of $\approx 22 \times 22$ mm^2 and a length of 230 mm, corresponding to 25.8 χ_0.

The endcaps, at a distance of $314cm$ from the vertex and covering a pseudorapidity range of $1.479 < |\eta| < 3.0$, are structured as 2 back-to-back semi-circular aluminum plates formed of structural units of 5×5 crystals, know as “supercrystals”. The endcap crystals are arranged in an $x - y$ grid (not an $\eta - \phi$ grid). They are all identical and have a front face cross-section of 28.6×28.6 mm^{2}and a length of a 220 mm (24.7 χ_0)[51].

3.2.4 HCAL

The design of the hadron calorimeter was driven by the choice of magnet parameters since most of the CMS calorimetry is located inside the magnet coil and surrounds the ECAL system. An important requirement of the HCAL is to minimize the non-Gaussian tails in the energy resolution and to provide good containment and hermeticity to the missing transverse energy. Due to this the HCAL design maximizes material inside the magnet coil in terms of interaction lengths and is complemented by an extra layer of scintillators referred as the Hadron Outer (HO) detector, placed outside the coil. The absorber material layers are made out of brass, which is non-magnetics and has a short interaction length.

The barrel part of the HCAL covers -1.4 $< \eta <$ 1.4, which translate to 2304 towers with a segmentation $\Delta\eta \times \Delta\phi = 0.087 \times 0.087$. There are 15 brass plates in total, each with a thickness of about 5 cm, plus 2 external stainless steel plates for mechanical strength. Particles leaving the ECAL volume see first a scintillator plate with thickness of 9 mm instead of the 3.7 mm for the other plates. The light collected by the first layer is optimized to be about 1.5$\times$ higher that the other scintillator plates.

The Hadron Outer covers the region -1.26 $< \eta <$ 1.26 which lies outside the coil. It samples the energy from penetrating hadron showers leaking through the rear of the calorimeters and which make it pass the magnet, increasing the effective thickness of the hadron calorimeter to over 10 interaction lengths (λ). All this reduces the energy resolution function and improves the missing transverse energy resolution of the calorimeter. The Hadron endcaps consist of 14 η towers with 5°ϕ segmentation, covering the pseudorapidity region 1.3$<|\eta|<$3.0, making a total of 2304 towers.

The Hadron Forward (HF) calorimeter covers the pseudorapidity between 3.0 and 5.0. It is made out of steel/quartz fiber. The front face of the HF is located 11.2 m from the interaction point, with a depth of 1.65 m. Because the neutral component of the hadron shower is preferentially sampled in the HF technology, this design leads to narrower and shorter hadronic showers and hence is ideally suited for the congested environment in the forward region.

3.2.5 Muon Systems

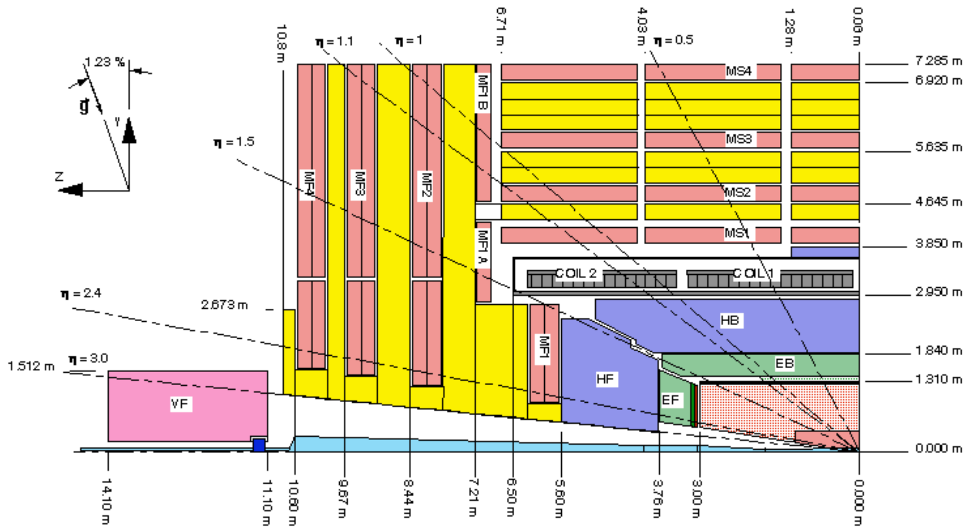

Figure 3.6: General layout of the different detectors that make up CMS. In light red, the muon chambers DT and CSC.

Muons are a very valuable handle in CMS. They are can be cleanly and unambiguously reconstructed, unlike jets or photons, and can be easily identified over the background, unlike electrons. The CMS muon system has three requirements, muon identification, muon trigger and muon measurement. Comprehensive simulation studies have indicated that the physics goals can be achieved if the muon detector has the following functionality and performance[53].

- Muon identification: at least 16λ of material is present up to η =2.4 with no acceptance losses.

- Muon trigger: the combination of muon chambers with precise resolution and a fast dedicated trigger detectors provide unambiguous beam crossing identification and trigger on single and multimuon events with well defined p_T thresholds from a few GeV to 100 GeV up to η =2.1.

- Standalone momentum reconstruction from 8 to 15% $\sigma(\delta_{p_T})/p_T$ at 10 GeV and 20 to 40 % at 1 TeV.

- Global momentum resolution: after matching with the Inner Tracker, the resolution is from 1.0 to 1.5 at 10 GeV, and from 6 to 17% at 1 TeV. Momentum-dependent spatial position matching at 1 TeV less than mm in the bending plane less than 10 mm in the non-bending plane.
- Charge Assignment: correct 99% confidence up to the kinematic limit of 7 TeV.
- Capability of withstanding the high radiation and the interaction background expected at the LHC.

The muon chambers are the outermost subsystems in the main body of the CMS detector. Direct muons that make it to the chambers have already been measured in the tracker, and have made it through the magnet coil, which removes a sizable portion of punch-through hadrons. Back-splash from the face of the HF, and the quadrupole magnet can be faked as muon especially in the outermost endcap chambers closest to the beam[53]. There are many factors that can limit the ability to of the muons system to measure accurately the momentum of a traversing muon :

- Multiple scattering in the calorimeters and in the thick steel plates separating the muons stations;
- Intrinsic resolution limitations of the detectors;
- Energy loss;
- Extra detector hits generated by muon radiation, δ-rays, and other backgrounds;
- Chamber misalignment;
- Uncertainty in the B field;

The muon momentum resolution is defined in Eq 3.13

$$\frac{\delta p_T}{p_T} = \frac{1/p_T^{meas} - 1/p_T^{gen}}{1/p_T^{gen}} \tag{3.13}$$

Figure 3.7 shows the p_T resolution for 2 pseudorapidity regions: the barrel (left) and endcaps (right). It can be seen that the p_T resolution of the "Full System" muon is obtained from the measurement in the tracker at low p_T, while at high-p_T the resolution is guided by the measurement in the muon chambers. It is also visible that the resolution worsens in the forward region. This is due to the "weaker" bending experienced by forward tracks that exit the solenoid traversing a smaller radial distance.

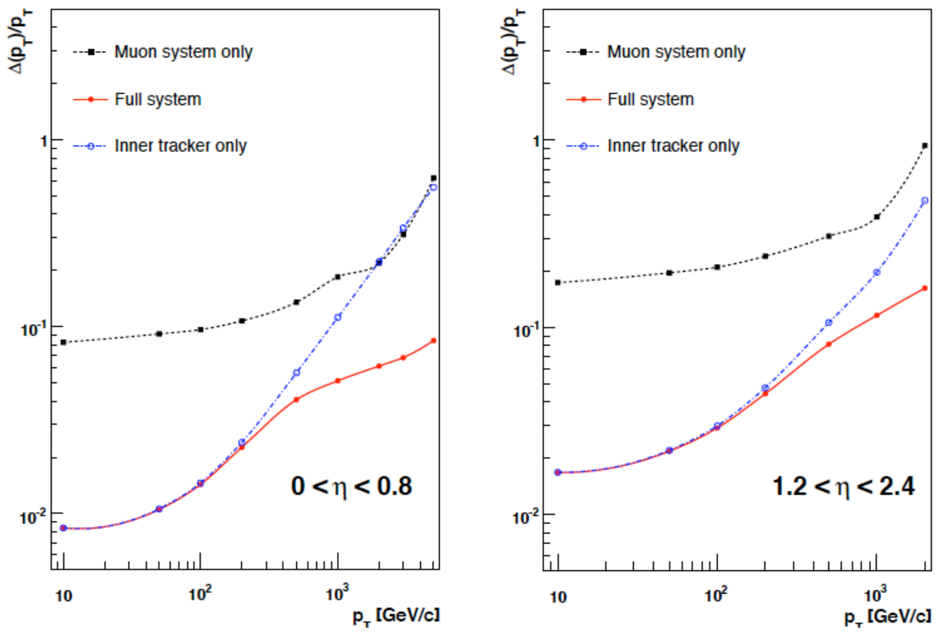

Figure 3.7: Muon $p_T$resolution in barrel region (left) an forward region (right)

CMS uses three gaseous detectors for muon identification: Drift Tubes (DT), Cathode Strip Chambers (CSC) and Resistive Plate Chambers (RPC).

3.2.6 Drift Tubes

The Drift Tubes are located in the barrel region and have a coverage of $|\eta| <1.2$. They are organized in 5 stations along the z-axis. Each station is made up of 4 concentric rings along the radial direction, as shown in Fig 3.9. This choice of detector for the barrel part is due to the low expected rate and the relatively low intensity of the local magnetic field. The principal wire length, around 2.5 m, is constrained by the longitudinal segmentation of the iron barrel yoke. The transverse dimension of the drift cell was chosen to be 2 cm or 350-400 μs. The tracking and timing performance of a chamber was optimized with a design using twelve layers of DTs divided into three groups of four consecutive layers,

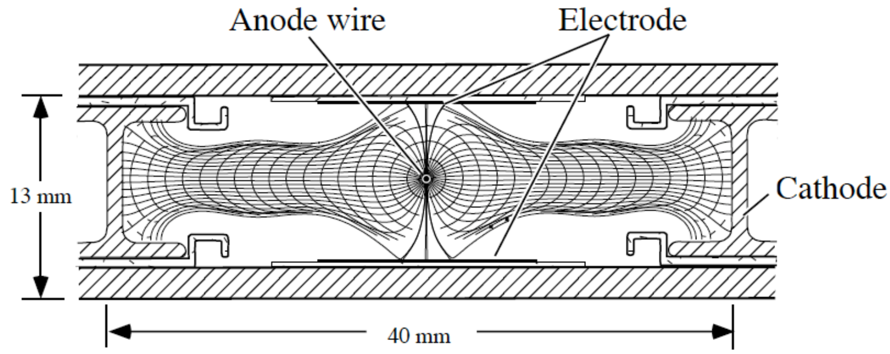

Figure 3.8: Drift Tube cell

named Super Layers(SL). Two SL's measure the (R,Φ) coordinate., i.e have wires parallel to the beam line, and the third measures the z-coordinate. The mechanical precision of the construction of the chamber is dictated by the aim to achieve the global resolution in (R,Φ) of 100 μm. This is achieved by the 8 track points measured in the two (R,Φ) SL, if the angle wire resolution is better than 250 μm. The cells operate at atmospheric pressure with an Ar/CO_2 gas mixture and keeping the CO_2 concentration in the range from 10- 20 %.

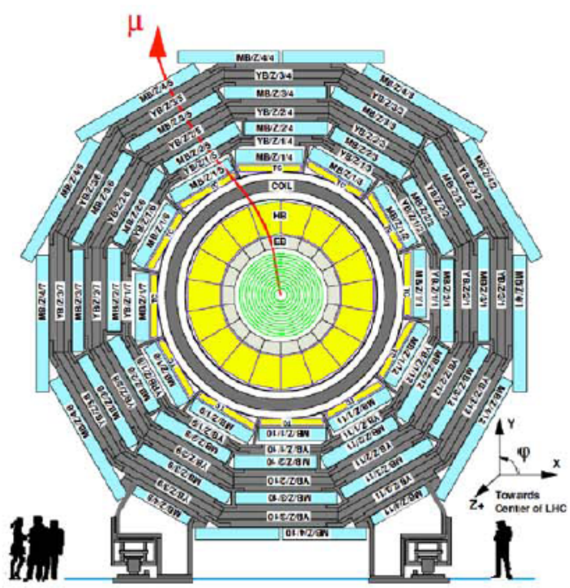

Figure 3.9: Layout of muon detector in the barrel region. In blue the DT and gray the return yoke. A muon track exemplified in red

The baseline cell design is shown in Fig 3.8, it has a pitch if 40 mm by 13 mm. At the center is the anode wire, made out of 50 μm diameter stainless steel. The cathodes defining the cell width are aluminum I-beams which are 1.2 mm thick and 9.6 mm high. A plastic profile is glued to the upper and lower side of the I-beams to isolate from the cathode. The wall plates are kept at ground potential, and a drift field is formed by putting the wires at positive voltage and the cathode wire at negative. A pair of positively-chaged strips has the effect of squeezing the drift lines, improving the linearity of the space-time relationship and resolution of the cell.

3.2.7 Cathode Strip Chambers

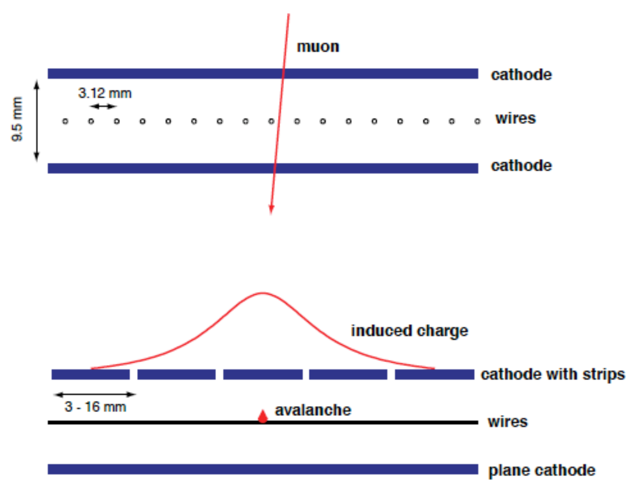

Figure 3.10: Coordinate measure of the CSCs. It shows the trajectory of a muon (top) and the induced charge left (bottom) that will be read

The Cathode Strip Chambers are part of the muon endcaps and have a coverage of $|\eta|$ >0.8. The CSCs are arranged in four discs on each side of the CMS barrel, with full ϕ coverage. Each disk is made out concentric rings, and each ring is made out of 18 or 26 stations. The cracks between the chamber rings are not projective, and thus coverage, defined as at least 3 chambers on a muon path, is close to 100%. The arrangement can be seen in Fig. 3.11. The CSCs are multi-wire proportional chambers in which one cathode plane is segmented into strips running across wires. An avalanche developed on a wire induces on the cathode plane a disturbed charge of a well known shape, see Fig 3.10. Charpak et al [54] showed that by interpolating the fractions of charge picked up by these strips, one can reconstruct the track position along the wire with a precision of 50 μm or better. A typical CSC is a six plane chamber of trapezoidal shape with maximum length of 3.4 m and a maximum width of 1.5 m. The major advantages of the CSCs are:

- intrinsic spatial resolution;
- closely spaced wires make the CSC a fast detector;
- by measuring signals from strips and wires one easily obtains two coordinates from a single detector plane;
- strips are fan-shaped to measure ϕ coordinate naturally;
- CSCs can operate in a large non-uniform magnetic field without significant deterioration to the performance;

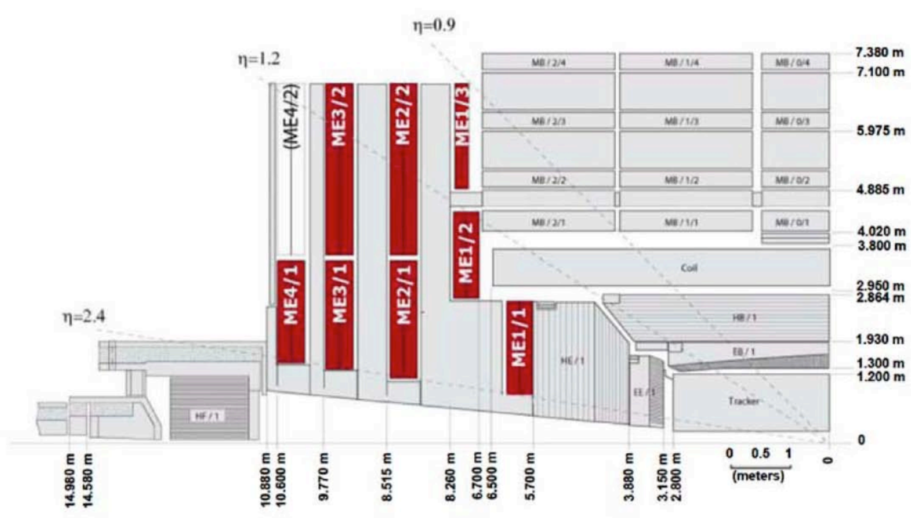

Figure 3.11: Location of CSCs (in red) within the muon system

A standard nomenclature refers to the subsystems as MEi/j where i labels the station and j the ring. Thus for example the innermost ring of the rst station, that closest to the Interaction Point (IP), is called ME1/1. All the CSCs lay outside the magnet except for the innermost ring of the first disk, the ME 1/1 chambers. Given their positions they operate in an axial magnetic field, to compensate for these the chambers are tilted by 25° with respect to a perpendicular to the chamber centerline. Since these chambers are the closest one to the collision point, they experience a high interaction rate. The main source of background hits comes from random hits from neutrons/ gammas (after knocking electron from surrounding materials), punch-through, pion and kaon decay-in-flight, tunnel muons and debris from muons going through calorimeters, iron disks, etc.

3.2.8 Resistive Plate Chambers

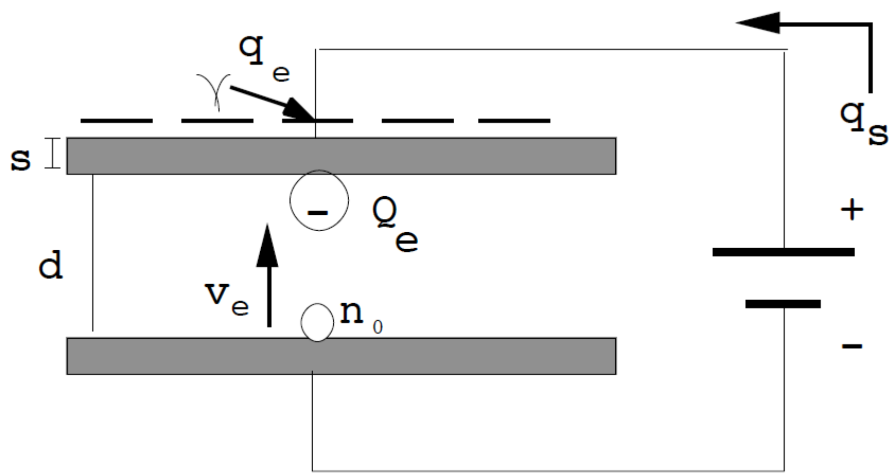

Figure 3.12: Schematic of parallel plates that make up the RPCs.

The RPC are gaseous parallel-plate detectors that combine adequate spatial resolution with time resolution comparable to that of scintillators[55]. An RPC is capable of tagging the time of an ionizing event with a time resolution in a much shorter time than the 25 ns between two consecutive LHC bunch-crossings. Therefore, a fast muon dedicated trigger can unambiguously identify the relevant bunch crossing at the design rate expected from the LHC. The RPC system offers a redundancy in the muon coverage, extending in a region $|\eta|$ <2.1 with full ϕ-coverage. An RPC based trigger has to perform three basic functions simultaneously:

- it has to identify a candidate muon
- it has to assign a bunch crossing to candidate track(s)
- it has to estimate transverse momenta

An RPC consist of two parallel plates separated by a gas gap of a few millimeters. The outer surfaces of the resistive material are coated with conductive graphite paint to form the HV and ground electrodes. The electrode resistivity mainly determines the rate capability, while the gap capability determines the time performance. Figure 3.12 shows a diagram of operation of the RPCs. A cluster of n_o electrons, produced by an ionizing particle ignites the avalanche multiplication. An electronic charge Q_e is then developed inside the gap of height d. The drift of such charge towards the anode induces on the puck-up electrode the fast charge q_e, which represents the useful signal of the RPC.

3.2.9 Forward Detectors

The Beam Scintillator Counters (BSC) are a set of large area scintillators mounted in front of HF to provide raw timing and beam halo information. The BSC are composed of 32(BSC1) + 4 (BSC2) polyvinyl-toluene plastic scintillator tiles. The location of BSC tiles in front and behind the HF reduces the ambiguity of measuring the timing of particles. The inner BSC detector tiles are known as disks while the outer tiles are known as paddles [56].

The Beam Pick-Up Timing for experiments (BPTX) are electrodes situated on the LHC at ±175 m from the CMS interaction point. The beams passing through the center induce a charge into the electrodes giving a highly accurate beam timing and position information. The BPTX system is the primary reference for triggering on particle beams passing through CMS. It provides a reliable, zero-bias signal with zero dead-time and is used for triggering several subsequent detectors.

Chapter 4

Simulation and Reconstruction

A generated sample that mimics physical processes based on statistical distributions is also known as a Monte Carlo (MC) sample. The generators that produce these MC samples have parameters that can be tuned to match previously obtained measurement. Once a generator is 'tuned' it can be used to extrapolate a measurement to a region of phase-space not reached by experimental measurements. The use of MC samples allows us to assess detector performance and the state of reconstruction and trigger algorithms prior to the first collisions. In order to accurately evaluate the response of the detector, it is expected that the MC sample properly (or within a certain degree of confidence) reproduces distributions, multiplicities, etc. at the hardware level. Therefore, an accurate and up-to-date detector geometry parameterization must be part of the simulation. A useful approach to bypass the risk associated with possibly incomplete descriptions of the detector response in the simulation software is to embed a signal event into real data collision events.

4.1 Simulation of Z $\rightarrow \mu^+\mu^-$ in Heavy-Ion events

The simulation of a specific physical processes in Heavy-Ion collisions is carried out in steps. Given that the goal of this physics analysis is to measure Z $\rightarrow \mu^+\mu^-$ events in Heavy-Ion collisions, a 'signal' Z $\rightarrow \mu^+\mu^-$ event is generated first. The kinematics of these signal distributions can be constrained to the phase-space where the detector has coverage to maximize the use of computing power. Once the signal events are generated, they will be embedded into a Heavy-Ion event at the sim level, that is when the detector response has been simulated. At the *simulation step* (sim) the response from the detectors prompted by the presence of a particle is After the 'signal' and Heavy-Ion event are successfully merged they can be reconstructed seamlessly as one event.

4.1.1 Z $\rightarrow \mu^+\mu^-$ signal

The generation of the Z $\rightarrow \mu^+\mu^-$ process can be carried out in different ways. A simple PYTHIA *pp* collision simulation can be embedded into a Heavy-Ion event. PYTHIA will generate Z's simulated *pp* events according to the realistic distributions, including regions of phase space not accessible in the current detector configuration. A much simpler and efficient way was to make use of a PYTHIA 'particle gun'. A particle gun is a random generation of a mother particle, following a distribution defined in rapidity (y^Z) and transverse momentum (p_T^Z) space. After the mother particle has been generated it is allowed to decay according to 2-body decay kinematics. To optimize the computing resources the Z's were restricted to only decay into $\mu^+\mu^-$ pairs. The Z's from the particle gun were generated flat in $|y^Z|$ <2.4 and p_T^Z = 0-50 GeV/c. The use of these flat distributions is to uniformly span the relevant phase-space region. A re-weighting of events with a more realistic distribution should is applied later in the analysis.

4.1.2 Heavy-Ion events

The generation of Heavy-Ion events was carried out using the HYDJET generator [57]. HYDJET is a Heavy-Ion event generator that simulates jet production, jet quenching and flow effects in ultra-relativistic Heavy-Ion collisions. The selection on impact parameter was not restricted in the generated Heavy-Ion events in order to obtain a minimum bias distribution of collision centralities.

4.1.3 Z $\rightarrow \mu^+\mu^-$ embedding in hydjet events

The method to combine the signal event into the Heavy-Ion events is known as embedding. The CMS software tool used for this purpose is the *DataMixer*, also used to study detector noise and pile-up events. In order to preserve as much information as possible, the philosophy is to merge the data streams at the earliest stage where the two streams have the same format. In this method a collection of pre-generated events at the SIM level is accessed, for each event the vertex location is found [58]. The signal event is forced to match the same vertex location and generated "on the fly". At the sim level both collections are merged into one. Form this point on, the merged collection will go through the following stages as one.

4.1.4 Z $\rightarrow \mu^+\mu^-$ embedding in real data Heavy-Ion collision events

A more reliable method to evaluate the performance of trigger and reconstruction algorithms is to embed a simulated signal into a real data event. The advantage of this approach is that the uncertainties related to the accuracy of the Heavy-Ion generator are completely removed. The uncertainty related to the accuracy of the hardware detector response remains, but it is greatly reduced because it only affects the decay muons. The detector response includes dead channels, chambers and sectors of the many subdetectors. A minimum bias sample was used for this study. The embedding procedure was the same as described in the previous section. This sample was produced by embedding one Z $\rightarrow \mu^+\mu^-$ event in each minbias event. A comparison between samples (Z $\rightarrow \mu^+\mu^-$ into HYDJET and Z $\rightarrow \mu^+\mu^-$ in real data) is done to ensure the reliability of the Heavy-Ion generator, and discussed in Sec. 5.2.4.

4.2 Reconstruction

The goal of a reconstruction algorithm is to accurately read the event from the information collected from all the subdetectors. The reconstruction, in a general way, depends on the detector configuration and occupancy. The occupancy is dependent on the multiplicity of the events. The main difference between the *pp* collision events and Heavy-Ion events is the increase of multiplicity by a few orders of magnitude of low-momentum particles. The increase in the occupancy is more dramatic in the the innermost detectors, such as the inner tracker and calorimeters. A significant increase of the occupancy is also detected in the forward region of the muon chambers, while in the barrel the 4 Tesla magnetic field prevents most low-p_T tracks from reaching the outermost detectors. The muon occupancy can be seen in Fig. 4.1, the different muon endcap stations are shown where the innermost(ME$\pm$ 1) have the largest amount of reconstructed hits (rechits) in the point closest to the beam axis.

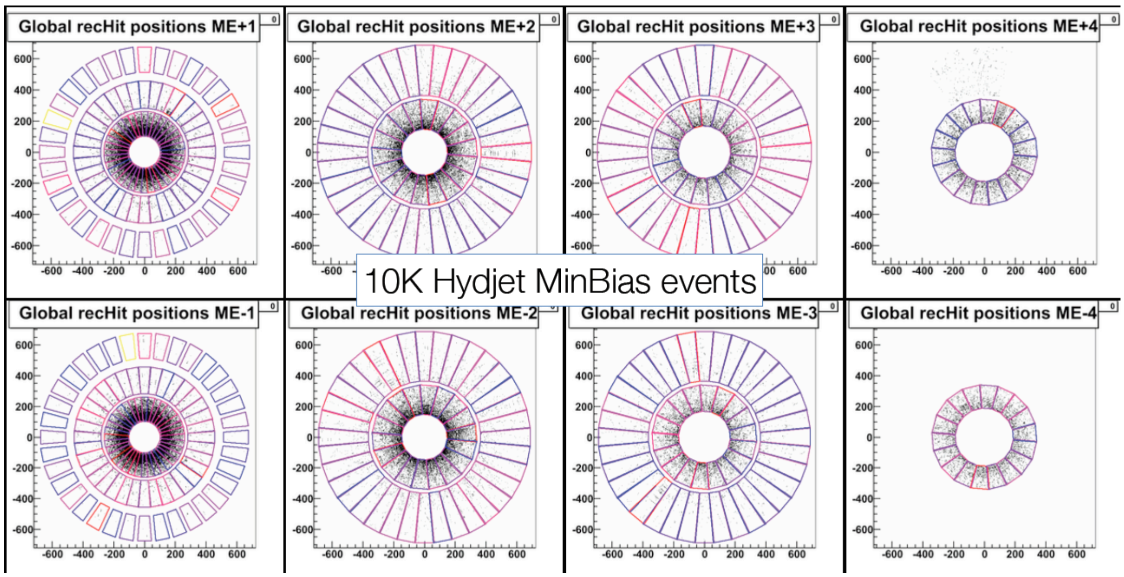

Figure 4.1: Occupancy of in CSC from MC events

The default reconstruction algorithm used for pp collisions is not well suited to deal with the high multiplicity environment. In fact it runs out of memory when deployed in the most central collisions due to large number of combinatorics when creating the tracker tracks. Calorimetry is also affected by the high level of activity, and needs to be properly re-scaled to account for the underlying event. The outside-in approach of the muon reconstruction from the *pp* scenario is already well suited for the reconstruction of muons in Heavy-Ion collisions, modulo the inner-tracker part of the algorithm.

4.2.1 Heavy-Ion Tracking

The Heavy-Ion track reconstruction uses pixel-triplet track seeds constrained to originate from the collision region. Then it makes use of the pattern recognition (CKF) algorithm written for track reconstruction in proton-proton events with settings tuned for

Heavy-Ion collisions [59]. The main differences in Heavy-Ion implementations are:

- Due to the combinatorics in high multiplicity central heavy ion events, only pixel triplets (and not pixel pairs) are used in track seeding;
- The tracking is currently done in a single pass, though recent studies have shown that the standard iterative procedure is very effective in peripheral heavy ion collisions (up to around b=10 fm when the jobs run out of memory). There are plans to develop a set of iterative steps customized to Heavy-Ion needs.

Heavy-Ion tracking sequence

The Heavy-Ion tracking sequence can be briefly described as follows [59]:

- **hiPixelClusterVertex** This step provides a rough estimate of the z-vertex position obtained by maximizing the compatibility of the pixel cluster lengths with their z-positions. This vertex is used to constrain the tracking region for the following step;
- **hiPixel3ProtoTracks** A collection of pixel-triplet tracks (without primary vertex constraint and using a variable-size tracking region based on pixel hit multiplicity) that are the input to the median vertex algorithm;
- **hiPixelMedianVertex** The median vertex is a fast and multiplicity-dependent algorithm. The $\eta - \phi$ window is reduced in central events to allow for fast processing;
- **hiSelectedProtoTracks** A subset of the ProtoTracks collection consisting of those that are compatible with the median vertex z-position and beamspot transverse position. These are inputted to the slower but more precise 3-d adaptive vertex fitter (next step). The minimum p_T of the selected prototracks is variably dropped from 1.0 to 0.075 GeV depending on the pixel hit multiplicity, so that peripheral events have more tracks from which to make the vertex;
- **hiPixelAdaptiveVertex** The collection of vertices calculated using *hiSelectedProtoTracks* selected based on the z-vertez compatibility;

- **hiBestAdaptiveVertex** Contains only the adaptive vertex with the most associated tracks ;
- **hiSelectedVertex** The same as above unless the adaptive algorithm failed (e.g. not enough prototracks), in which case the median vertex is used. If that fails the beamspot is copied as the "selected vertex". The associated errors are also copied over. The beamspot can reach a statistical precision of $2\mu m$ [60];
- **hiPixel3PrimTracks** The collection of pixel-triplet tracks that are constrained to originate from a tracking region around the selected vertex from the previous step;
- **hiPixelTrackSeeds** Generated from the above pixel tracks and used to seed the full tracking;
- **hiPrimTrackCandidates** These are the track candidates from the trajectory propagator through the strip tracker;
- **hiGlobalPrimTracks** The output of a global covariance fit to the above candidates;
- **hiSelectedTracks** A subset of the above that pass some track quality cuts, such as compatibility with vertex, number of hits, etc.;

In order to minimize the contribution of fake and non-primary tracks while maintaining relatively high efficiency in the highest track density environment, additional quality selection were applied to the tracks from the $hiGlobalPrimTrack$ (Sec. 5.2.4) collection in the standard Heavy-Ion tracking collection.

4.2.2 Vertex

To calculate the vertex in Heavy-Ion events, the first step is to get a rough estimate of the z-vertex position by stepping through from -20 to 20 cm and determining the compatibility of the pixel cluster lengths with the vertex hypothesis. For each step, the number of compatible hits based on the cluster length is calculated. The z-vertex step with the maximum in the number of compatible hits is called the 'cluster vertex'. After finding the cluster vertex, one initiates the track reconstruction of the pixel-triplet tracks. Fig. 4.2 shows the vertex z distribution in data and MC.

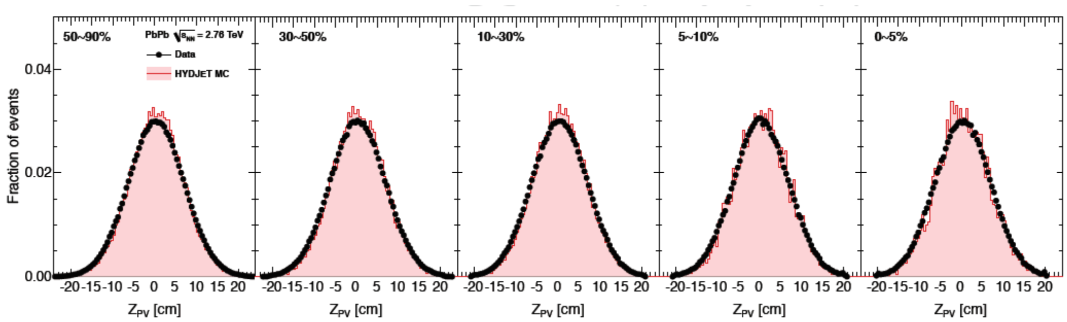

Figure 4.2: z-vertex position from HYDJET and data events in different centrality classes.

A data-driven vertex resolution study was carried out by dividing all the tracks in a single event into two sub-events. The difference between the vertices reconstructed from the two sub-events is related to the resolution in x, y, and z. Figure 4.3 shows the x-axis vertex resolution vs. the number of tracks.

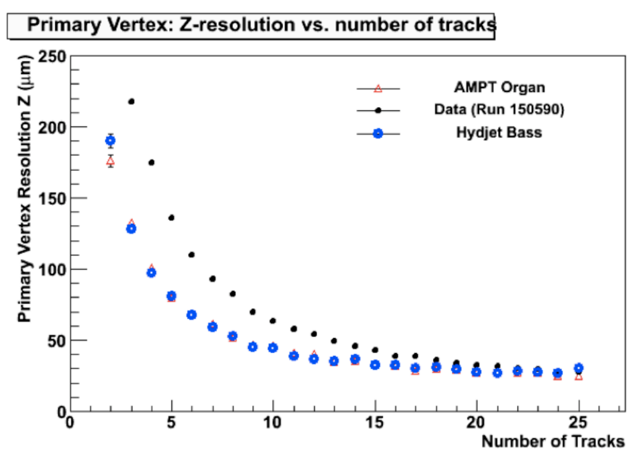

Figure 4.3: z-vertex position resolution vs number of tracks, with AMPT, HYDJET and HI data samples

4.2.3 Centrality

The centrality variable is calculated based on HF energy deposits which are classified according to their fraction of the total inelastic cross-section. Extensive details can

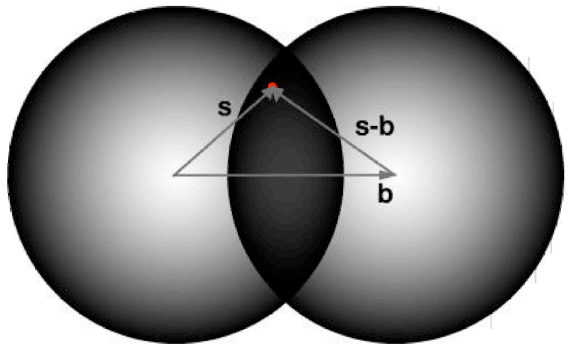

Figure 4.4: Overlap region of two nuclei

be found in [61]. Heavy-Ion collisions can occurr at a range of impact parameters, form head-on collisions to grazing interactions. Given the geometry of each of the colliding nuclei, approximated as spheres with a density profile, a geometrical overlap can characterize the centrality of the collision. The distance between the two centers of the spheres is the impact parameter, b. The overlap region is the "almond-shape" area, where the two colliding nuclei are superimposed as seen from the beam axis, Fig. 4.4. The overlap region is represented by the overlap function T_{AB}.

$$T_{AA}(b) = \int d^2 s T_A(s) T_A(b-s) \tag{4.1}$$

where $T_A(s)$ and $T_A(b-s)$ are the nuclear profile functions, based on Wood-Saxon parameterizations, for nuclei A and B. Integrating Eq 4.1 over all impact parameters we get the normalization.

$$\int T_{AA}(b) d^2 b = 1 \tag{4.2}$$

Now, the probability to have n inelastic baryon-baryon collisions at an impact parameter b is given by

$$P(n,b) = \begin{pmatrix} A^2 \\ n \end{pmatrix} [T(b)\sigma_{pp}]^n [1 - T(b)\sigma_{pp}]^{A^2-n} \tag{4.3}$$

where the first factor represents the number of combinations for finding n collisions out of A^2 possible nucleon-nucleon encounters. The second factor gives the probability of having exactly n collisions, while the third factor is the probability of having exactly A^2 -n misses. The total inelastic cross-section is :

$$\sigma_{AA} = \int db \Big\{ 1 - [1 - T(b)\sigma_{pp}]^{A^2} \Big\} \tag{4.4}$$

The experimental determination of centrality allows for the characterization of the events. Once the experimental value of the centrality variable is obtained it can be combined with information obtained "*a priori*" about a geometrical model to infer variables such as b, N_{part}(number of participant nucleons), and N_{coll} (number of colliding nucleons). The can be defined as follows:

$$\langle N_{coll} \rangle(b) = \sigma_{pp} \cdot A^2 \cdot T_{AA}(b) \tag{4.5}$$

$$\langle N_{part} \rangle(b) = 2A \int d^2 s T_{AA}(s) \Big\{ 1 - \Big(1 - T_{AA}(s-b)\sigma_{pp} \Big)^{A^2} \Big\} \tag{4.6}$$

where σ_{pp} is the cross-section of a proton-proton system at the same center of mass energy.

Experimental determination of centrality classes

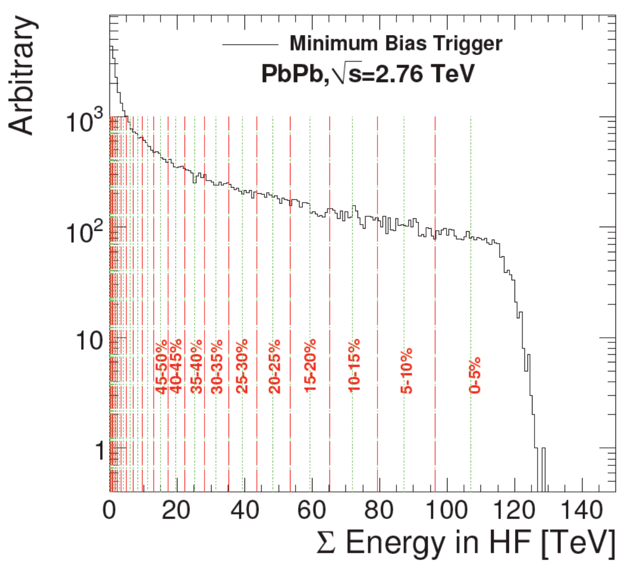

Figure 4.5: HF energy distribution in centrality bins

The event centrality in nucleus-nucleus collisions can be determined by measuring the charged particle multiplicities or the transverse energies in various regions of pseudo-rapidity. The signals can be divided in centrality bins to provide a measure of centrality. In CMS the centrality of the event is inferred from the transverse energy deposited in the Hadron Forward calorimeters with coverage $3< |\eta| < 5.2$. The energy on both sides of the detector is summed up. As a cross check, the pixel detector multiplicity is studied, since it increases monotonically in the same fashion as the HF signals. The number of spectator neutrons released from the interaction is measured by the ZDC, which is negatively correlated in central events. Once the total transverse energy is collected by the HF, it is assigned a centrality bin when compared to the integrated sample. Fig 4.5 shows the centrality bin classes in a HF energy distribution. Using the HF energy-sum limits shown in the figure, one can define bins with equally normalized fractions of the minimum bias cross section, which serve as centrality classes for subsequent analysis. The resulting distribution should be flat for a minimum bias data sample by construction, as shown in Fig 4.6. As it can be seen the centrality bin are assigned $1/40^{th}$ of the cross-section each.

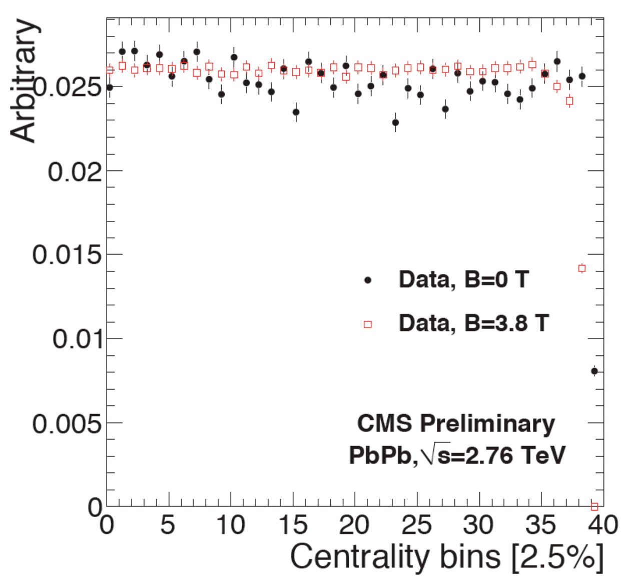

Figure 4.6: Centrality bins in MinBias events

4.2.4 Muon Reconstruction

Since it is a massive (compared to the electron) lepton, a muon with enough p_T to overcome the magnetic filed can make it to the outermost detectors leaving information in all the relevant systems along the way. The muon reconstruction combines inner tracking information with the information collected by the muon chambers, and some calorimetry for specific cases. Muons can be though of as massive electrons that can be traced in the tracker and leave a minimum ionization signature in the ECAL, and no signal in the HCAL. The muon sub-detectors can track the muon trajectory outside the return yoke. The muon reconstruction is carried out in steps: it starts with the local reconstruction of 'tracklets' or segments in each of the muon sub-system and tracker as explained in Sec 4.2.1. Then the information of the muon systems is combined to form a stand-alone (SA) muon. Finally the SA muon trajectory is matched to a track from the tracker for form a Global muon.

Local Reconstruction

The local reconstruction begins with the identification of a signal left by a traversing particle. Proper interpretation of these signals can be turned into reconstructed hits having a 3-dimensional location. The association of the reconstructed hits into a trajectory, forms a segment. The local reconstruction in the CSCs begins with the identification of a pulse in a strip, followed by the cluster hit reconstruction. By identifying the cluster of hits in a CSC layer the strip with the greatest ADC count is found. Using this as the central strip, the two on each side are also included as a hit cluster. The pulse is fitted with a Gatti distribution. The Gatti distribution is not exact since it does not take into account effects due to drift, time dispersion, and non-normal incidence of tracks, but is has been shown in Refs. [53] and [62] to be less biased. Before fitting, a wire group is associated with each strip. The local y-coordinate is found of the intersection of each strip within a wire group with a signal. The local x-position is found by the minimization of the χ^2 from the Gatti fit of the pulse distribution. Each of the 6 layers of a chamber provides an independent 2-dimensional reconstructed hit (*rechit*). The *rechit* are fitted to form a linear segment. In the case of the CSCs a segment must have at least 4 hits. Only hits reasonably close (within

2.5 mm in $r\phi$) [63] to the line are considered. The hits associated to a segment are flagged as 'used' and the procedure is iterated.

The local reconstruction of points in the DT is done by obtaining the distances with respect to the wire multiplying drift time by drift velocities. The reconstruction relies on a time-to-distance parameterization of the cell behavior. The measure x_{drift} is computed as a function of (i) the drift time (t_{drift}), (ii)parallel and perpendicular components of the magnetic filed with respect to the wire in the radial direction($B_{\|}$ and $B_{\perp}$) and (iii) the incidence angle with respect to the direction of the chamber (α). The component of the magnetic field parallel to the drift lines can be neglected since it has no measurable effect on the drift time. $B_{\|}$, $B_{\perp}$ and α are not known at the level of the individual hit, a 3-step reconstruction algorithm is implemented. First step assumes a crude estimate of the impact angle and the hit position along the wire. The hits are updated twice: after they have been used to build a 2D $r-\phi$ or $r-z$ segment, and after it has been used in the 3D segment fit. A segment is built from aligned hits, this is starts from a pair of hits that must point in the nominal direction of the interaction region. The best segments amongst those sharing hits (solving conflicts, suppressing ghosts) are selected. The hit reconstruction is updated using information from the segments. Finally a quality criterion is applied to require $\chi^2/\mathrm{ndf} < 20$ and number of hits ≥ 3.

The local reconstruction in the RPCs is made out of points in the plane of the detector. First, a clustering procedure starting from all strips that carry signals is performed. By grouping all the adjacent fired strips, a reconstructed point is defined as a center of gravity of the area covered by the cluster of charges. It is assumed that each group of strips is fired due to a single particle crossing, and that the actual trajectory could have traversed anywhere with a flat probability over the area covered by the strips of the cluster.

Stand-alone Muons

Once each of the sub-detectors has read the signals left by a traversing muon, and these have been turned into segments in each of the chambers, the information is combined to make the stand-alone muon object. The SA tracking algorithm combines reconstructed track segments and hits using a Kalman filter technique [62] to reconstruct muon trajectories. The track segments are extrapolated taking into account muon energy loss in the material, multiple scattering and non-constant magnetic field. The propagation of the measurement is inside-out at the beginning, collecting hits at each measuring surface of the detectors. First, from the two innermost measurements, trajectory parameters are calculated. These parameters are extrapolated to the next measuring surface and combined with the measurements there. This is done recursively until the outermost layer is reached. The propagation is then reversed to an outside-in direction. A smoothing algorithm is used to incorporate the full information and remove background hits [53]. The final track parameters and their errors are delivered at the innermost muon station. Muon tracks are then propagated through the calorimeters to the nominal vertex position in order to assign a p_T value at the interaction point. The SA muon reconstruction efficiencies are shown in Fig. 4.7.

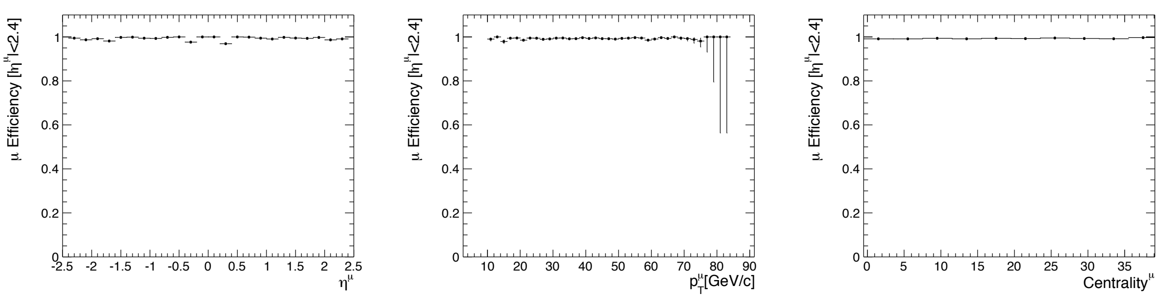

Figure 4.7: Single stand-alone muon reconstruction efficiency from Z $\rightarrow \mu^+\mu^-$ embedded in minbias HYDJET as a function of ,p_T (left), pseudorapidity (center) and centrality bin(right)

Global Muons

The global muon reconstruction takes the stand-alone muon trajectories and extends them to include the tracks in the tracker. The SA muon trajectory is taken at the innermost muon station and extrapolated to the outermost surface of the tracker taking into account energy loss and multiple-scattering effects. The extrapolated trajectory will be used to define an $\eta - \phi$ 'region of interest'. Each of the tracker tracks, specifically the collection 'hiGlobalPrimTracks' defined in Sec. 4.2.1, that are within the region of interest are compared one-by-one to the standalone muon trajectory. For each "tracker track"-"standalone muon" pair an overall fit is performed. The overall fit is performed with the Kalman filter, taking into account energy loss and multiple-scattering effects. The best global muon is selected.

The global muon reconstruction efficiencies are shown in Fig. 4.8. The efficiencies are obtained from a Z $\rightarrow \mu^+\mu^-$ decay embedded in a HYDJET event sample. The distribution of reconstructed muons is normalized by the number of generated muons with $|\eta| \leq 2.4$ and $p_T \geq 10$ GeV/c. It can be observed that the standalone muon efficiency is saturated at one over all the single muon pseudorapidity, single muon p_T, and event centrality phase space. The global muon reconstruction exhibits a flat distribution as a function of muon p_T, a slight dependence as a function of event centrality. As a function of muon pseudorapidity the efficiency shows a plateau in the barrel region($|\eta| \leq$0.8), and decreases with increasing muon pseudorapidity.

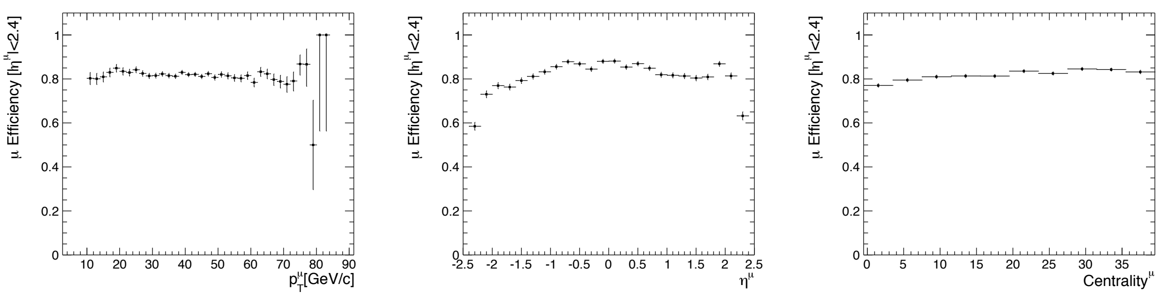

Figure 4.8: Single global muon reconstruction efficiency from Z $\rightarrow \mu^+\mu^-$ embedded in minbias HYDJET as a function of ,p_T (left), pseudorapidity (center) and centrality bin (right)

The overall reconstruction of a muon trajectory can bee seen in Fig. 4.9, where the solid blue line is indicative of a global muon. The red line is indicates the trajectory of an electron reconstructed in the tracker. A charged hadron (green line) leaves a signal in the tracker and deposits its energy in the HCAL. A neutral hadron is identified by the energy deposited in the HCAL without a trajectory in the inner tracker, indicated by the green dashed line. Finally, a photon leaves no signal in the tracker and deposits its energy in the ECAL.

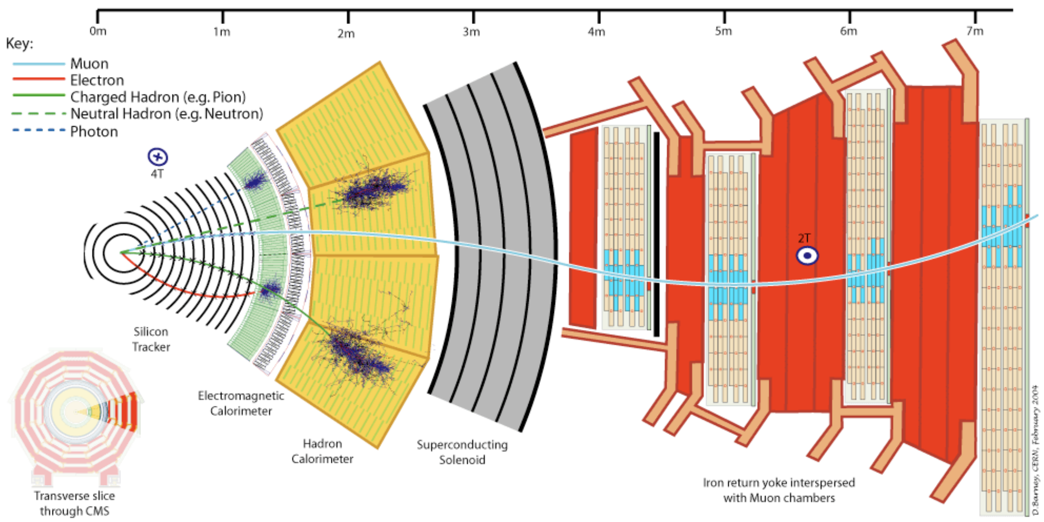

Figure 4.9: CMS slice showing the trajectories of muon, electron, charged hadron, neutral hadron and photons

Dimuons

The reconstruction of Z^0 is done by requiring two opposite-charge global muons in the event. Each muon must pass a series of quality cuts. Furthermore, an extra constraint is imposed on the dimuon pair to beat down random background that might fake two muons. The vertex probability test evaluates the compatibility of two tracks to originate from the same vertex. The vertex probability is calculated using the χ^2 and the number of degrees of freedom of the vertex. The calculated probability is that an observed χ^2 exceeds the value χ^2 by chance, even for a correct model[64].

4.3 MC truth Matching

In order to estimate the the performance of the reconstruction algorithms and perform readout studies it is important to have a handle over the generated information. The simulation step directly precedes the reconstruction step, the sim hits are used as seeds to start the reconstruction algorithms. Once the entire reconstruction chain has been executed the information can be compared with the simulated data that was put in. In high multiplicity events many tracks can be close together in $\eta - \phi$ space and have similar tranverse momenta, which make very difficult to associate tracks based solely on kinematical parameters. A better approach is to unambiguously match the reconstructed object to the simulated object, and vice-versa, on a hit-by-hit basis.

4.3.1 Muon association by Hits

The Muon Association By Hits (MABH) is a package that is used to do the aforementioned hit-by-hit comparison between reconstructed and simulated objects. The idea is to take the 3D location of the reconstructed hits that make up the reconstructed object and compare them with the 3D location of the simulated hits from the simulated track. With this information one makes a one-to-one map between sim and reco objects. In order to calculate efficiencies each simulated track is compared with the collection of reconstructed tracks. If a simulated track is found to have a match in the reco collection it is considered to be successfully reconstructed. A reco-to-sim approach is generally used to perform fake rate studies. The MABH can associate global muons in a modular fashion, allowing one to characterize the silicon tracker reconstruction and the stand-alone muon reconstruction separately.

Criteria

The criterion to consider a successful match depends on what percentage of hits are matched between the reco and sim object. The quality of the match is given in a range form 0 to 1. A quality of 1 means that all the hits in the simulated track were found to have a match in the reconstructed object. A quality of zero implies that the specific simulated track does not share any hits with a given reconstructed track. This criterion can be evaluated separately for the 'tracker' part and the 'muon' of a global muon, both quality levels are set to 0.75 or higher. The advantage of requiring that each part meets the 75% criteria as opposed to an over-all 75% approach, is that with the former requirement it can also be ensured that tracker track is properly reconstructed.

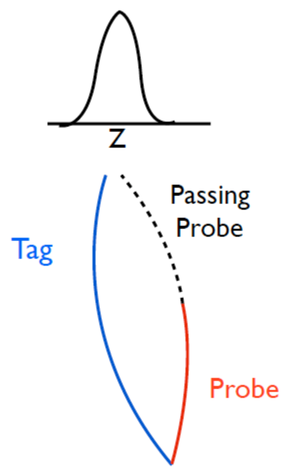

Figure 4.10: Tag and probe diagram with Z mass resonance

4.4 Tag and Probe

Tag and probe is a data driven technique to calculate efficiencies with a "modular" approach. One of the main advantages of the *tag-and-probe* method is to avoid large systematic error due to imperfections in modeling of the data and the detector response. This is done by measuring the efficiency from the data itself with no reference to simulation. This method utilizes known mass resonances (e.g. J/ψ, Υ, Z) to select particles of the desired type and probe the efficiency of a particular selection criterion on those particles [65]. The Tag is an object that passes a set of very tight selection criteria designed to isolate the required particle type (in this case a muon). The fake rate for passing tag selection criteria should be very small (<<1%). A generic set of the desired particle types known as $probes$ is selected by pairing with the $tags$ such that the invariant mass of the combination is consistent with the mass of the resonance. Combinatoric backgrounds can be subtracted with a fit or a sideband subtraction. The definition of *probe* depends on the specifics of the selection criterion being examined. The efficiency is measured by counting the number of *probe* particles that pass the desired selection criteria :

$$\epsilon = \frac{N_{passingprobes}}{N_{allprobes}} \tag{4.7}$$

where $N_{passingprobes}$ is the number of probes that pass the selection criteria and $N_{allprobes}$

is the total number of probes counted using the resonance. Figure 4.10 shows a simplified diagram of the Tag and probe method. The *tag* (blue line) is selected with a tight selection criteria, the a collection of probes with a looser criteria is selected. The *tag* gets paired with every probe and only the one that make the Tag-Probe pair add to mass of the resonance (Z mass) will be considered. Now, the efficiency to be calculated by the ratio of how many probes satisfy the requirements to complete the black dashed line, divided by the number of all the probes.

The *tag-and-probe* method can be used to calculate different efficiencies depending on the definition assigned to the tags and probes. The efficiencies can be separated in a "modular" fashion to account for each of the steps needed to calculate an overall efficiency. In the case of the global muon reconstruction is can be divided like:

$$\epsilon_{GlobalMuon} = \epsilon_{trackerTrack} \times \epsilon_{matching} \times \epsilon_{muonTrack} \tag{4.8}$$

where $\epsilon_{trackerTrack}$ is the efficiency to reconstruct the inner track of a muon, $\epsilon_{muonTrack}$ is the efficiency to reconstruct the outer part of the muon and $\epsilon_{matching}$ is the efficiency to match an inner track with the muon track.

Chapter 5

Analysis Details

5.1 CMS Heavy-Ion setup

The high multiplicity environment produced in $PbPb$ collisions, required the detector to adopt a setup optimized for such events. Some of the subsystems were required to make changes (with respect to the pp setup) in the readout schemes to accommodate the needs of various Heavy-Ion analyses. The main issues that were addressed were: data formats, firmware limitations, and level-1 triggering. In the pixels the main modifications were done to the zero suppression algorithm and firmware. For the silicon strips a different zero suppression algorithm was used and data were collected in the virgin raw mode. For the ECAL selective readout schemes were also implemented. The muon system does not present such a big increase in the occupancy compared to pp collisions, however the L1 configuration for the CSC was adjusted to cope with a higher fake rate.

5.1.1 Readout

During preparation for the Heavy-Ion run, some concerns regarding the readout strategy for the CSC were addressed. The forward muon chambers present a higher activity in the $PbPb$ environment as can be seen in Fig 4.1. This activity is due to the large number of hadrons that make it to the first chambers with enough p_T to penetrate only a few layers. Most of these particles hit the forward-most chambers, ME1/1, and do not make it to the next layer. The large number of punch-throughs has a direct impact in the number of level-1 triggers coming from the CSCs. The CSC track finder (CSCTF) is an algorithm that is in charge of connecting track segments into a full track (Sec. 4.2.4) and assign a p_T, η and ϕ value to it [53], achieving a p_T resolution of 25% [66]. At the time of pp running, the configuration for the CSCTF required to have a muon trigger candidate with at least one segment, also known as 'singles'. This configuration was optimized to trigger on low-p_T forward muons for the b-physics analyses. This loose criterion used to trigger on muon stubs would have resulted on a very high rate of CSCTF triggers in Heavy-Ion collisions. In order to reduce the rate of punch-thorughs, the 'singles' requirement was removed. Instead, a 'coincidence' requirement was implemented, requiring different chambers to having hits consistent with the assumption of coming from the same track, to satisfy the CSC track finder.

Given the data sizes expected in the most central collisions, the data flow in the CSCs was under review to detect possible bottle-necks. Estimates made with MC samples indicate that, with an expected minimum-bias event rate was of the order of ≈ 100 Hz the data sizes were calculated to be well under the maximum limit restricted by the front end boards (FEBs). A direct comparison of the estimates of the data volume generated by the number of $recHits$ and segments for minBias events in pp collisions at $\sqrt{s}$= 7TeV and $PbPb$ collisions $\sqrt{s_{NN}} = 2.76$ TeV is shown in Fig 5.1 and Fig 5.2.

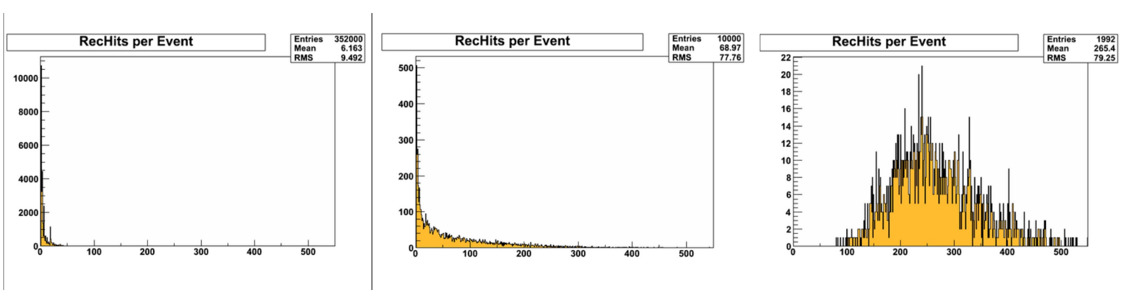

Figure 5.1: Comparison of recHit multiplicity for minbias pp (left), minbias $PbPb$ (center) and $PbPb$ central events(right)

The mean increase in $recHits$ and segment multiplicity in the CSCs is about a factor of 3-4× when comparing minBias pp and $PbPb$ events. However, the mean multiplicity for central (impact parameter set to zero) $PbPb$ events is significantly higher. Central

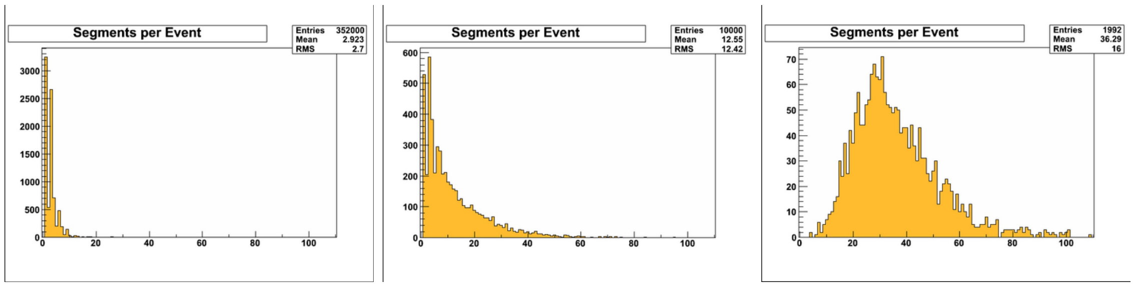

Figure 5.2: Comparison segment multiplicity for minbias *pp* (left), minbias *PbPb* (center) and *PbPb* central events(right)

events are rare. Furthermore, even at the high-end tail of the distribution, the data volume is well under the max alloted by the front end electronics. Therefore, it was deemed safe to continue with the current, at the time, CSC readout scheme for the 2010 Heavy-Ion run.

5.2 Heavy-Ion collisions

The November-December 2010 PbPb run was the first Heavy-Ion run at the LHC. The constantly-evolving conditions of the accelerator meant that the CMS detector had to be prepared for different trigger scenarios. The continuous increase in the instantaneous luminosity translates into an increase of the rate of data being recoderd to tape. This can be seen in Fig 5.3. The number of bunches delivered by the accelerator increased from 1×1 to 129×129. ThE total number of triggered minimum-bias events was $N_{MB} = 53\ 584\ 437$. As discussed in Sec. **??**, the minimum-bias trigger was based on E_T measured in the HF calorimeters. The minbias trigger efficiency, ϵ_{MB}, was calculated using a simulation of the response of the HF in HYDJET events, and was found to be 97± 3% [61]. This results in 55 241 688 delivered minimum-bias events after correcting for trigger efficiency[1]. The trigger efficiency was cross-checked with a technique based on the number of good pixel hits. Further details given in Sec. **??**. The total integrated luminosity delivered was $\mathcal{L} = 7.2\ \mu b^{-1}$ assuming $\sigma_{PbPb} = 7.65$ b.

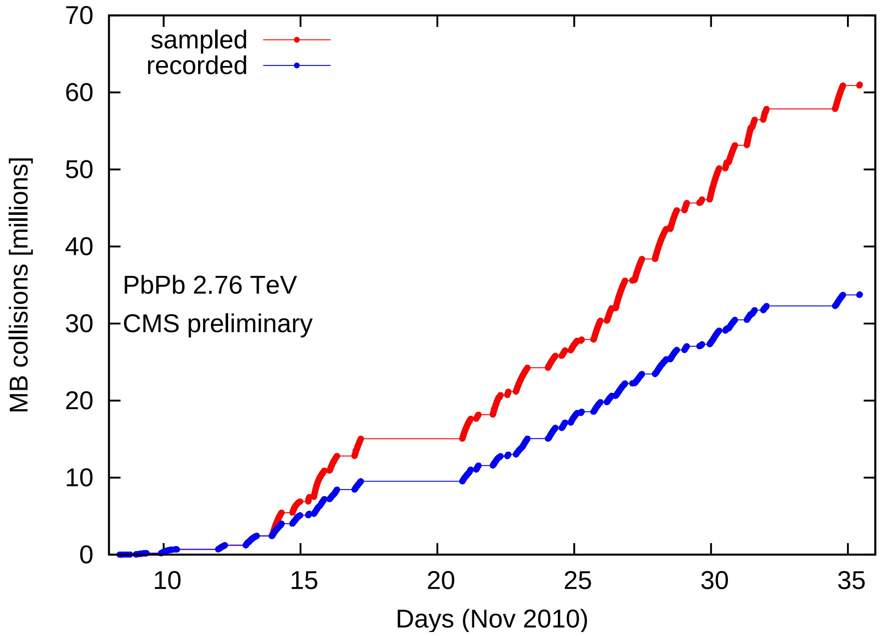

Figure 5.3: Total number of equivalent minimum-bias, in red sampled and in blue recorded by CMS.

5.2.1 Data flow schemes

In order to optimize the resources and the availability of the data for analysis a multi-stream strategy was devised. The data was divided into 3 different streams, a Data Quality Monitor (DQM) stream, a minimum-bias stream and Physics-Analysis stream. All these streams had a different purpose. The DQM stream is the smallest of the three and it was used to feed the DQM framework in order to validate and monitor the data as it was flowing from the detector. The requirement of this data was to have a quick turnaround time and to take a small fraction of the bandwidth. The minimum-bias stream was the one occupying the largest fraction of the bandwidth. This sample contained the main minimum-bias trigger selection with some pre-scales as necesary. This stream, being the largest one of the three had the largest delay due to reconstruction. Its main purpose was to be used for longer time-scale analyses. The third stream was designed to have a so-called *core physics* selection. This stream was fed by triggered data, such as the dimuon triggers used for this work. It was setup to be promptly reconstructed and analyzed. It started from a minbias selection, followed by a specific physics analyses triggers. The configuration to build the *core physics* stream was designed to maximize the number of useful events for analysis while keeping the bandwidth to the allocated fraction. This was a challenging task as the instantaneous luminosity delivered by the LHC changed on a daily basis.

5.2.2 Triggering

The CMS detector has different ways to trigger on events, making use of the different subsystems. The main objective is to distinguish the activity captured by the detector coming from collisions to the one coming from noise, cosmics, beam background and other non-collision related activity. The sequence implemented to suppress non-collision activity starts from a minbias L1 trigger selection. This is followed by a specific sequence of physics-related triggers. For this analysis the sequence included single and double muon triggers. The minbias and muon trigger are executed *online*, that is, as the event data is being readout the trigger system makes a decision to either keep or reject the event. After triggering, *offline*, a series of event selection cuts are applied. Finally, specific quality cuts were implemented at the analysis level.

Minimum-Bias Trigger

The minimum-bias trigger used information from the HF and BSC. The minimum-bias trigger relied only in the BSC up to run 150593 (inclusive). The trigger required coincidence, that is, that the detectors should have activity on both sides. In addition, a bunch crossing identified by the BPTX was required. The coincidence requirements on the BSCs were set to look for at least one segment to fire on each side, dubbed 'threshold 1'. The BSCs have 16 segments on each side (32 total), from which 31 were operational. Most (75%) of the collisions illuminate all 31 segments, thus making the effect of one dead segment negligible [67]. After run 150093, the minimum-bias trigger incorporated information from the HF as an "OR" operator. The HF trigger required at least two towers that had deposited energy exceeding the firmware threshold. Compared to the BSC trigger, the HF trigger was also noise-free, but offered a better efficiency to identify minimum-bias collisions. In addition, the HF trigger offered a better overlap with the offline event selection. The combination of the two trigger bits provided a robust and more reliable net to "catch" hadronic *PbPb* collisions. Having the HF requirement as an "OR" with the BSC coincidence provided a measure of redundancy in case any hardware problems presented themselves.

Muon Triggers

The triggering system is organized in levels where each provides a selection to further reduce the data volume. Trigger candidates passing the level-1(L1) stage move on to the level-2(L2) trigger and to level-3(L3), the latter two compose the High Level Trigger(HLT). The level-1 trigger analyzes every bunch crossing. The L1 trigger decisions are made by programable hardware electronics, while the HLT is a software system implemented in a farm of about a thousand processors using reconstruction software similar to one used in the offline analysis. A series of single muon triggers can be deployed depending on p_T threshold and quality of the triggered muon. The level-1 muon trigger makes use of the CSC, DT and RPC sub-detectors. The DT and CSC electronics first process the information from each chamber locally. A position and angle per muon station is delivered for every muon that crosses a station. Vectors from different stations are combined to form a muon track and to assign a transverse momentum value. The RPCs deliver their own track candidates based on regional hit patterns. The information of the three sub-systems is combined achieving an improved momentum resolution and efficiency. The four highest-$p_T$muons from each subsystem are selected for further processing. Finally, the muon p_T thresholds are applied [53]. The L1 muons serve as seeds for the L2 muons. The L2 algorithm reconstructs hits from the muon sub-systems and constructs tracks using the Kalman Filter technique [68]. The resulting trajectories are used to refine the resolution of the measured muon kinematics.

Various L1 triggers were used during the 2010 Heavy-Ion run. These included triggers which selected muon with $p_T$thresholds at 3, 5, 15 and 20 GeV/c. The L2 p_T thresholds used were 3, 5, and 20 GeV/c.

Dimuon Triggers

Dimuon triggers are also implemented at different levels of the triggering system. For this analysis two dimuon triggers were used. One used L1 muons, and simply required the presence of two in one event, regardless of their p_T. No RPC information was required. These events were dubbed "L1DoubleMuOpen". A second trigger used L2 muons, requiring the presence of two in one event, with the additional condition that each had $p_T \geq 3$ GeV/c. The RPC information was used in this case. These events were dubbed "L2DoubleMu3".

The low luminosity at the beginning of the Heavy-Ion run allowed for less restrictive. The double muon trigger $L1DoubleMuOpen$ requires two muons that leave a signal that is read by the muon hardware systems. This makes it a very efficient algorithm and also very susceptible to background noise and punch-throughs. This is due to the fact that hadrons can have just enough energy trigger the muon hardware systems. As the performance of the accelerator improved, the instantaneous luminosity increased, requiring a more restrictive double muon trigger to fit in the allotted readout bandwidth. The $L2DoubleMu3$ trigger is more selective than the $L1DoubleMuOpen$ in three aspects. It implements the L2 muon algorithm which makes use local muon reconstruction similar to the stand-alone muon described in section 4.2.4. This allows for a better resolution in the kinematic parameters to be achieved. This trigger requires coincidence in the muon trajectories found by the DT and CSC with the trajectories found by the RPC. Since the data obtained from this trigger sample was mainly used for the Z $\rightarrow \mu^+\mu^-$ analysis, a p_T threshold of 3 GeV/c was also used to keep the readout volume under control. This cut has a negligible acceptance effect for muons coming from a Z decay.

Figure 5.4 shows the centrality distribution of events that fired the minbias trigger (black histogram). The fraction of the hadronic cross section is integrated starting from the most central (near-zero impact parameter) events. By construction the bin widths are constructed to contain equal fractions of the total hadronic cross sections, resulting in a flat shape in the figure. The *DoubleMuOpen* triggered event distribution (red, hashed histogram) shows that the majority of these events come from the most central collisions. Since the main sources of dimuon in the CMS acceptance scale with the number of hard

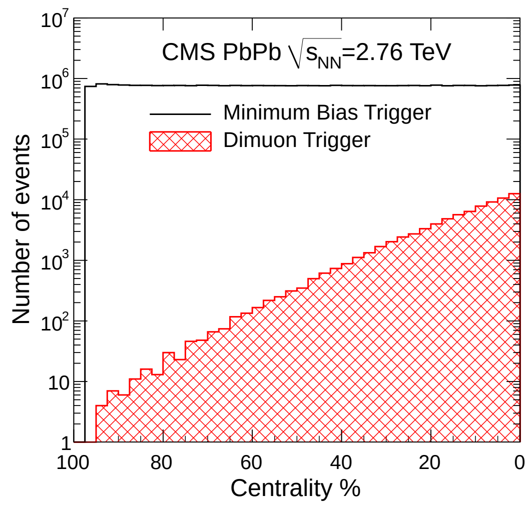

Figure 5.4: Centrality distribution for minimum-biasand dimuon triggered events.

collisions.

Dimuon Trigger Efficiencies

The trigger efficiencies were obtained with a data driven method known as *tag-and-probe* (Sec. 4.4). Figures 5.5 and 5.6 show the trigger efficiency for the $L1DoubleMuOpen$ and $L2DoubleMu3$, respectively. The efficiencies were calculated using different samples to estimate the systematic uncertainty and check for consistency. The $L1DoubleMuOpen$ trigger efficiencies were obtained from a Z $\rightarrow \mu^+\mu^-$ event embedded in a Hydjet minbias sample(red squares) and also embedded in a minbias selection of HI data (blue triangles). The efficiency is shown as a function of muon η (with a $p_T \geq$ 10 GeV/c selection) and muon transverse momentum. The efficiency of this trigger is very close to unity and shows a flat distribution in the full η acceptance and in the p_T [10- 80] GeV/c. After run 150593 the trigger setup was changed to $L2DoubleMu3$. This trigger shows a slightly lower efficiency than $L1DoubleMuOpen$ trigger. The same features are observed as a function of muon η. As function of p_T a turn-on curve that saturates at $\approx$ 98% after 10 GeV/c. The trigger efficiency obtained using the data-driven *tag-and-probe*method is also shown for in black squares and single-muon-triggered data in open circles.

As can be seen in Fig. 5.6, the efficiency obtained from single-muon-triggered data (open circles) is lower in the p_T range from 10-20 GeV/c compared to the distributions obtained in the other samples. The single-muon-triggered data efficiency was calculated by obtaining the ratio between reconstructed muons matched to the $L2DoubleMu3$ trigger primitives divided by all the reconstructed muons with high quality cuts shown in table 5.1. Most of the muons that populate this distribution are in the lower p_T range [10- 20 GeV/c]. However, the muons from a Z^0 decay have a higher p_T, where there is a better agreement in the results across the four different samples. For the purpose of this analysis the difference in efficiencies will not be considered as a systematic error, instead the only the error bars on the *tag-and-probe* will be used. This is done in order to obtain the uncertainty limitation directly from data, as opposed to relying on MC.

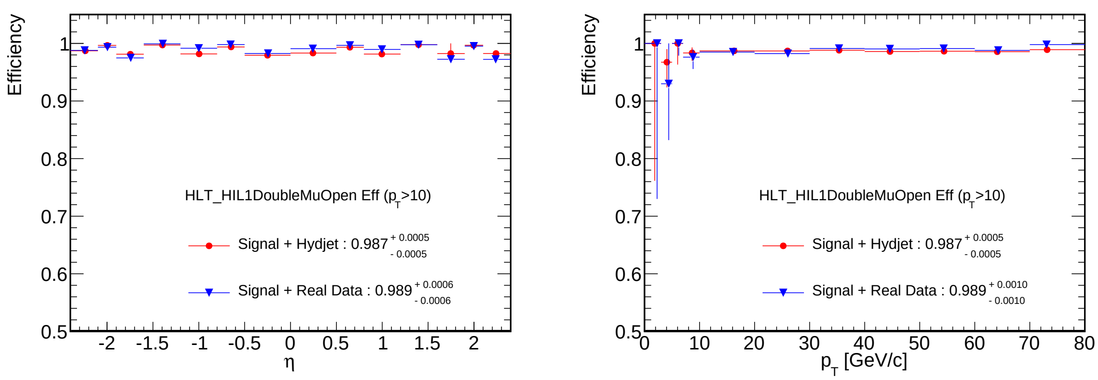

Figure 5.5: Efficiency for single muons from a L1 dimuon trigger as a function of muon η (left) and p_T (right). Efficiencies obtained from: signal embedded in HYDJET (red) and signal embedded in HI data (blue)

In order to calculate the trigger efficiencies using the *tag-and-probe* method the following definitions were used.

- Tag: A global muon, matched to a single muon trigger with a p_T threshold of 20 GeV/c.
- Probe: A global muon passing the quality cuts, to ensure a well defined *probe*.
- Passing probe: A probe that is matched to either the $L1DoubleMuOpen$ or $L2DoubleMu3$,

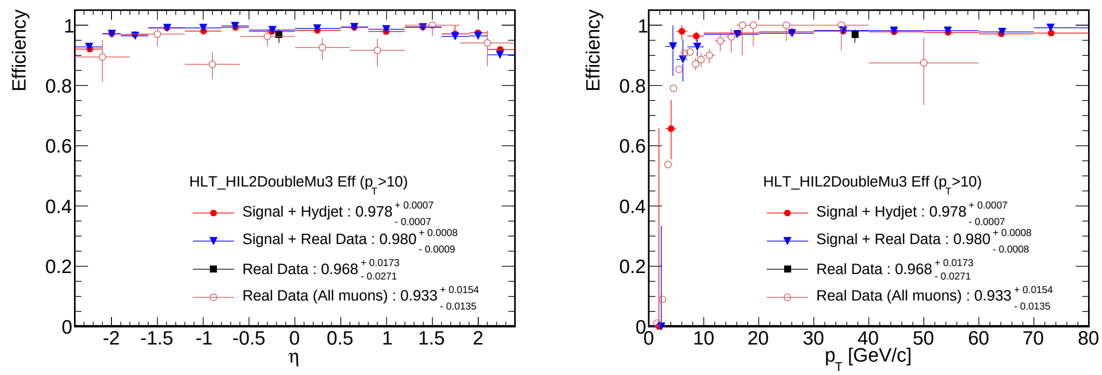

Figure 5.6: *Tag-and-probe* efficiency for single muons from a L2 dimuon trigger as a function of muon η (left) and p_T (right). Efficiencies obtained from: signal embedded in HYDJET (red) and signal embedded in HI data (blue), dimuon triggered data (black) and single muon triggered data (open red circles)

depending the stage of the run.

To avoid introducing a trigger bias, the sample was first filtered on the single muon trigger that is matched to the L2-single muon trigger with a 20 GeV/c p_T threshold. To have a pool of events in which to sample only the trigger efficiency. The efficiency on real data for single muons is obtained by the ratio of reconstructed muons matched to the $L2Mu3$ (single muon trigger) over all the reconstructed muons with high quality cuts (see table 5.1). The cut $TrackerMuonArbitrated$ refers to the requirement of that track to be considered a tracker muon after resolving the ambiguity of sharing segments. A ‘tracker muon’ is an inner track that is matched to at least one segment reconstructed in the muon chambers. The $TMLastStationAngTight$ cut is also a tracker muon requirement that applies position and pull cuts to the segment match in the deepest required station[69].

5.2.3 Offline event selection

The *good event* qualification was assigned to events that passed the minimum-bias trigger requirement and also satisfied a set of offline cuts. The offline event selection was implemented to clean up triggers coming from cosmics, beam-halos, background, beam-gas events and ultra-peripheral collisions (UPC). The cuts are the following:

Table 5.1: Quality cuts applied to global muons for trigger efficiency. Variables described in Sec 5.2.4

cut	Value Applied
isTrackerMuon	*true*
isGlobalMuon	*true*
N. of valid hit in the inner track	≥ 11
N. of valid hit in the muon stations	≥ 1
χ^2_{global}/ndf	$\leq 10.$
χ^2_{inner}/ndf	$\leq 4.$
$d_{xy}(vertex)$	≤ 0.2 mm
$d_z(vertex)$	≤ 14 mm
pixel layers with measurement	≥ 1
$TrackerMuonArbitrated$	*true*
$TMLastStationAngTight$	*true*

- BSC halo-filter: Events in which any of the BSC halo triggers bits fired were excluded. The BSC halo trigger requires coincidence on both sides. This means that at least one hit on each side, in any segment within 40 ns (timed for a muon moving at the speed of light) would fire the trigger. This is intended to exclude muons consistent with having a trajectory that crosses the detector from one side to the other. Figure 5.7 shows the correlation between the number of hits in the first pixel layer and the total HF energy. The events from collisions (black) show a good correlation between the two quantities. The events triggering the BSC beam halo (red) bits have small energy deposits in the HF and large activity in the pixel layers [67].

- A two-track primary vertex requirement was imposed. In peripheral events, all tracks with a $p_T > 75$ MeV/c were used to reconstruct the vertex. In central events, the minimum p_T was increased to keep the maximum number of fitted tracks stable around 40-60, ensuring time-efficient reconstruction.

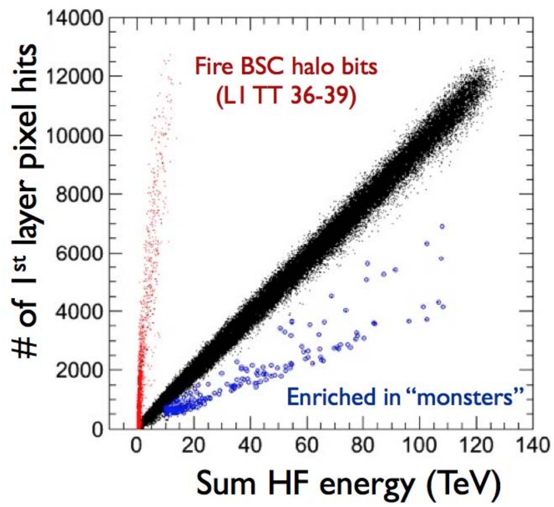

Figure 5.7: Correlation of between sum HF energy and 1st pixel layer activity for *good event* (black), BSC triggers (red) and 'monster' events (blue)

- To remove 'monster' events a requirement of pixel cluster-length compatibility with the vertex was implemented. Figure 5.7 shows (in blue) events in which HF deposit are much smaller than for any *PbPb* collisions. Those events are mostly eliminated by a cluster compatibility cut (defined below); some are eliminated by the BSC cut alone; but they are all eliminated by the combination of both. Figure 5.8 shows the cut implemented to exclude "monster" events, which fall below the red line are excluded. The compatibility variable is the number of clusters that have a length that is compatible with the reconstructed vertex, divided by the number of hits that are compatible with an artificially displaced vertex (offset ± 10 cm). If the ratio is high, that indicates a well defined vertex and a valid collision. If the ratio is close to unity, this indicates that the vertex is ill defined, characteristic of 'monster' events. At very low pixel multiplicity, the compatibility is allowed to be low, in order to keep events that have a little larger background hit fluctuation but otherwise good collisions. Figure 5.8 shows the relation between cluster-vertex compatibility and the number of pixel hits, used to define a 'good event'. The line shows the value of the cut being applied.

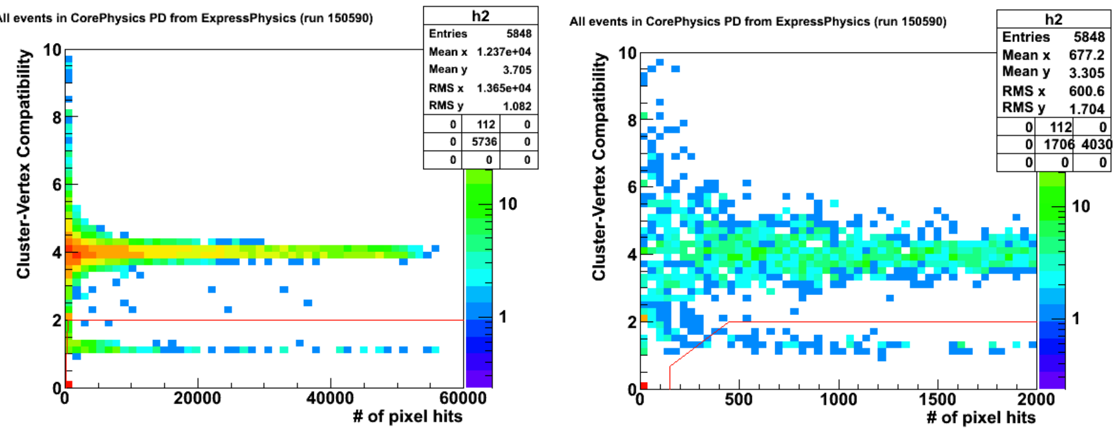

Figure 5.8: "Monster Event" cut, excludes events below the red line. Cluster-vertex compatibility(y-axis) against the number of pixel hits(x-axis).

- An offline requirement of HF coincidence requiring at least 3 towers on each side of the interaction point with at least 3 GeV of total deposited energy in the HF.

5.2.4 Signal Extraction

The main objective of the signal extraction is to keep as much of the Z $\rightarrow \mu^+\mu^-$ events while suppressing the background. In order to improve the signal-to-noise ratio it is important to know the parameters that can help remove some of the background without adversely affecting the signal. A series of quality cuts are applied to ensure that the information provided by reconstructed object is reliable. Some of the cuts have become standard within analyses that rely on muon reconstruction and/or use the Heavy-Ion tracking sequence. Given that the analysis relies on the proper identification of high-p_T muons, the main goal is to ensure that the Global muon objects pass the basic quality standards. By virtue of the CMS design, not a lot of punch-through hadrons make it to the outer muon chambers resulting on a fake muon, however the can make noise in the muon reconstruction. Cosmic muons can also 'fake' a collision muon. To ensure an un-biased selection of the cut parameters and their values, a cut analysis exercise was performed before taking a look at the data. Each of the quality cuts are summarized in the following section.

Quality cuts

In order to study the effects of each of the cuts the variables, five different distributions were plotted in Figs 5.9 to 5.14. In the same canvas were overlaid reconstructed muons from MC (Z $\rightarrow \mu^+\mu^-$ embedded in HYDJET events) with reconstructed muon from HI data. Each distribution is defined:

- Muons from Z^0: A set of reconstructed global muons that were traced back to a generated muon which decayed from a Z^0 (Gray histogram).
- Punch-throughs: A set of reconstructed global muons that where traced back to anything other than a muon after the GEANT simulation (Red-hashed histogram).
- Other Muons: A set of reconstructed global muons that where traced back to a muon but do not originate (at any level) from a Z^0(Blue hashed histogram).
- Muons from HIData: A set of reconstructed global muons from real collisions, after passing quality cuts (Green triangles).
- Muon from Zcand: A set of reconstructed global muons that come from the Z candidates from collisions (Red stars).

All the distributions have been normalized to match the integral area of the muons that come from Z candidates (red stars). In the embedding process, as detailed in section 4.1.1, the Z $\rightarrow \mu^+\mu^-$ events were generated flat in p_T and rapidity. In order to show a "*Realistic*" profile of each of the variables a re-weigthing procedure was applied in rapidity and transverse momenta. The flat distributions were weighted according to the shapes generated with PYTHIA. The dashed red vertical lines indicate the value of the quality cut used for that variable. In all cases the five distributions are plotted after all the quality cuts have been applied, except the one that is being profiled.

Some of the cuts implemented were selected taking into account the physical acceptance of the CMS detector. The pseudorapidity coverage of the muon chambers is $\pm$ 2.4 units, thus reconstructed muons beyond those limits were not considered. It can be observed that the muons coming from Z^0 (MC or HI data) follow a close-to-flat distribution

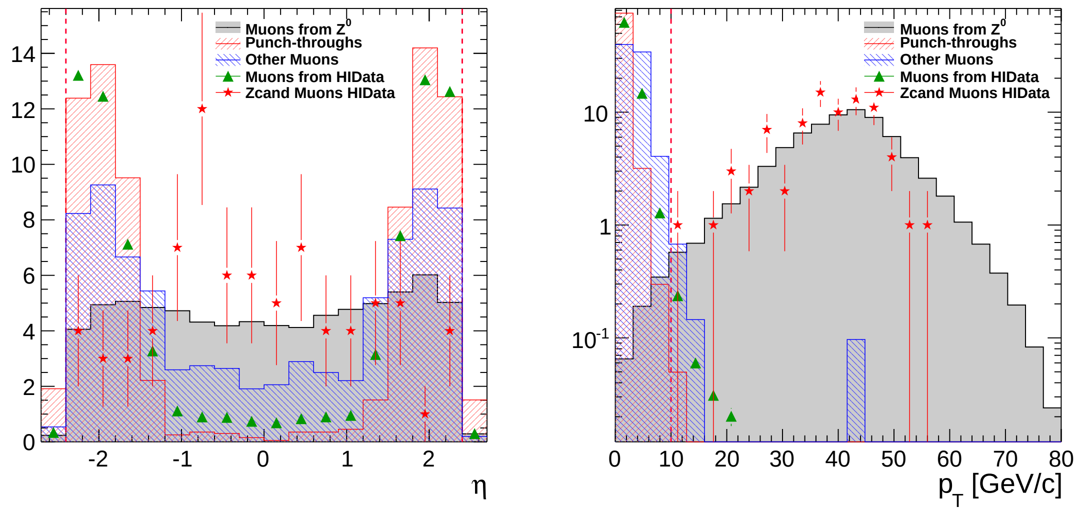

Figure 5.9: η and $p_T$distribution of reconstructed muons form HI data and MC (see text for description)

as a function of η, whereas muons from in-fligth decays or punch-through favor the forward direction. This is because the p_T requirement to be reconstructed in the barrel is higher than in the endcaps. Figure 5.9 (Left) shows the η distributions of the five sets. On the right panel the p_T distribution is shown. The cut at 10 GeV/c applied for the analysis has a negligible effect on the muons from simulated Z^0 decays (gray histogram) and does not cut any of the muons from the Z^0 candidates. It is worth noting the impact of this cut in eliminating reconstructed muons that do not com from Z^0 decays. This cut was set to reduce the systematic error at the expense of losing 1% of the generated Z^0 , due to fact that the turn-on curves of the triggers are safely under this value.

In order to better constrain muons originating from the collision, the distance between the reconstructed primary vertex and the closest point of the reconstructed trajectory is measured in the transverse plane (d_{xy}) and in the longitudinal plane (d_z). In Fig. 5.10 it can be seen that the cuts implemented are very loose and do not affect the signal while cutting a small portion of the background. One of the characteristics of muons from a Z^0 decay is that the p_T is considerably higher than the muons from the underlying event. These high-p_T muon tracks have an improved pointing accuracy to the interaction point.

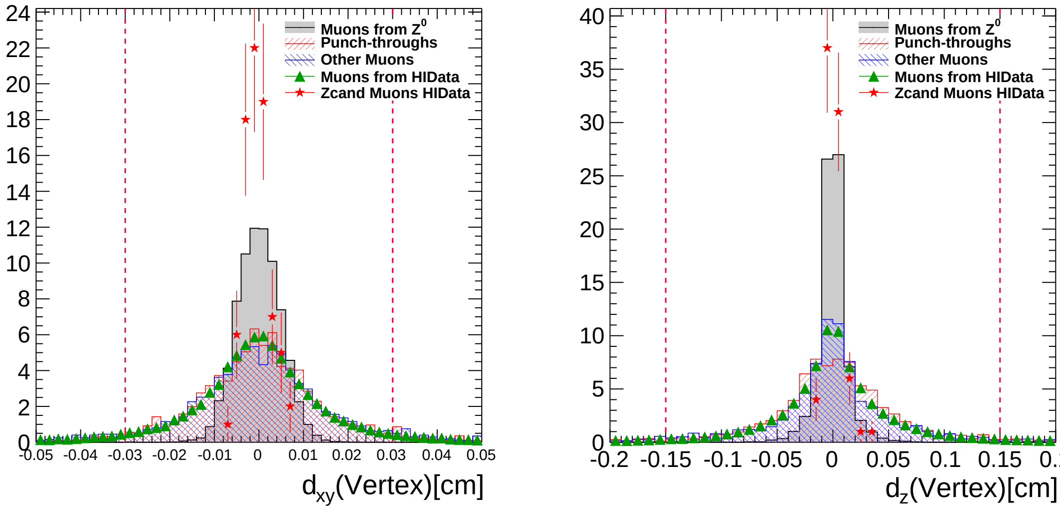

Figure 5.10: d_{xy} and d_z distribution of reconstructed from HI data muons and MC (see text for description)

In order to have a reliable reconstruction, a goodness of fit is calculated at different levels of the reconstruction and properly normalized by the number of degrees of freedom. The χ^2_{inner}/DoF is the normalized χ^2 distribution for the inner track that used to match to a muon detected by the muon chambers to form a global muon. The χ^2_{global}/DoF is the normalized χ^2 distribution for the overall fit of the global muon, it is a powerful tool to reject both decay-in-flight and punch-throughs [70]. In both cases the applied cuts are very loose, as seen in Fig 5.11.

The number of hits used has an impact on the quality of the reconstruction. Figure 5.12 shows the distribution of the number of hits used for the reconstruction of the inner tracker track (left) that forms the global muon (right) and the number of hits used in the over-all fit of the global muon. The number of hits in the tracker track part of the global muon is ≥ 10 hits. Generally, tracks with smaller number of hits give a bad p_T estimate. In-flight decays give rise to lower hit occupancy in these tracks, since the track does not originates at the innermost layers. For the global muon the requirement is set to more than 1 "valid" hit. With this requirement it is ensured that the global muon is not a bad match between the spatial and momentum information from the muon system and tracker. It is

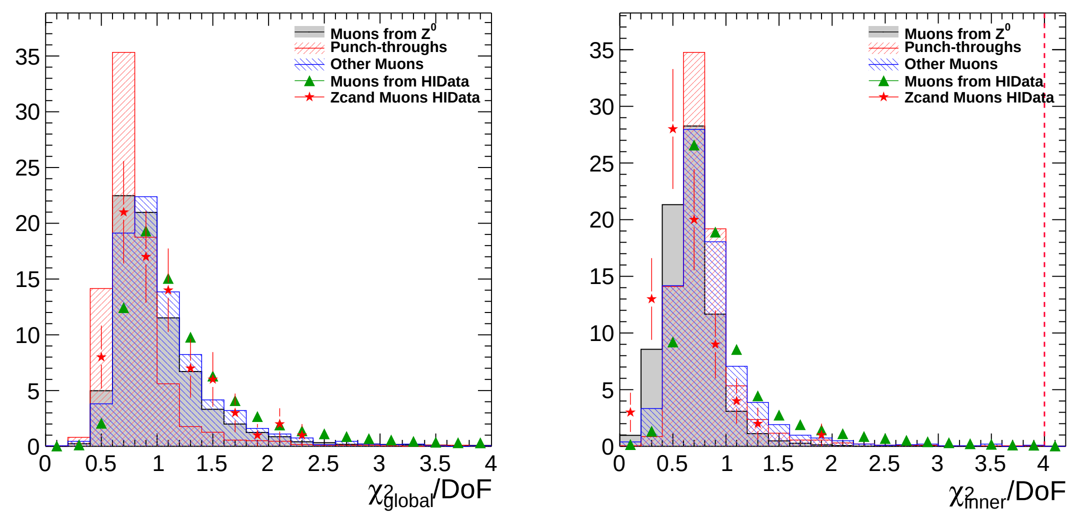

Figure 5.11: Inner χ^2 and global χ^2 distribution of reconstructed muons from HI data and MC (see text for description)

clearly visible that this is one of the more effective cuts to get rid of punch-throughs.

Figure 5.13 shows the distribution of the number of pixel hits coming from the inner track (left) and the number of segments matched to the outer part of the global muon track (right). The inner-most part of the tracker is an important handle in discarding non-prompt muons. By asking for a minimal number of pixel hits it can be ensured that the track originates at least within the pixel detector geometry. The number of matched segments from the muon chambers to the global muon track is also shown in Fig. 5.13 (right). The larger the number of segments matched to the track the more information from the local reconstruction (from each of the sub-detector is used) is used. This is an effective way to chose global fits using substantial amount of information from the chamber themselves.

Figure 5.14 shows the boolean variable $isTrackerMuon$ and the relative error of the reconstructed p_T. The $isTrackerMuon$ variable refers to the quality of the global muon to also fulfill the requirements to be considered a *tracker muon*. A 'tracker muon' is a well reconstructed inner-track that is matched to at least one segment reconstructed in the muon chambers. This is an effective cut against in-flight decays, punch-throughs and accidental matching (with noisy background tracks or segments). The panel on the left shows the

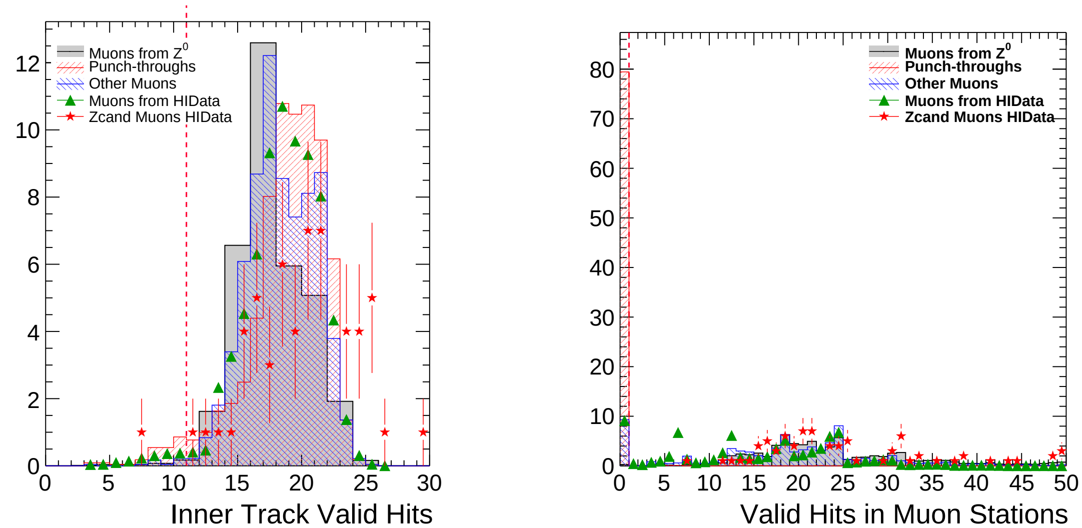

Figure 5.12: Inner track and global muon hits distribution of reconstructed muons from HI data and MC (see text for description)

relative error of the reconstructed p_T, for global muons, the p_T assignment is obtained from the inner track (up to 100 GeV/c). This cut simply removes those muon with a bad p_T assignment.

The quality cuts that were implemented on the global fit of the muons are in accordance to recommendation from the Muon object group [71, 70] and following the spirit of the cuts used in previous Z^0 measurements in pp collision with the CMS experiment [72] where applicable. An overall agreement between can be observed between the distribution of the muons coming from a Z^0 decay in MC and the muons coming from the Z^0 candidates in the Heavy-Ion data.

Table 5.2 summarizes the value of each of the cuts in the column. The second column shows the impact of each cut applied to the MC sample defined in Sec. 4.1.1 applied by itself. The percentage shown in the third column is the fraction of the sample kept when a specific cut is applied by itself. The fourth column shows the fraction of muons coming from a Z decay that is kept when all other cuts are applied and the parameter at hand is released. It can be seen that none of the cuts introduce inefficiencies greater than 1%. The overall efficiency after applying all the quality cuts is estimated to 97.58%.

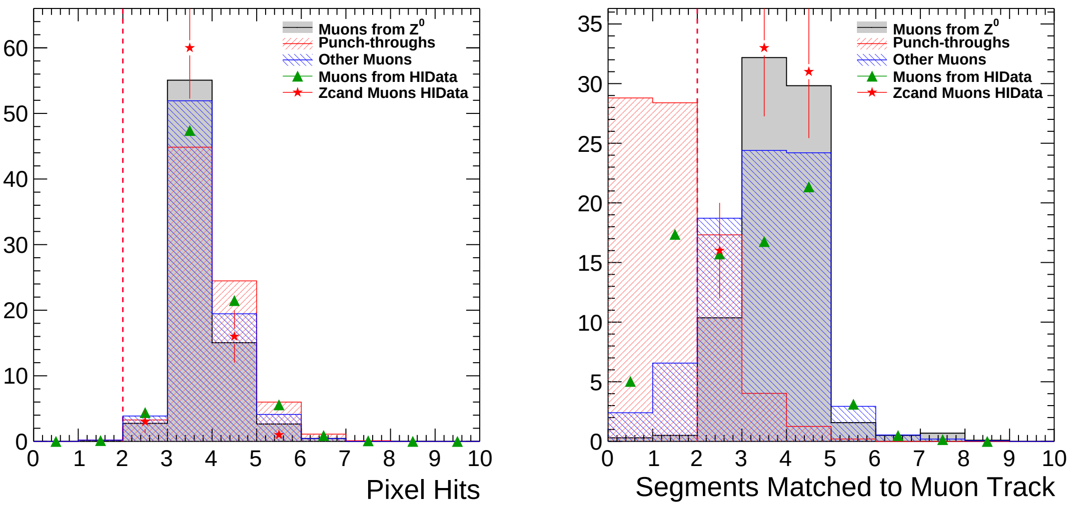

Figure 5.13: Pixel hits and matched muon segments distribution of reconstructed muons from HI data and MC (see text for description)

5.2.5 Z^0 Acceptance

Acceptance can be defined as the fraction of produced events which are measurable by the detector out of the total number of generated events within a given phase-space region. In this light, the acceptance is dependent on the phase space spanned by the generated Z^0's, which will eventually decay into muons, and also on the kinematics that the daughters will need in order to be *detectable*. A *Detectable* muon must have enough p_T to reach the muon chambers, and must leave a certain number of reconstructible hits in the sensitive areas of the muon chambers. Furthermore, the muons must be reconstructed with opposite-sign charges, and their kinematics must add up to an invariant mass from 60 to 120 GeV/c^2. The CMS detector has a coverage of $|\eta|$ <2.4 for muons. The p_T acceptance has an η dependence, but for the purposes of this analysis was set at a constant of 10 GeV/c, with full coverage as a function of ϕ. To generate the Z^0 decays, a PYTHIA [73] simulation is used at $\sqrt{s_{NN}}$ =2.76 GeV is used with CTEQ6L1 PDFs [?]. Figure 5.16 shows the acceptance for Z^0 bosons as a function of rapidity and transverse momentum. The acceptance as a function of p_T exhibits a constant value on the order of 77.7 $\pm$ 2% in the range of 0 to 50 GeV/c [1]. The acceptance as a function of p_T has a maximum in the mid-rapidity region

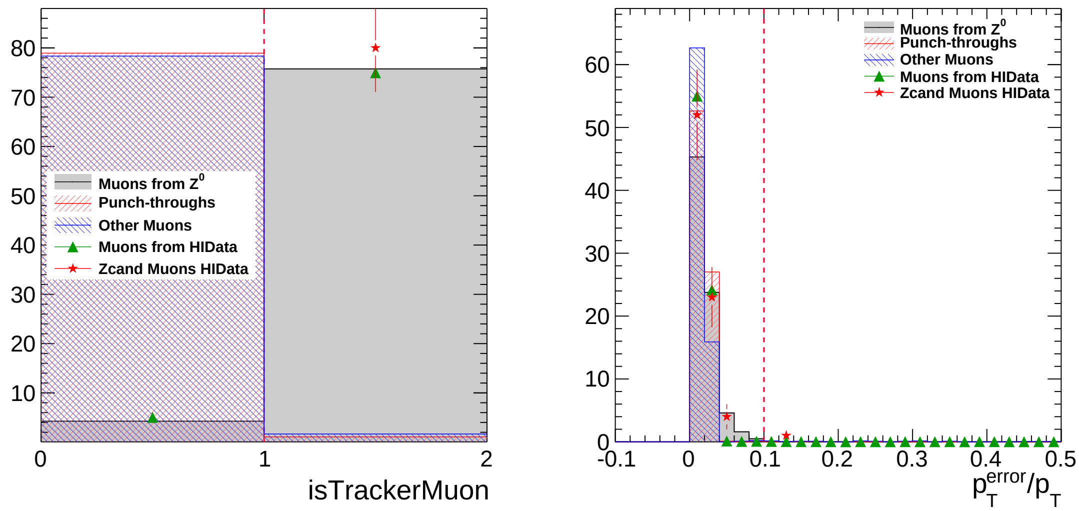

Figure 5.14: Tracker Muon requirement and $p_T$error/$p_T$distribution of reconstructed muons from HI data and MC (see text for description)

while it decreases in the forward region. This implies that 77.7 $\pm$ 2% of the Z^0 decays produced by our generator are indeed reconstructible with the CMS detector.

5.2.6 Z^0 Acceptance $\times$ Efficiency

For the purpose of this analysis it is more useful to calculate acceptance and efficiency combined. The product of these two represents the fraction of Z events that are successfully reconstructed with respect to the number that were produced. One of the advantages of having acceptance and efficiency combined, is that there is no risk of double correcting for a missing event or completely ignoring some events that may fall between the definitions of acceptance and efficiency. For the calculation of *Acceptance* $\times$ *Efficiency* the PYTHIA gun sample embedded in minimum-bias real events described in section 4.1.4 was used. In this sample the Z^0 is generated with a flat distribution in rapidity and transverse momentum. Due to this, the corrections based on *Acceptance* $\times$ *Efficiency* will need to be readjusted using weights to account for the realistic distribution in Z^0 rapidity and $p_T$distributions. The shapes used for the weights is obtained from PYTHIA. This weighting procedure is also used to correct for the use of a minimum-bias event sample for

Table 5.2: Quality cuts applied to global muons

	Value Applied	Only this cut	All except this cut
$\|\eta\|$	< 2.4		
p_T	≥ 10 GeV/c	99.00%	98.47%
χ^2_{inner}/ndf	$\leq 4.$	99.98%	97.58%
χ^2_{global}/ndf	$\leq 10.$	99.69%	97.82%
$d_{xy}(vertex)$	≤ 0.3 mm	99.93%	97.59%
$d_z(vertex)$	≤ 1.5 mm	99.94%	97.59%
$Validhits_{innertrack}$	≥ 11	99.62%	97.90%
$Validhits_{muonstations}$	≥ 1	99.72%	97.83%
isTrackerMuon	*true*	99.54%	97.94%
p_T^{error}/p^T	≤ 0.1	99.77%	97.70%
All cuts applied	97.58%		

the generated Z $\rightarrow \mu^+\mu^-$ events, instead of one that reflect hard collisions as shown in 5.4.

In order to calculate the *Acceptance* $\times$ *Efficiency* the (MABH) tool (described in Sec. 4.3.1) was used. This allows us to trace back (to the generator level) each of the single muons that make up the dimuon candidate in the mass range 60 - 120 GeV/c^2. The following definitions were used:

- Dimuons that are in our acceptance (defined in Sec 5.2.5) and were successfully reconstructed in the mass range 60 - 120 GeV/c^2 as defined by having two opposite charged global muons with $p_T \geq$ 10 GeV/c and $|\eta| \leq 2.4$ and each of the muons passing the quality cuts. In order to match a reconstructed muon with a simulated muon the criteria used was 75% hit sharing. This defined in Sec 4.3.1.

- For the efficiency ,the normalization factor (denominator) is a dimuon pair in the mass range 60 - 120 GeV/c^2 and $|y| \leq 2.4$.

The corrections obtained from the *Acceptance* $\times$ *Efficiency* method were applied

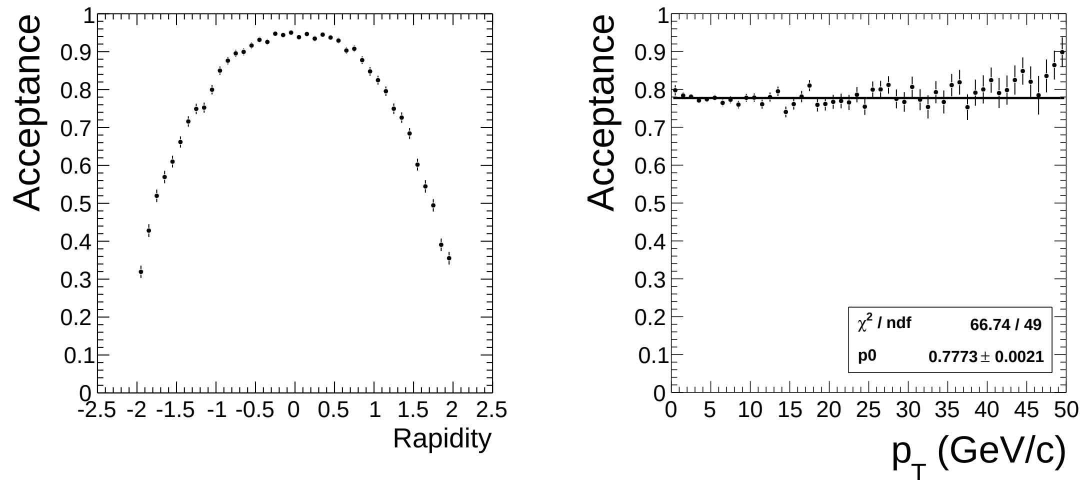

Figure 5.15: Z $\rightarrow \mu^+\mu^-$ acceptance for each of the muons in $|\eta|$ <2.4 and p_T>10 GeV/c as a function of Z^0 rapidity and transverse momentum [1]

in a bin-by-bin basis as a function of dimuon rapidity and event centrality with the proper weights to account for the realitic distributions as described in Eq. 5.1. The middle panel of Fig. 5.16 show a flat distribution of *Acceptance* $\times$ *Efficiency* as a function of Z^0 p_T, hence the p_T dependence is factored out of Eq 5.1

$$\alpha \times \varepsilon_{avg} = \frac{\sum_{y\ bins} \sum_{cent\ bins} \alpha \times \varepsilon(y, cent) \times \omega_{pythia}(y) \times N_{coll}(cent)}{\sum_{y\ bins} \sum_{cent\ bins} \omega_{pythia}(y) \times N_{coll}(cent)} \tag{5.1}$$

In figure 5.16 a result obtained from "peak method" is also shown as a cross check. This is the method used in Ref. [1]. It can bee seen that a good agreement is reached between these two approaches.

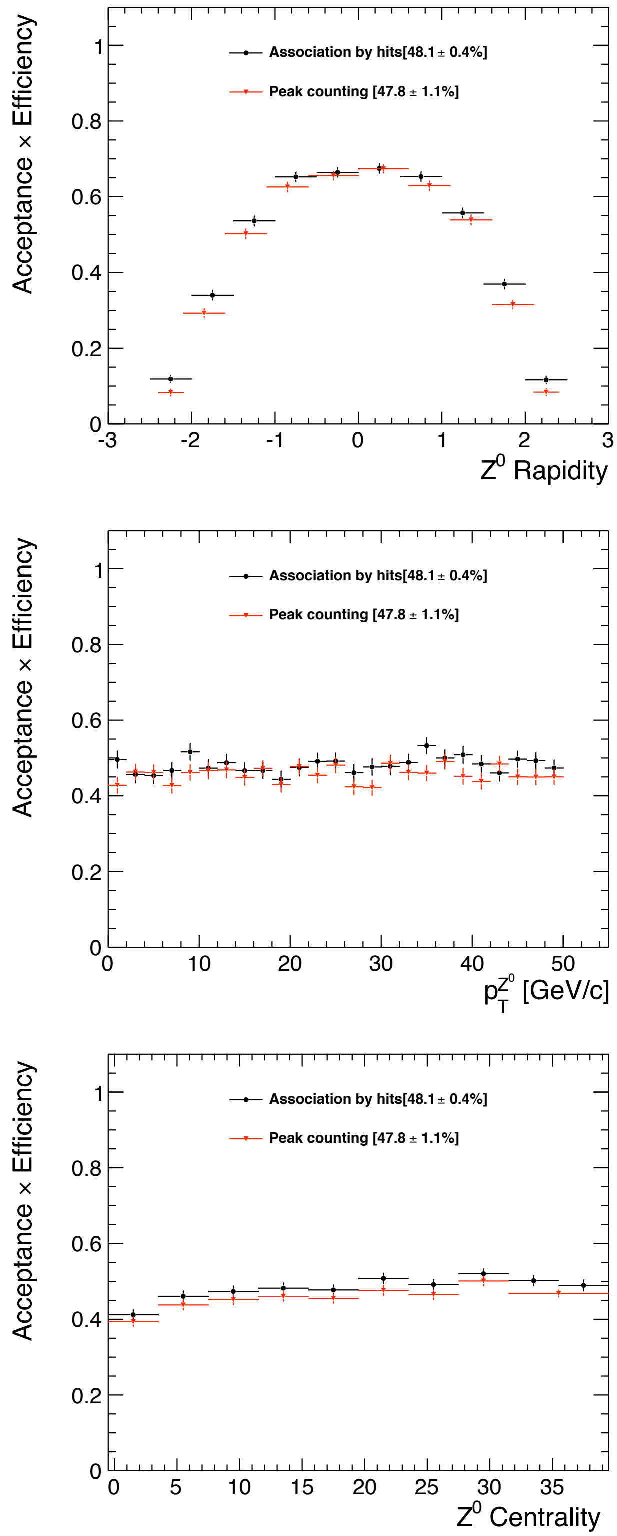

Figure 5.16: Acceptance × efficiency as a function of rapidity, transverse momentum and centrality

Chapter 6

Results and Discussion

In this chapter the Z $\rightarrow \mu^+\mu^-$ measurement is presented as a function of rapidity, transverse momentum, and number of participants. The nuclear modification factor with respect to pp collisions at $\sqrt{s}$=2.76 TeV is also presented.

6.1 $PbPb$ analysis sample

The first Z $\rightarrow \mu^+\mu^-$ event in $PbPb$ collisions recorded by CMS came in run 150590 on Nov. 9th, shown in figure 6.1. The event display shows the activity in the inner tracker represented by the yellow tracks that populate the innermost region of the detector. The high multiplicity expected from Heavy-Ion collisions is clearly visible here. The towers in the electromagnetic calorimeter are shown in red, while the towers in blue are found in the hadron calorimeter. It can be noticed that most of the activity in the ECAL and HCAL is in the forward region. The purple towers are found in the Hadronic forward calorimeters, used to trigger minimum-bias collisions and to calculate the event centrality. The two reconstructed global muons are shown as black tracks. The first muon [η = 0.38, ϕ = -1.98, p_T = 33.80 GeV/c] is reconstructed in the barrel region and the DT chambers, with segments belonging to the track shown in gray. The second muon [η = -2.28, ϕ = 0.71, p_T = 29.41 GeV/c] is in the forward region with the CSC chambers also in gray. The outline of the detector can be seen in the background in a faint red and blue tone.

With an integrated luminosity of $\mathcal{L}$ = 7.2 μb^{-1}, a total of 39 dimuon pairs were

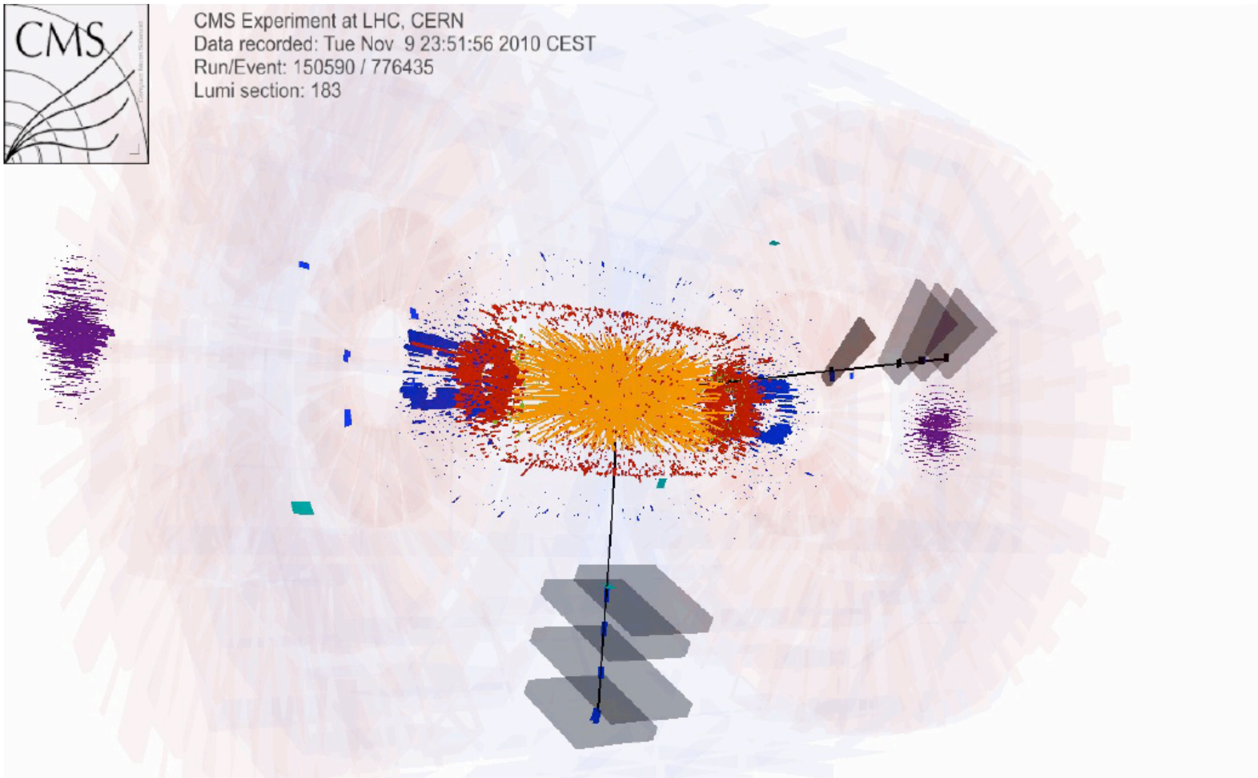

Figure 6.1: First Z $\rightarrow \mu^+\mu^-$ candidate event in PbPb collisions in the CMS detector

found, after applying the quality cuts outlined in table 5.2 and requiring two muons with opposite charge, in the mass range 60-120 GeV/c^2. Figure 6.2 shows the invariant mass of the Z^0 candidate pairs (blue squares), as well as the only same-sign pair (red open circle) that passed the quality cuts in the range 30-120 GeV/c^2. It is easy to see the clear signal the emerges almost background-free. In the range 30-50 GeV/c^2 a structure forms due to the continuum from other physics processes, mainly $b\bar{b}$ production. In the figure, a black histogram from the Z $\rightarrow \mu^+\mu^-$ measurement in pp collisions at $\sqrt{s} = 7$ TeV by CMS [74] is shown. This pp measurement was performed with similar kinematic cuts. The pp invariant mass histogram has been scaled to match the integral obtained with the $PbPb$ data. It can be seen that the performance of the detector is comparable between $PbPb$ and pp collisions.

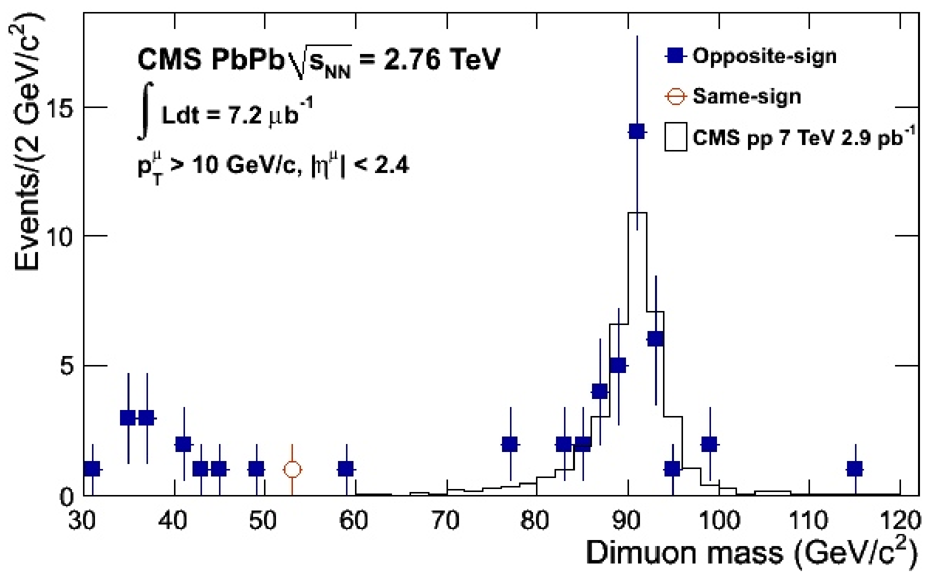

Figure 6.2: Invariant mass distribution of Z^0 candidates in PbPb collisions at $\sqrt{s_{NN}} = 2.76$ TeV

6.1.1 Mass fits

Due to the size of the data sample and lack of background (in the 60 -120 GeV/c^2 mass range), this analysis can be carried out by counting the events that make up the invariant mass peak. Yet, it is also interesting to compare these events to relevant fits. Figure 6.3 shows the Z^0 -candidate muon pairs in blue markers overlaid with different fits. The solid green line is a fit to the data using a Breit-Wigner (BW) [75] functional form given by:

$$f(E) \propto \frac{k}{(E^2 - M_z^2)^2 + M_z^2\Gamma^2} \tag{6.1}$$

where the width of the distribution is given Γ fixed to the Particle Data Group (PDG) value 2.49 GeV/c^2 and is related to the mean lifetime as $\tau = 1/\Gamma$ (in natural units). The amplitude is given by the parameter k, which is allowed to vary when fitting. The parameter M_z is the pole of the distribution which represents the value of the Z^0 mass. The Breit-Wigner is the natural fit for resonances in particle physics without taking into account resolution effects. The BW exhibits a tail in the low end of the distribution due to radiative losses. A better

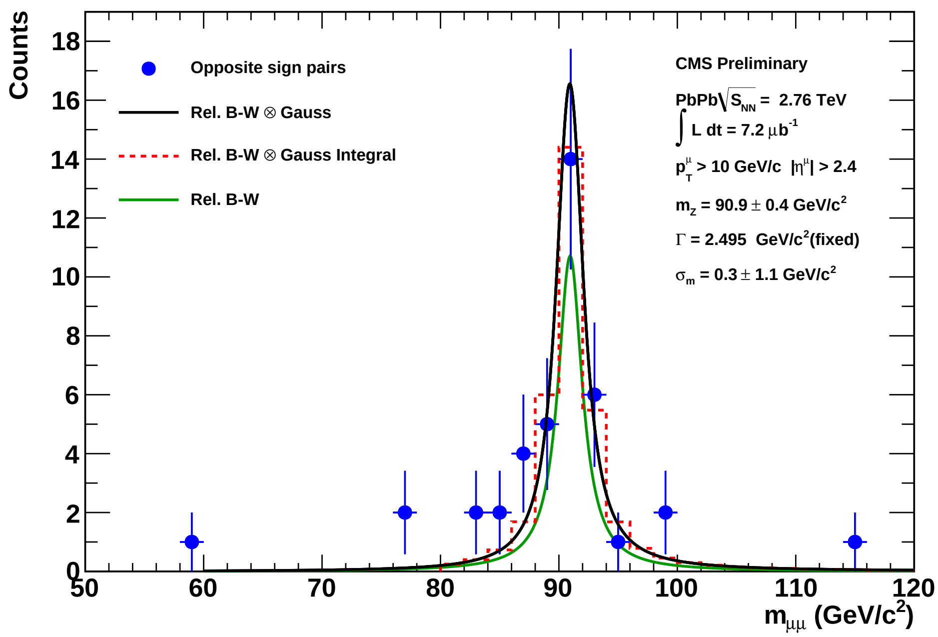

Figure 6.3: Invariant mass Z^0 candidates in $PbPb$ collisions at $\sqrt{s_{NN}} = 2.76$ TeV with fits, fit parameters listed for the BW convolved with a Gaussian

approach to fit the reconstructed data is to account form smearing of the distribution due to resolution effects. This can be accomplished by using a Breit-Wigner convolved with a Gaussian shape. An extra parameter is added with respect to the pure BW, σ_z, which is the width of the gaussian shape. This is shown in figure. 6.3 with the solid black line fit. The dashed red line shows the bin integral version of the BW$\otimes$Gaussian shape. It can be seen that the the BW$\otimes$Gaussian follows the data closer than the BW alone. The integral under the curve for the pure BW is $\sim$20 counts, while the convolved BW$\otimes$Gaussian yields $\sim$34 counts, compared to the 39 muon pairs that are plotted.

The parameters obtained from the fits are summarized in table 6.1. In both fits the BW width was fixed to the PDG value, and the rest of the parameters were obtained from the fitting routine.

Table 6.1: Fit parameters for Z invariant mass

Fit	Parameter	Symbol	Value
Relativistic Breit-Wigner			
	Width	Γ	2.495 GeV/c^2 (fixed PDG)
	Mean	M_z	90.07 $\pm$0.43 GeV/c^2
	Integral		20
BW $\otimes$ Gauss			
	Natural Width	Γ	2.495 GeV/c^2 (fixed PDG)
	Gaussian Width	σ_z	0.3 $\pm$1.1 GeV/c^2
	Mean	M_z	90.93 $\pm$ 0.37 GeV/c^2
	Integral		34

6.2 Systematic Uncertainties

Minimum bias counting

The efficiency of the minimum-bias bias trigger used was found to be 97 $\pm$ 3%. This comes from the fact that not all the inelastic collisions lead to a triggered event. The uncertainty was evaluated varying the Glauber parameters in Ref. [61].

Background fitting

The statistical uncertainty that arises from the limited sample can be affected by contribution to the background in the 60 - 120 GeV/c^2. The main sources of backgrounds around the Z^0 pole can can originate from W backgrounds, $Z \rightarrow \tau^+\tau-$, dibosons, $t\bar{t}$ and QCD multijet (with a muon inside) [74]. The contributions from all these sources add up to 3.7 parts per million. Electroweak backgrounds are not expected to be modified in the QGP. QCD backgrounds, however, should be modified by the QGP which can make the hadrons (that later decay into muons) loose energy as it traverses the medium. The main source of background that contribute to the opposite-sign dimuon distribution come from

$b\bar{b}$. Also, the semi-leptonic decay form D and $\bar{D}$ or B and $\bar{B}$ decays that combine into an opposite charged muon pair. The background $b\bar{b}$ is estimated to be a factor of 20 lower than the signal, even without assuming b-quark quenching [76]. To properly estimate the background that lies under the Z^0 mass peak an exponential is fit to the data obtained in the range 35-60 GeV/c^2. The integral of the exponential in that range is 1.48 counts while there are 39 counts in the same region. The ratio of, background over signal, yields a 3.8% to be used as a one sided systematic uncertainty.

Quality Cuts

In table 5.2 the sources of efficiency lost are listed. The total efficiency after all the quality cuts have been applied is 97.6% which can be translated to the loss of a 1 Z^0 candidate. The systematic uncertainty introduced by the use of quality cuts is estimated to be 2.6%.

Acceptance

The fraction of events that fall within the defined acceptance depends on the choice of kinematic parameters used to generate the samples, as well as the number of contributing diagrams for such processes. Acceptance uncertainties derive from the choice of the kinematic distributions under two assumptions:

- choice of the Parton Distribution Function (PDF),
- difference between LO and NLO MC generators.

Systematic uncertainties were obtained by comparing distributions obtained using PYTHIA interfaced with two different PDFs, namely CTEQ6L1 and MRST2004LO with results from MC@NLO interfaced with CTEQ6L1 [77]. By comparing the sample generated with PYTHIA-CTEQ6L1 with the one generated with PYTHIA-MRST2004LO, the systematics with respect to the PDF choice are extracted. The comparison of PYTHIA-CTEQ6L1 with MC@NLO-CTEQ6L1 is used to obtain the systematic uncertainties related to the leading order calculation used by the generator. Figure 6.4 (left) shows the acceptance of the Z^0 boson as a function of p_T. The acceptance is defined by:

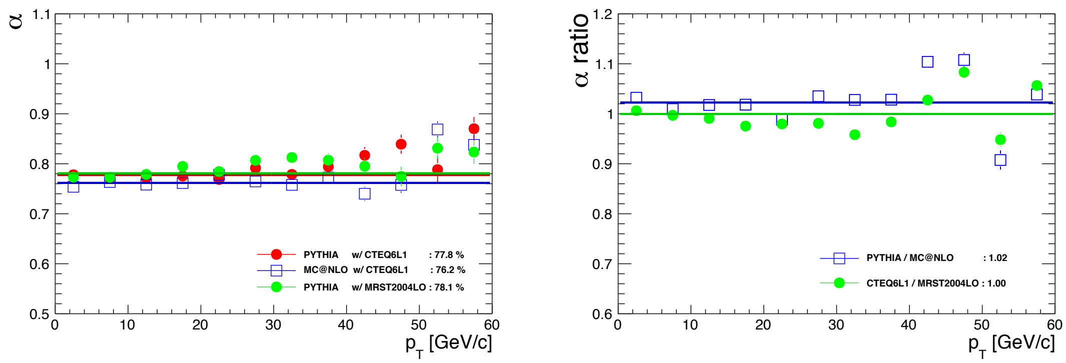

Figure 6.4: Left: Z^0 acceptance α versus p_T of the Z^0 , from: PYTHIA-CTEQ6L1 (red circles), PYTHIA-MRST2004LO (green full squares) and MC@NLO-CTEQ6L1(open blue squares). Right: Acceptance ratios, for generator choice (blue open squares), and for PDF choice (green full squares).

$$\alpha = \frac{N_z^{|y|<2.0;p_T^{\mu}>10GeV/c;|\eta^{\mu}|<2.4;M_Z[60-120GeV/c^2]}}{N_z^{|y|<2.0;M_Z[60-120GeV/c^2]}} \tag{6.2}$$

where the numerator is the number of Z^0's, within four units of rapidity, that decay into muons that have the chance of being reconstructed within a mass of 60-120 GeV/c^2. The denominator is the number of Z^0's generated in $|y|$ <2.0 in the same mass range. It can be observed that the acceptance is constant with the three generator-PDF configurations up to a p_T of 35 GeV/c. In all three cases the acceptance can be approximated with a constant value of ~77%. Figure 6.4 (right) shows the ratios of the distributions on the left. The ratio depicting the effect of using PYTHIA vs MC@NLO (blue line). The ratio between two different PDFs, CTEQ6L1 and MRST2004LOis also shown (green line). The difference between these two is less than ~2%.

In order to be able to extrapolate our result ($|y^Z| \leq 2.0$ and $p_T^{\mu} \geq 10GeV/c; |\eta^{\mu}| \geq 2.4$) and expand it to the entire phase space in which the Z can be generated, α_{Total}, a total acceptance is calculated. The ratio α_{Total} is defined by Eq. 6.3

$$\alpha_{Total} = \frac{N_z^{|y|<2.0;M_Z[60-120GeV/c^2]}}{N_z^{M_Z[60-120GeV/c^2]}} \tag{6.3}$$

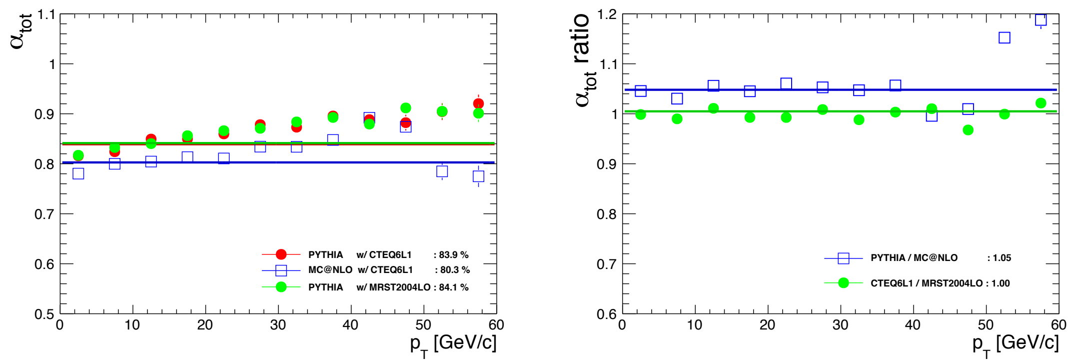

Figure 6.5: Left: Z^0 extrapolation to all rapidity α_{tot} versus p_T of the Z^0 , from: PYTHIA-CTEQ6L1(red circles), PYTHIA-MRST2004LO(green full squares) and MC@NLO-CTEQ6L1(open blue square). Right: Acceptance ratios, for generator choice (blue open squares), and for PDF choice (green full squares).

Figure 6.5 shows the acceptance of all the Z's in the 60-120 GeV/c^2 mass range that can be found in the $|y^Z| \leq 2.0$ phase space. The acceptance as a function of p_T shown in the left panel, it shows a slight increase with transverse momentum. The averaged value shown with a constant fit is simple used as visual reference. Both PYTHIA configurations interfaced with different PDFs show similar behavior, however, the MC@NLO interfaced with CTEQ6L1 shows a smaller acceptance value. The panel on the right is the ratio of the curve shown on the left. The effect of interchanging the generator is larger than the effect due to PDF selection, estimated at 5%.

Table 6.2: Variations of the acceptance corrections due to generator-PDF choice

Generator	α	α_{tot}
PYTHIAw/ CTEQ6L1	77.8%	83.9%
MC@NLOw/ CTEQ6L1	76.2%	80.3%
PYTHIAw/ MRST2004LO	78.1%	84.1%

The summary of the acceptance factors, used to estimate the uncertainties can be found in Table 6.2. The largest systematic uncertainty, due to the generator-PDF choice is calculated to be 1.9% for the analysis acceptance. The systematic uncertainties due to the choice of different generator parameters (LO vs NLO and PDF choice) can also influence the shape of the *Acceptance* × *Efficiency* corrections. The overall corrections when comparing the different generator-PDF setups, the average of the difference between setups, are calculated to be less than 1% [76].

Isospin

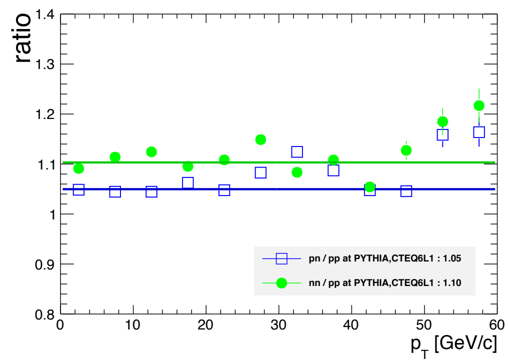

Figure 6.6: Ratios of the acceptance for pn/pp and nn/pp collsions, illustrating the systematic impact of isospin effects on the Z^0 acceptance.

Table 6.3: Variations of the acceptance corrections due to isospin effects.

Generator	α	α_{tot}
PYTHIAw/ CTEQ6L1p+p	77.8%	83.9%
PYTHIAw/ CTEQ6L1p+n	77.7%	83.8%
PYTHIAw/ CTEQ6L1n+n	77.4%	83.4%

Another acceptance effect that has to be taken into account is the one due to isospin. This arises from the comparison of proton-proton collision systems, to those involving proton-neutron or neutron-neutron, which are allowed by the collision of a Pb nucleus.

This is shown in Fig. 6.6. To study the impact of the isospin effect ratios of the acceptance as a function of p_T generated with PYTHIA-CTEQ6L1 are shown. The distribution in full circles shows the ratio of events generated in proton-proton/proton-neutron (pp/nn) collisions. The distribution in empty squares shows the pn/pp ratio. In both cases the ratios are close to unity. The deviaitons from unity are quantified in Table 6.3.

The summary of the acceptance factors due to isospin effects can be found in Table 6.3. The largest systematic uncertainty (from the difference between pp and nn collisions system) is calculated to be 0.4%.

Shadowing and Initial-state Energy Loss

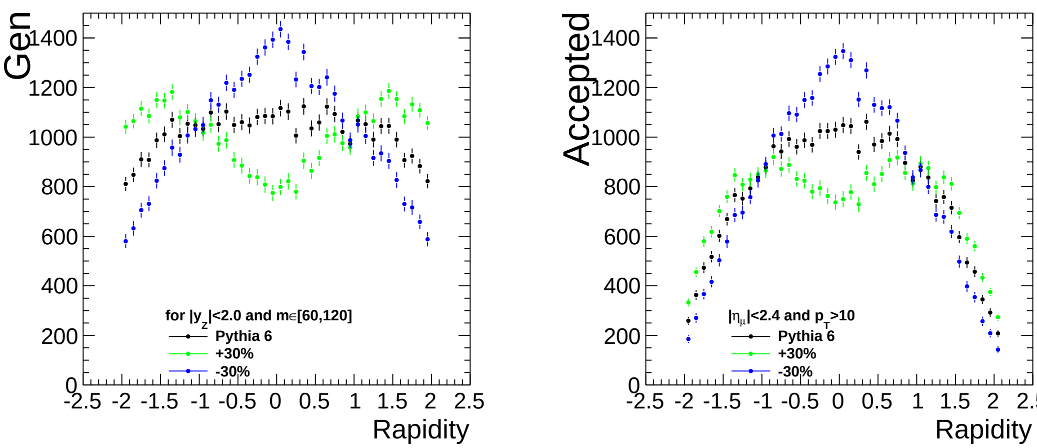

Figure 6.7: (Left panel) PYTHIA generated rapidity distribution (black), a +30% variation (green) and a -30% variation (blue) of the original shape. (Right panel) The rapidity distribution for the Z^0 that fall in the acceptance, for the same curves on the left

According to theory predictions in Refs. [47, 46] shadowing and initial-state energy loss should modify the rapidity shape for the Z. Because of this, the acceptance is also modified. The energy loss effect introduces a 3% modification of the cross-section, while shadowing is expected to have a 10-20 % impact. In order to properly account for the modifications at the acceptance level, variations for the p_T and rapidity shape were introduced. The rapidity of the Z^0 boson was obtained by artificially varying the shape by $\pm 30\%$ in

$|y^Z| \leq 2.0$ and the p_T^Z [0,50]GeV/c^2 range. The artificial variation parameters were chose to translate into a maximal (or minimal) acceptance factor. The 30% variation is expected to encase the maximum expectations from theory predictions. To include isospin effects in these variations, the three collisional systems will be considered (pp, nn, pn). The effects will be propagated for each of the collisional configurations. Fig. 6.7 shows an example of the 30% variations done to the rapidity shape. On the left panel that generated shapes, the PYTHIA shape (black), the +30% (green) and the -30% (blue). On the right panel the distribution as a function of rapidity of the accepted Z^0's for the three generated shapes.

In order to properly incorporate the isospin corrections it is necessary to estimate an average acceptance that reflects the fraction of pp:pn:nn collisions such as:

$$\alpha_{Isospin} = \frac{82^2 \cdot \alpha_{pp} + 82 \cdot 126 \cdot \alpha_{pn} + 126 \cdot 82\alpha_{np} + 126^2 \cdot \alpha_{nn}}{82^2 + 2 \cdot 82 \cdot 126 + 126^2} \tag{6.4}$$

The acceptance is calculated in each bin of interest. The acceptance and its variations for the *pp* case are shown in Table 6.4. The averaged effect is calculated to be 3%.

Table 6.4: Acceptance and variation to account for shadowing and energy loss.

y	system	α default	up	down
$[-2;2]$	pp	77.8 ± 0.6	80.6 ± 0.6	75.0 ± 0.6
$[-2;2]$	pn	77.7 ± 0.6	80.5 ± 0.6	74.8 ± 0.6
$[-2;2]$	nn	77.4 ± 0.6	80.2 ± 0.6	74.5 ± 0.6
p_T	system	α default	up	down
$[0;50]$	pp	77.6 ± 0.6	78.1 ± 0.5	78.2 ± 0.7
$[0;50]$	pn	77.5 ± 0.6	77.9 ± 0.5	78.0 ± 0.7
$[0;50]$	nn	77.2 ± 0.6	77.6 ± 0.5	77.8 ± 0.7

Trigger

The systematic uncertainties due to trigger efficiencies are calculated using the *tag-and-probe* method over real data. In section 5.2.2 the *L2DoubleMu3* efficiency is estimated to be $0.968^{+0.017}_{-0.027}$. For simplicity the uncertainties are symmetrized to a value of $\sim$ 2.2%. This value is calculated as a single muon efficiency, for a muon pair the uncertainty should be doubled to 4.5%.

Reconstruction

The systematic uncertainties due to the muon reconstruction are taken from the *pp* analysis obtained from data driven methods. The occupancy in the muon chambers is comparable to the one in *pp* collisions and is known at the 0.5% level[76]. Because of this, we can use a similar uncertainty on the reconstruction, taken to be 1% for dimuons.

The tracking and matching part of the reconstruction efficiency is obtained from the *tag-and-probe* method in Heavy-Ion data using the following approach, exemplified in Fig. 4.10:

- Tag : A global muon, matched to a muon with a p_T cut of 10 GeV/c and matched to the $L2SingleMu20$ trigger object.
- Probe: A stand-alone muon.
- Passing probe: A probe that is matched to global muon.

The single muon tracking efficiency is shown in Fig 6.8 as a function muon p_T and η. This efficiencies are calculated in MC Heavy-Ion events (Red) and HI data (Blue) with a Z $\rightarrow \mu^+\mu^-$ embedded event. The efficiency is also calculated in HI data (Black). The efficiency from data is $87.5^{+3.8}_{-4.7}$%. To calculate the systematic uncertainties the efficiency from the *tag-and-probe* method will be used as it as the advantage of being data-driven. The total systematic uncertainty from the tracking reconstruction is estimated to [+8.7,-10.7]%.

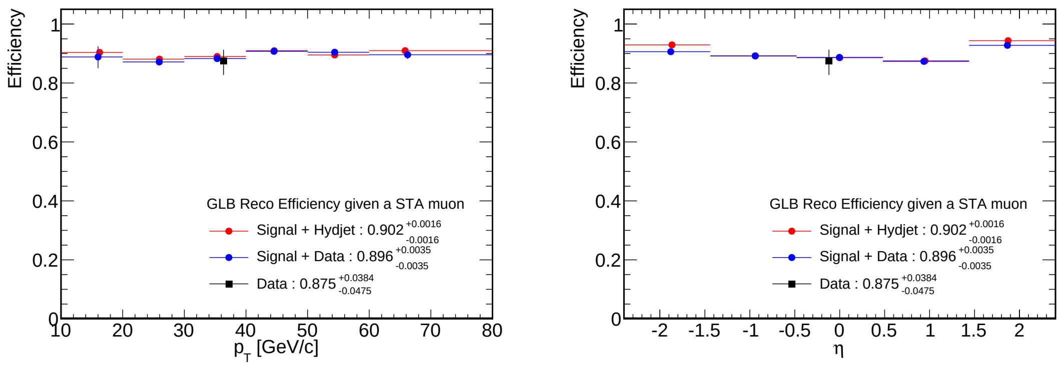

Figure 6.8: Single muon matching and tracking efficiency as a function of p_T (left) and η (right).

Other effects

Smaller corrections due to the differences between the embedded sample in real data and HYDJET, are calculated to be on the order of 1% [76]. Momentum-scale and resolution corrections are dependent on the detector alignment and on the material present in it. These did not change with respect to the setup for the *pp* run, hence the systematic uncertainty is taken as 0.2% as in Ref. [74].

All systematic uncertainties are summarized in table 6.5. After they are added in quadrature it yields an asymmetric +11.1% - 13.3% uncertainty band due to systematics. The largest component being from the inner tracking reconstruction efficiency estimation. The total systematic uncertainty is still smaller than the statistical uncertainty of $(1/\sqrt{39})$ or 16%.

6.3 *PbPb* Results

Table .9 shows some of the reconstructed variables of each of the 39 Z candidates along with information of the muon daughters. Form this table the distributions as a function of rapidity, transverse momentum and N_{part} can be extracted.

Table 6.5: Systematic uncertainties

	uncertainty
Background fitting	- 3.8%
Quality cuts	± 2.6%
Acceptance	± 1.0%
Isospin	± 0.4%
Acceptance(Energy loss and shadowing)	± 3%
Trigger	± 4.5%
Muon reco	± 1%
Tracking reco	± +8.7%, -10.7%
MC simulation	± 1 %
Scale & Allignment	± 0.2%
Minbias counting	± 3%
Total	+11.1% -13.3%

6.3.1 Z^0 Rapidity

The Z $\rightarrow \mu^+\mu^-$ differential yield as a function of rapidity is obtained in a rapidity window of Δy=4.0 using equation 6.5.

$$\frac{dN}{dy}(|y| \leq 2.0) = \frac{N_Z}{\alpha\epsilon N_{MB}\Delta y} \tag{6.5}$$

Using a total of 55 $\times$ 10^6 minimum bias events, with 39 candidates, dN/dy is found to be (33.8 $\pm$ 5.5 $\pm$ 4.4) $\times$ 10^{-8}. Figure 6.9 shows the rapidity distribution of the Z candidates. The data is shown in red dots in three rapidity bins $|y| \leq$0.5, 0.5 $\leq |y| \leq$1.0 and 1.0$\leq$ $|y| \leq$ 2.0. Sytematic uncertainties are shown in orange boxes and statistical uncertainties are shown as black bars. The theory models include a distribution from POWHEG interfaced with PYTHIAscaled by A^2/σ_{PbPb} (black line). The theoretical models discussed in the following lines were provided as *pp* equivalent cross-sections and multiplied by A^2/σ_{PbPb}. The comparison of the distribution by Salgado and Paukkunen using the unmodified CT10 parameterization(green dotted line) [46] with the data shows the difference that arises from isospin effects. The previous model is shown with an EPS09 [78] modified nuclear parton density function (blue line, with systematic uncertainties as blue bands). This model takes into account shadowing effects. A model by Neufeld and Vitev using the MSTW08 parton distribution function [48], which also includes isospin effects (dotted brown line). The previous model with energy loss effects is also shown (red-dashed line). Form figure 6.9 it can be seen that the data points agree with a nuclear scaling (A^2/σ_{PbPb}). The data agrees with the *pp* models after taking into consideration the nuclear scaling. This is an indication of no modification induced by the hot medium. The experimental uncertainties do not allow to discern from the other, smaller, effects.

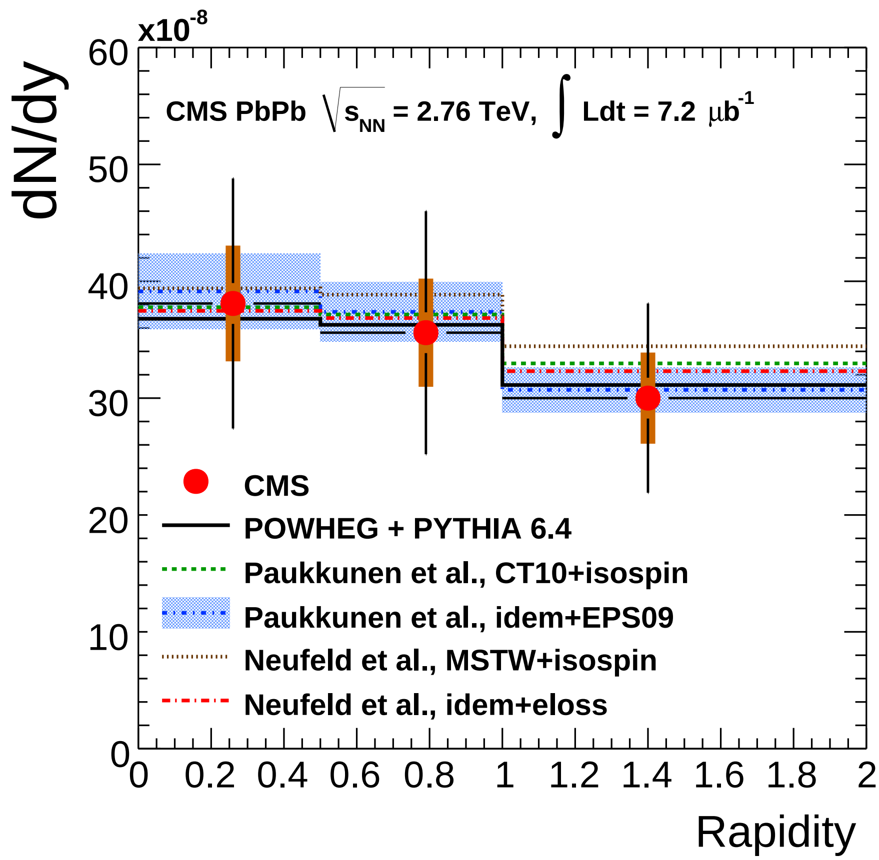

Figure 6.9: Rapidity distribution of Z candidates in *PbPb* collisions at $\sqrt{s_{NN}} = 2.76$ TeV

6.3.2 Z^0 Transverse momentum

The differential yield as a function of Z^0 transverse momentum is obtained with Eq 6.6. The HI data are plotted in the p_T range [0-36] GeV/c in figure 6.10. The data are shown in red dots with orange systematic uncertainties and black statistical uncertainties. The HI data points are placed in the mean p_T value within the corresponding bin. The data is compared to a POWHEGinterfaced-with-PYTHIA calculation. Within statistical uncertainties the POWHEG calculation scaled by the nuclear geometry agrees with the HI data.

$$\frac{d^2N}{dydp_T} = \frac{N_Z}{\alpha\epsilon N_{MB}} \cdot \frac{1}{\Delta y \Delta p_T} \tag{6.6}$$

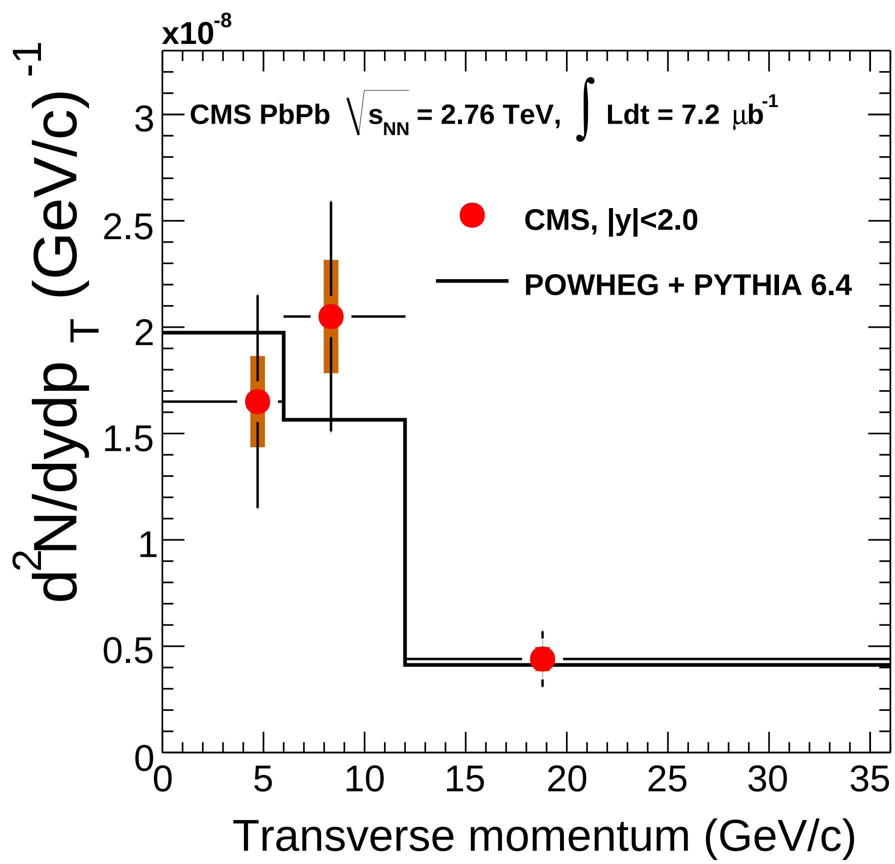

Figure 6.10: $p_T$distribution of Z candidates in $PbPb$ collisions at $\sqrt{s_{NN}} = 2.76$ TeV

6.3.3 High-p_T Z^0 event

In figure 6.10 one high-p_T (115.75 GeV/c) event falls out of range. By examining table .9, the mass is found to be 115.86 GeV/c^2 and the rapidity is found to be 0.41. Due to the nature of the event, a careful examination of the event was carried out. No jet was found in the opposite side in azimuth from the Z^0 candidate.

6.3.4 Z^0 yield vs N_{part} distribution

The differential yield divided by the overlap function is shown in figure 6.11 comparing the HI data to the same models described in section 6.3.1. The differential yield is divided by the overlap function, T_{AA}, in three centrality bins. The corresponding T_{AA} values are shown in table 6.6[61]. The HI data is shown in red dots with orange systematic uncertainties and black statistical uncertainties. Three centrality bins are shown and one minimum-bias bias point (hollow blue square). The points are placed at the average N_{part} value of the centrality bin. A slight difference is expected, ∼3% [48] from energy loss, from peripheral to central collisions. Within experimental uncertainties, the data is compatible with all the models scaled by the nuclear geometry(A^2/σ_{PbPb}).

Table 6.6: Nuclear overlap function.

centrality	0-100 %	0-10 %	10-30%	30-100%
T_{AA} $(1/\mu b^b)$	5.67± 0.30	23.2± 1.9	11.6± 0.6	1.45± 0.13

The differential yields as a function of rapidity and p_T are summarized in table 6.7. The results are divided in p_T, rapidity and centrality bins.

6.3.5 Z^0 R_{AA} with POWHEG

The nuclear modification factor, R_{AA}, was calculated at first making use of a POWHEG calculation in the same kinematical range as the HI data. The differential cross-section obtained from POWHEG is $d\sigma_{pp}/dy = 59.6\ pb$ in $|y| \leq 2.0$. The nuclear modification factor is calculated using Eq. 6.7. The minimum-bias R_{AA} is calculated to be 1.00±

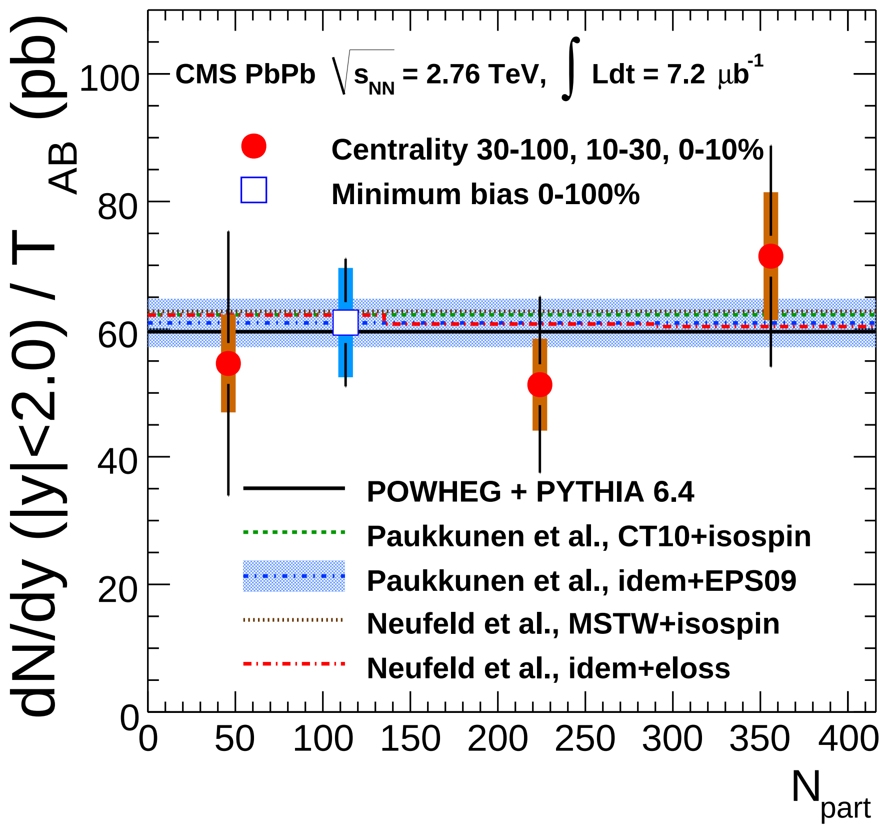

Figure 6.11: Number of participants distribution of Z candidates in $PbPb$ collisions at $\sqrt{s_{NN}}$ = 2.76 TeV

0.16(stat.) ± 0.16(sys.) in the $|y| \leq$2.0 range.

$$R_{AA} = \frac{dN_{AA}/dy}{T_{AA} \times d\sigma_{pp}/dy} \tag{6.7}$$

6.4 The *pp* Reference Sample

During the month of March 2011 a *pp* run was taken at $\sqrt{s}$= 2.76 TeV to be used as a reference sample for $PbPb$ measurements. The total integrated luminosity collected by CMS was 231 nb^{-1} with an associated uncertainty of 6% based on the analysis of data collected during a Van der Meer scan [79]. A total of 29 Z candidate events were found. A complete list of the Z candidates can be found in the appendix table 6.5. The Level-1

Table 6.7: Number of Z^0 candidates (N_Z) in each $|y|$, p_{T} and centrality interval. (second column) Associated yield dN/dy. The last column is the pp σ_{pp}/dy using POWHEG . For the p_{T} bins, $d^2N/dydp_{\mathrm{T}}$ and $(d\sigma^2_{pp}/dydp_{\mathrm{T}})$ are quoted instead, in units of per GeV/c. Quoted uncertainties are statistical then systematic.

$\|y\|$	N_Z	dN/dy $(\times 10^{-8})$	$d\sigma_{pp}/dy$ (pb)
$[0, 2.0]$	39	$33.8 \pm 5.5 \pm 4.4$	59.6
$[0, 0.5]$	13	$38.1 \pm 10.7 \pm 5.0$	65.1
$[0.5, 1.0]$	12	$35.6 \pm 10.4 \pm 4.6$	64.0
$[1.0, 2.0]$	14	$30.0 \pm 8.1 \pm 3.9$	55.0
$p_{\mathrm{T}}(GeV/\mathrm{c})$	N_Z	$d^2N/dydp_{\mathrm{T}}$ $(\times 10^{-8})$ [1/(GeV/c)]	$d\sigma^2_{pp}/dydp_{\mathrm{T}}$ [pb/(GeV/c)]
$[0, 6]$	11	$1.65 \pm 0.50 \pm 0.22$	3.48
$[6, 12]$	15	$2.05 \pm 0.54 \pm 0.27$	2.76
$[12, 36]$	12	$0.44 \pm 0.13 \pm 0.06$	0.73
Centrality	N_Z	dN/dy $(\times 10^{-8})$	$d\sigma_{pp}/dy$ (pb)
$[30, 100]\%$	7	$7.92 \pm 3.00 \pm 1.03$	59.6
$[10, 30]\%$	14	$59.5 \pm 16.0 \pm 7.7$	59.6
$[0, 10]\%$	18	$165 \pm 40 \pm 22$	59.6

triggers required slightly higher quality muon to cope with the higher collision rate than the one in *PbPb* collisions. From a comparison of the trigger efficiency in MC and data using the *tag-and-probe* method, a 2% systematic uncertainty is obtained [79]. The same offline event selection was applied as the one described in section 5.2.3 with the exception of the use of a more relaxed HF coincidence requirement of one 3 GeV tower, as opposed to three towers required in the *PbPb* case.

The data-set has been processed with the Heavy-Ion reconstruction software, as opposed to the one commonly used in *pp* collisions. The same *Acceptance* × *Efficiency* correction used in *PbPb* will be considered, only that in the *pp* case the correction obtained in the most peripheral bin in centrality is used.

Figure 6.12 shows the invariant mass reconstructed from the *pp* run at $\sqrt{s} = 2.76$

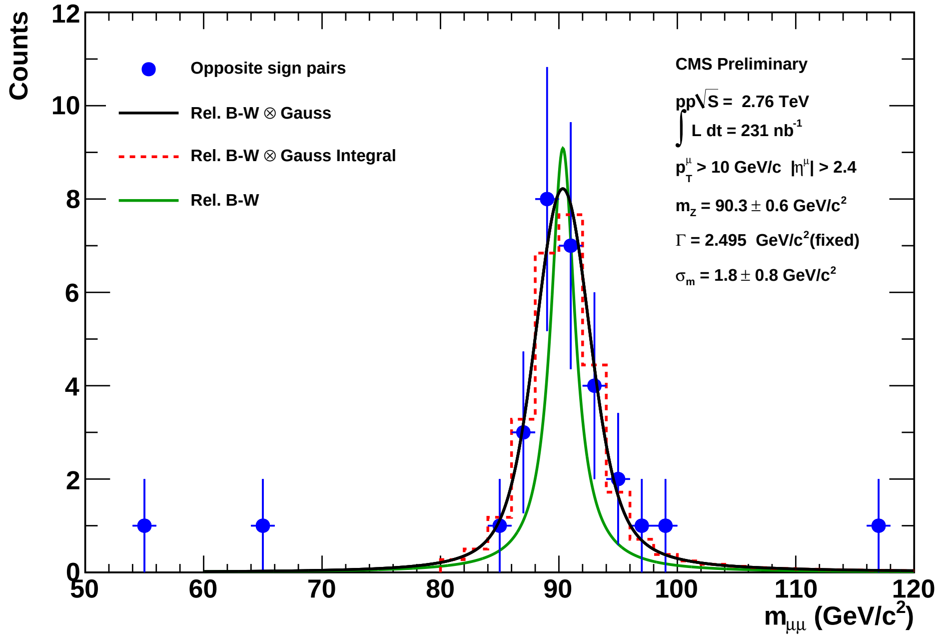

Figure 6.12: Invariant mass Z candidates in pp collisions at $\sqrt{s}$ = 2.76 TeV with fits, fit parameters listed for the BW convolved with a Gaussian.

TeV. The data points (blue dots) are shown with statistical error bars. Fits to the data are also overlaid, as already discussed in section 6.1.1. A Breit-Weigner fit (green line), with Γ fixed width, to 2.495 GeV/c^2, does not properly reproduce the mass resolution obtained from the HI reconstruction. A better approach is to use the BW convoluted with a Gaussian to account for the detector resolutions. It can be seen that there is no background in the mass range [50-120] GeV/c^2. A total of 29 candidates are found in the mass range [60-120] GeV/c^2.

6.4.1 Z^0 R_{AA} with *pp* data at $\sqrt{s_{NN}} = 2.76$ TeV

To calculate the nuclear modification factor from the data obtained in *pp* and *PbPb* it is necessary to obtain the yields in *PbPb* as in Eq. 6.8

$$\frac{1}{T_{AA}} \cdot \frac{d^2N}{dp_T dy} = \frac{1}{T_{AA}} \cdot \frac{1}{\Delta y \Delta p_T} \cdot \frac{N_Z}{\alpha \epsilon N_{MB}} \qquad (6.8)$$

while in pp the yield can be calculated using Eq. 6.9

$$\frac{d^2\sigma}{dp_T dy} = \frac{1}{\mathcal{L}_{pp}} \cdot \frac{1}{\Delta y \Delta p_T} \cdot \frac{N_Z}{\alpha\epsilon} \tag{6.9}$$

The form for the R_{AA} is given by Eq. 6.10.

$$R_{AA} = \frac{\mathcal{L}_{pp}}{T_{AA} N_{MB}} \cdot \frac{N^Z_{PbPb}}{N^Z_{pp}} \cdot \frac{\alpha\epsilon_{pp}}{\alpha\epsilon_{PbPb}} \tag{6.10}$$

To calculate the nuclear modification factor, comparing the yield in $PbPb$ with pp, some of the systematic uncertainties cancel out due to the use of the same reconstruction algorithm. The ones that do not cancel are the following:

- The luminosity uncertainty in pp collisions. This results in a global luminosity uncertainty of ± 6%
- Minbias event counting in $PbPb$ collisions. This results in a global uncertainty kept at ± 3%
- Background fitting in $PbPb$ collisions. Uncertainty on the background under the Z^0 peak, this is kept a one-sided -3%. The uncertainty in the pp case is negligible due to the minimal background.
- Isospin, shadowing and energy loss. This is kept at ± 3.2%
- Systematic uncertainty due to dimuon trigger efficiencies. A ± 2% uncertainty is assigned for dimuons [79].
- The inner tracking uncertainty is kept at ±1% Given the the same reconstruction algorithm was used, only the centrality dependent uncertainty is not canceled.

The total global systematic uncertainty is 6.7%. The overall systematic uncertainty on the measurement is calculated to be[+3.9% , - 4.9%.] The statistical uncertainty is found by adding in quadrature the uncertainties in pp (± 19%) and $PbPb$ (± 16%). The overall statistical uncertainty is ± 25%.

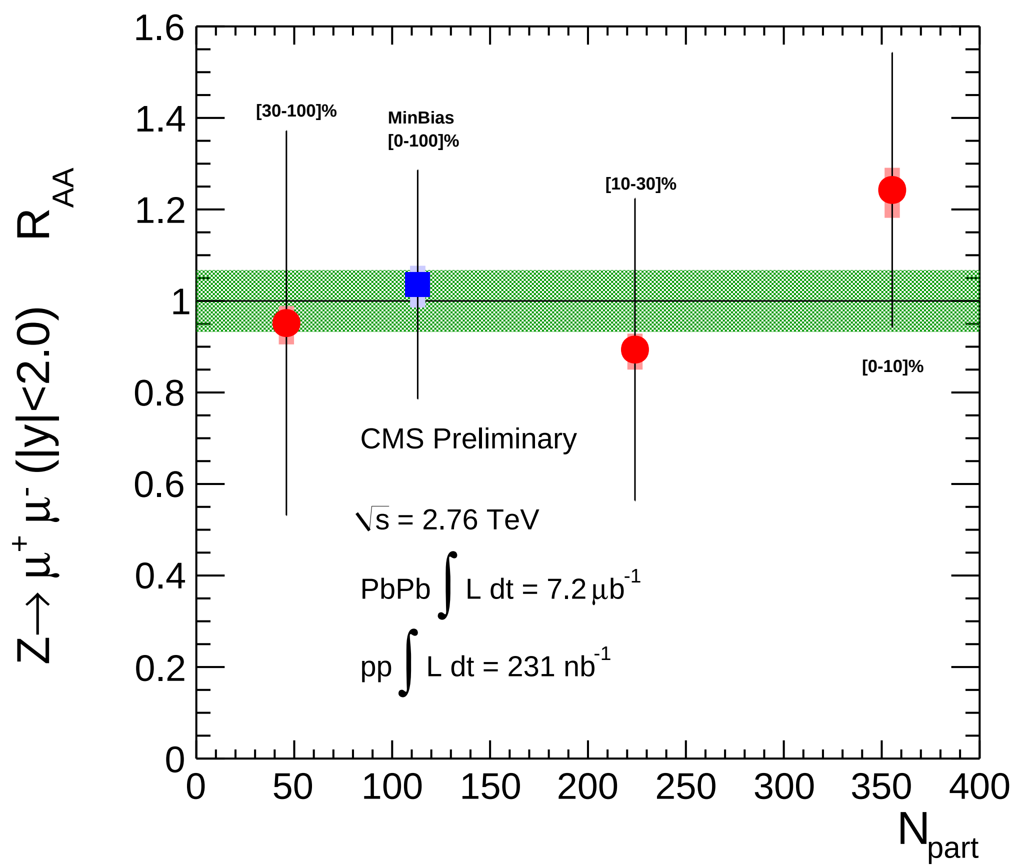

Figure 6.13: Nuclear modification factor as a function of N_{part} for $\mathrm{Z} \rightarrow \mu^+\mu^-$ at $\sqrt{s_{NN}} =$ 2.76 TeV

6.4.2 Results

The nuclear modification factor for the $\mathrm{Z} \rightarrow \mu^+\mu^-$ ($|y| \leq$2.0) at $\sqrt{s} = 2.76$ TeV is shown in Fig. 6.13. The points are shown with black statistical uncertainty bars. The systematic uncertainties are shown as red bars, and blue for the minimum-bias point. It can be seen that the R_{AA} does not have a N_{part} dependence as a function of centrality, within uncertainties. In each of the centrality bins the measurement is compatible with unity within measurement uncertainties. The data points are placed at the average N_{part} value within the centrality bin assigned. The minimum-bias value shows no nuclear modification for the $\mathrm{Z} \rightarrow \mu^+\mu^-$ decay, as expected. Given that there is no observed modification as a function of centrality, the $\mathrm{Z} \rightarrow \mu^+\mu^-$ channel can be established as a standard candle for hot nuclear effects.

Table 6.8: Nuclear overlap function.

centrality	0-100 %	0-10 %	10-30%	30-100%
R_{AA}	1.03	1.24	0.89	0.95
Statistical Uncertainty	25%	30%	33 %	42%
Systematics Uncertainty	[+4.0 - 5.0]%	[4.8 - 6.0]%	[+3.5 - 4.4]%	[+3.7 - 4.7]%

Figure 6.14 shows the R_{AA} as a function of the transverse mass, m_T, for the 0-10% most central collisions. Table 6.8 shows the R_{AA} values fro the different centrality classes, and the over-all value with statistical and systematic uncertainties. The plot shows the nuclear modification factor for isolated photons in CMS, as black dots with statistical uncertainties and yellow bands as systematic uncertainties. The R_{AA} for the Z $\rightarrow \mu^+\mu^-$ channel (blue square) with red systematic uncertainty bands is also shown. The R_{AA} for charged particles is also shown (hollow points) over a large range of m_T, with blue systematics uncertainties. A clear suppression of the charged particle is observed in *PbPb* collisions, while the electrweak probes remain unmodified, within measurement uncertainties, in the most central collisions.

6.5 Discussion

The first measurement by CMS of the Z^0 boson in Heavy-Ion collisions is presented. The Z boson differential yields as a function of y^Z, p_T^Z and N_{part} were calculated in *PbPb* collisions. The nuclear modification factor was obtained by using the *pp* reference run at $\sqrt{s_{NN}}$ = 2.76 TeV taken by CMS. The yields with respect to y^Z and p_T^Z were found to match the POWHEG *pp* calculation, scaled by the nuclear geometry. In other words, that the high-precision tune developed from *pp* collisions is able to reproduce the yields in *PbPb* collisions after scaling with the appropriate nuclear geometry, A^2/σ_{pp}. The yield as a function of N_{part} shows no dependence on the number of participants. This shows that in the Z $\rightarrow \mu^+\mu^-$ decay channel the yields measured per binary collision remain constant

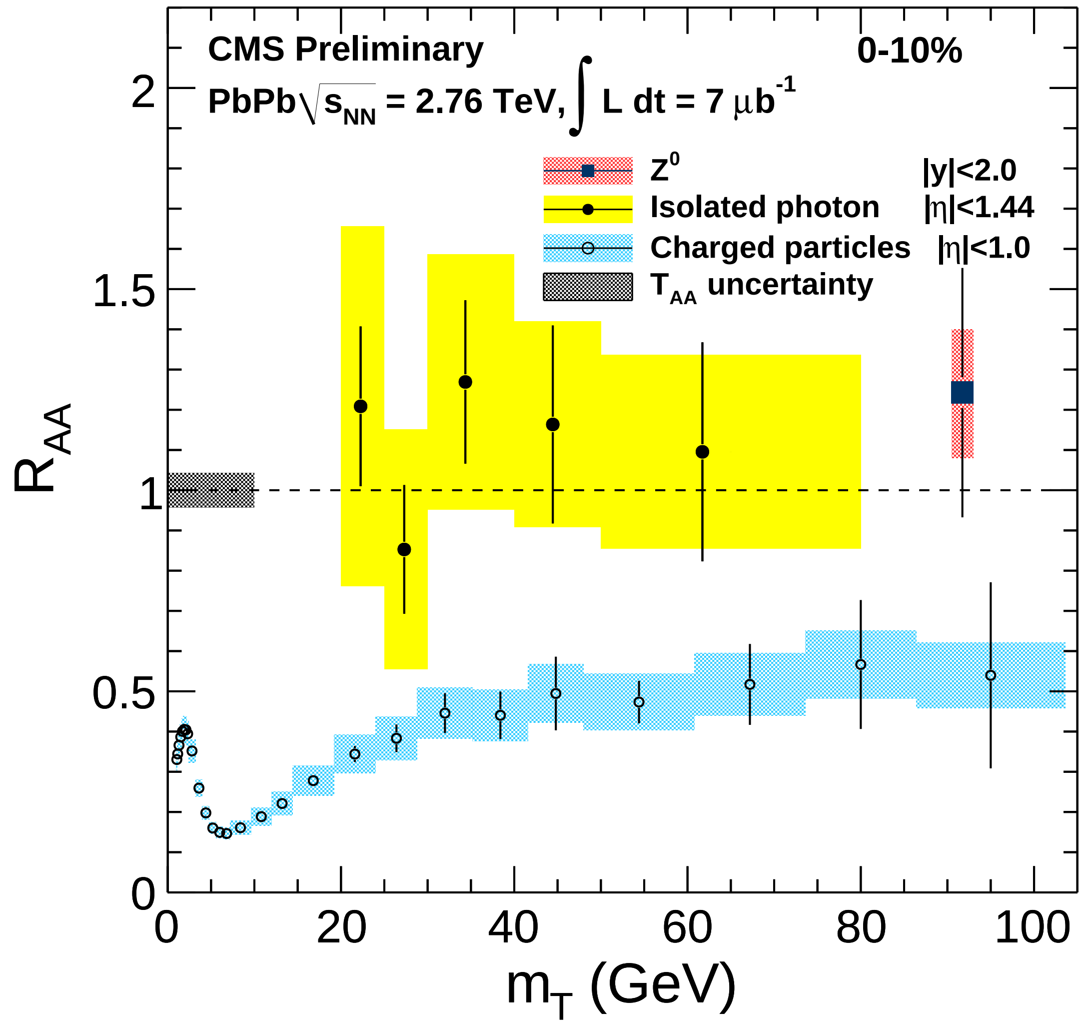

Figure 6.14: Nuclear modification factor of electromagnetic probe as a function of m_T in 0-10% most central events in CMS

from peripheral to central collisions. The observed yields were compared models which take into account subtler effects, e.g. modifications due to shadowing (10-20%) [47], isospin effects ($\sim$ 3%) [46] and energy loss ($\sim$ 2%) [48]. The statistical error bars are larger than the expected size of these modifications, precluding any further conclusions regarding their magnitude.

The nuclear modification factor was also calculated using the *pp* reference run at the same energy that the *PbPb* run. The R_{AA} was found consistent with unity in three different centrality classes, thus showing that there is no modification due to hot nuclear effects in the $Z \rightarrow \mu^+\mu^-$ channel.

Bibliography

[1] CMS Collaboration, CMS collaboration, Phys. Rev. Lett. **106**, 212301 (2011).

[2] Gargamelle: neutral current event, 1973.

[3] Physics Letters B **126**, 398 (1983).

[4] UA2 Collaboration, P. Bagnaia *et al.*, Phys.Lett. **B129**, 130 (1983).

[5] P. G. Langacker, (2000).

[6] Physics Reports **427**, 257 (2006).

[7] M. and Gell-Mann, Physics Letters **8**, 214 (1964).

[8] D. J. Gross and F. Wilczek, Phys. Rev. Lett. **30**, 1343 (1973).

[9] C.-Y. Wong, *Introduction to High-Energy Heavy-Ion Collisions* (World Scientific Pub Co Inc, 1994).

[10] Particle Data Group, K. N. et. al, J. Phys. G **37** (2010).

[11] Physics Letters B **86**, 243 (1979).

[12] CDF Collaboration, F. Abe, H. Akimoto and Akopian, Phys. Rev. Lett. **74**, 2626 (1995).

[13] D0 Collaboration, S. Abachi *et al.*, Phys. Rev. Lett. **74**, 2422 (1995).

[14] I. M. Dremin and A. V. Leonidov, Physics-Uspekhi **53**, 1123 (2010).

[15] D. d'Enterria, J.PHYS.G **34**, S53 (2007).

[16] E. V. Shuriak, Zhurnal Eksperimental noi i Teoreticheskoi Fiziki **74**, 408 (1978).

[17] D. Schwarz, Annalen der Physik **12**, 220 (2003).

[18] E. Iancu and R. Venugopalan, hep-ph/0303204.

[19] J. M. Maldacena, Adv. Theor. Math. Phys. **2**, 231 (1998), [hep-th/9711200].

[20] K. Kovtun, P. D. T. Son and A. O. Starinets, Phys. Rev. Lett. **94**, 111601 (2005).

[21] H. Liu, K. Rajagopal and U. A. Wiedemann, Phys. Rev. Lett. **97**, 182301 (2006).

[22] S. S. Gubser, Phys. Rev. D **74**, 126005 (2006).

[23] M. G. Alford, K. Rajagopal and F. Wilczek, Phys. Lett. **B422**, 247 (1998), [hep-ph/9711395].

[24] Z. Fodor and S. D. Katz, 0908.3341.

[25] J. D. Bjorken, Phys. Rev. D **27**, 140 (1983).

[26] T. Altherr and P. Ruuskanen, Nuclear Physics B **380**, 377 (1992).

[27] R. Averbeck, Journal of Physics G: Nuclear and Particle Physics **30**, S943 (2004).

[28] J. Seixas *et al.*, Journal of Physics G: Nuclear and Particle Physics **34**, S1023 (2007).

[29] S. Campbell and the PHENIX Collaboration, Journal of Physics G: Nuclear and Particle Physics **34**, S1055 (2007).

[30] T. Matsui and H. Satz, Physics Letters B **178**, 416 (1986).

[31] A. Mócsy and P. Petreczky, Phys. Rev. Lett. **99**, 211602 (2007).

[32] R. Vogt, Phys. Rev. C **81**, 044903 (2010).

[33] X. Zhao and R. Rapp, Nuclear Physics A **859**, 114 (2011).

[34] X. Zhao and R. Rapp, Phys. Rev. C **82**, 064905 (2010).

[35] A. Andronic, P. Braun-Munzinger, K. Redlich and J. Stachel, Nuclear Physics A **789**, 334 (2007).

[36] L. Yan, P. Zhuang and N. Xu, Phys. Rev. Lett. **97**, 232301 (2006).

[37] S. C. J. Adams, NUCL.PHYS.A **757**, 102 (2005).

[38] R. Vogt, *Ultrarelativistic heavy-ion collisions* (Elsevier, 2007).

[39] E. Iancu and R. Venugopalan, hep-ph/0303204.

[40] T. Hirano, U. Heinz, D. Kharzeev, R. Lacey and Y. Nara, Physics Letters B **636**, 299 (2006).

[41] D. d'Enterria *et al.*, *CMS Physics: Technical Design Report v.2: Addendum on High Density QCD with Heavy Ions*, Technical Design Report CMS Vol. 34 (CERN, Geneva, 2007), revised version submitted on 2007-03-15 12:08:08.

[42] D. d'Enterria and the CMS Collaboration, Journal of Physics G: Nuclear and Particle Physics **35**, 104039 (2008).

[43] PHENIX Collaboration, S. S. Adler *et al.*, Phys. Rev. C **69**, 034909 (2004).

[44] PHENIX Collaboration, S. S. Adler *et al.*, Phys. Rev. Lett. **94**, 232301 (2005).

[45] R. Neufeld, I. Vitev and B.-W. Zhang, 1010.3708.

[46] H. Paukkunen and C. Salgado, Journal of High Energy Physics **2011**, 1 (2011), 10.1007/JHEP03(2011)071.

[47] R. Vogt, Phys. Rev. C **64**, 044901 (2001).

[48] R. B. Neufeld, I. Vitev and B.-W. Zhang, Phys. Rev. C **83**, 034902 (2011).

[49] L. Evans and P. Bryant, Journal of Instrumentation **3**, S08001 (2008).

[50] L. Evans and P. Bryant, Journal of Instrumentation **3**, S08001 (2008).

[51] D. Acosta, editor, *CMS Physics Technical Design Report Volume I: Detector Performance and Software*Technical Design Report CMS (CERN, Geneva, 2006), There is an error on cover due to a technical problem for some items.

[52] R. Brauer and K. Klein, CERN Report No. CMS-NOTE-2005-025. CERN-CMS-NOTE-2005-025, 2005 (unpublished).

[53] CMS collaboration, *The CMS muon project: Technical Design Report*Technical Design Report CMS (CERN, Geneva, 1997).

[54] J. Hauser, Nuclear Instruments and Methods in Physics Research Section A: Accelerators, Spectrometers, Detectors and Associated Equipment **384**, 207 (1996), BEAUTY '96.

[55] R. Santonico and R. Cardarelli, Nuclear Instruments and Methods in Physics Research **187**, 377 (1981).

[56] Y.-J. L. L. Bagby, A. J Bell and G. Veres, CERN Report No. 018, 2010 (unpublished).

[57] I. Lokhtin and A. Snigirev, The European Physical Journal C - Particles and Fields **45**, 211 (2006), 10.1140/epjc/s2005-02426-3.

[58] M. Hildreth, Instructions for using the datamixingmodule, https://twiki.cern.ch/twiki/bin/view/CMS/DataMixer, 2011.

[59] G. Cerati, Track reconstruction sequences, https://twiki.cern.ch/twiki/bin/view/CMSPublic/SWGuid 2011.

[60] CMS collaboration, CMS Internal Note (2007).

[61] CMS collaboration, Internal Note (2010).

[62] R. Wilkinson and P. T. Cox, CERN Report No. CMS-NOTE-2001-013, 2001 (unpublished).

[63] G. Bruno *et al.*, CERN Report No. CMS-NOTE-2002-043, 2002 (unpublished).

[64] R. Brun, Root reference guide, http://root.cern.ch/root/html/TMath.html#TMath:Prob, 2011.

[65] CMS collaboration, CMS Analysis Note 2009/111 (2009).

[66] CMS collaboration, *CMS TriDAS project: Technical Design Report; 1, the trigger systems*Technical Design Report CMS (Technical Design Report CMS ; 6, 2000).

[67] CMS collaboration, CMS Analysis Note 2010/399 (2010).

[68] M. R. P. Billoir, R. Frhwirth, Nucl. Instr. and Meth **A241**, 115 (1985).

[69] C. Campagnari and D. Kovalsky, Software guide tracker muons, https://twiki.cern.ch/twiki/bin/view/CMSPublic/SWGuideTrackerMuons, 2011.

[70] G. Abbiendi, N. Adam, J. Alcaraz et al., CMS Analysis Note 2008/097. (2008).

[71] M. Mulders, I. Bloch, E. James et al., CMS Analysis Note 2008/098 (2008).

[72] T. VBTF, CMS Analysis Note 2010/116 (2010).

[73] T. Sjöstrand, S. Mrenna and P. Skands, JHEP **026** (2006), [hep-ph/0603175].

[74] CMS collaboration, Journal of High Energy Physics **2011**, 1 (2011), 10.1007/JHEP01(2011)080.

[75] G. Breit and E. Wigner, Phys. Rev. **49**, 519 (1936).

[76] CMS collaboration, Internal Note (2011).

[77] S. Frixione and B. R. Webber, Journal of High Energy Physics **2002**, 029 (2002).

[78] K. Eskola, H. Paukkunen and C. Salgado, Journal of High Energy Physics **2009**, 065 (2009).

[79] CMS collaboration, Internal Note (2011).

Appendices

Table .9: List of all Z candidates. Cent corresponds to the centrality bin (0 most central)

runN	LS	eventN	Z mass	Z p_T	Z y	cent	η^{μ_1}	η^{μ_2}	$p_T^{\mu_1}$	$p_T^{\mu_1}$	$\delta(\phi)$
150590	183	776435	93.07	14.61	-1.28	5	-2.28	-0.38	29.67	33.77	2.70
151020	212	998915	87.83	16.75	-1.08	6	-2.29	-0.31	21.46	38.17	3.18
151027	663	2714491	88.69	6.95	-0.24	12	-0.66	0.16	39.52	42.52	2.99
151058	230	1189276	91.77	1.47	-1.42	11	-1.93	-0.91	40.80	40.13	3.17
151058	437	2407858	89.27	7.47	-0.19	10	-0.60	0.20	39.87	42.97	2.98
151059	19	100429	82.47	11.99	-0.88	1	-0.77	-1.02	46.30	36.41	3.31
151088	57	350321	87.23	4.78	-1.59	3	-2.00	-1.22	38.43	42.64	3.20
151211	126	676548	88.23	5.09	1.69	11	1.96	1.45	40.82	44.74	3.07
151240	16	85452	91.76	6.08	1.03	0	1.58	0.43	41.33	37.38	3.26
151240	213	1123319	92.80	6.38	-0.26	17	0.35	-0.95	41.21	35.29	3.20
151353	127	715443	85.08	18.30	-0.78	0	-1.28	-0.24	39.83	36.56	2.67
151968	78	450797	90.05	13.82	0.12	10	0.84	-0.54	35.03	38.01	3.51
152112	170	804963	87.34	6.63	-0.14	6	0.61	-0.82	32.57	36.62	3.29
152112	527	2734474	94.77	7.74	1.68	0	1.64	1.72	46.05	48.96	2.99
152112	596	3092518	87.36	5.54	-0.62	3	-0.40	-0.83	40.50	45.03	3.07
152113	533	2789077	98.50	21.36	-1.43	7	-2.12	-0.29	46.26	25.05	3.07
152349	107	385577	90.44	27.95	0.64	3	1.10	-0.18	52.02	27.32	2.79
152431	353	1883516	89.01	7.94	-1.48	0	-1.44	-1.52	47.25	42.04	3.01
152474	127	608700	89.07	11.00	-0.87	1	-0.78	-0.98	46.49	42.82	2.91
152561	355	1965024	91.98	5.24	1.13	0	2.28	-0.02	26.55	26.60	3.34
152592	131	788491	90.85	4.12	-0.75	0	-1.84	0.34	27.42	27.61	3.29
152592	308	1820803	99.71	5.78	1.01	0	1.08	0.93	50.52	49.08	3.03
152601	122	528278	115.86	115.75	0.41	1	1.10	0.13	41.84	107.27	1.55
152602	92	568075	91.59	11.01	0.87	7	1.26	0.56	38.11	48.83	3.08
152602	328	1969397	76.82	23.70	-0.26	5	-0.44	-0.00	45.59	32.93	2.62
152602	647	3744192	93.69	13.33	0.78	2	1.47	0.27	33.64	46.49	3.05
152625	273	1587545	93.54	8.91	-0.09	6	-1.04	0.68	29.48	38.24	3.09
152625	530	2989029	91.45	10.39	0.48	14	1.45	-0.79	32.69	22.30	3.14
152641	173	1020942	91.33	2.71	1.36	3	2.11	0.60	35.71	34.65	3.21
152642	477	2861862	90.02	6.21	0.35	15	1.27	-0.71	32.27	26.81	3.04
152652	90	347872	82.39	12.53	-1.40	9	-1.67	-1.07	43.66	36.05	2.89
152705	55	211752	76.46	14.78	0.25	1	2.11	-0.87	10.85	24.97	2.88
152722	115	722609	84.19	7.59	-0.74	16	-1.12	-0.42	36.09	43.47	3.10
152745	628	3636927	92.22	5.99	-0.86	1	-2.22	0.35	21.87	25.78	3.33
152751	230	1213764	91.23	5.30	1.82	16	2.11	1.52	45.40	42.10	3.05
152785	282	1586972	91.05	8.82	-0.28	2	0.01	-0.60	45.29	42.07	2.95
152785	265	1485142	93.76	17.85	-0.96	7	-1.31	-0.72	36.85	54.66	3.17
152957	134	829320	91.57	5.81	-0.36	12	-0.11	-0.62	45.22	43.66	3.02
152957	575	3532156	90.55	31.18	-0.71	4	-1.59	0.86	38.20	16.66	2.22

Table .10: List of all Z candidates

runN	LS	eventN	Z mass	Z p_T	Z y	cent	η^{μ_1}	η^{μ_2}	$p_T^{\mu_1}$	$p_T^{\mu_1}$	$\delta(\phi)$
891	17639301	161366	89.62	5.11	0.23	-1	1.24	-0.91	29.34	25.32	3.02
1175	108516259	161439	89.88	6.94	0.11	-1	0.76	-0.66	39.08	32.36	3.09
1490	112886783	161439	99.74	13.43	1.28	-1	1.94	0.40	45.26	31.91	3.18
4363	1472661	161454	89.79	2.20	1.97	-1	2.21	1.713	44.46	42.55	3.11
4653	2054342	161473	91.37	10.54	0.96	-1	0.50	1.48	43.75	38.16	2.92
5030	4937589	161473	89.49	6.16	-0.19	-1	0.69	-1.17	32.37	28.72	2.97
5137	5758592	161473	84.69	7.66	-0.62	-1	0.16	-1.56	33.98	27.08	3.03
5753	10561994	161473	65.01	20.20	0.26	-1	-0.49	1.43	29.47	16.82	2.41
8536	20253173	161474	91.30	4.10	-1.26	-1	-0.36	-2.19	32.32	30.73	3.02
9870	5142488	161396	86.68	7.89	-0.84	-1	-0.69	-1.02	46.86	39.00	3.15
9930	5754687	161396	86.21	7.34	-1.60	-1	-2.21	-0.91	38.00	33.13	2.98
11688	46355453	161474	117.07	6.89	-0.70	-1	-1.33	0.01	50.90	44.11	3.16
12584	54920550	161474	88.42	46.33	0.34	-1	0.05	1.06	66.03	24.41	2.62
12811	8617541	161366	88.96	1.91	0.53	-1	-1.02	2.18	18.11	16.34	3.10
13422	1643178	161439	89.71	6.01	0.98	-1	-0.06	2.11	28.55	25.78	2.94
14284	8882716	161439	92.02	17.60	-0.22	-1	0.40	-1.11	43.83	28.70	2.88
15311	17168095	161439	91.12	16.48	-0.06	-1	-1.02	1.07	32.29	25.59	2.61
15426	18235512	161439	91.09	4.51	-0.63	-1	0.62	-2.02	24.56	20.76	3.03
17114	32323618	161439	95.43	2.62	-0.07	-1	-1.70	1.57	17.89	17.86	2.99
17444	35437261	161439	87.93	6.37	-0.10	-1	0.59	-0.88	36.73	31.83	3.26
18774	47271486	161439	97.46	73.67	0.74	-1	0.57	1.25	88.50	28.55	4.02
19565	53826449	161439	91.11	29.88	-0.50	-1	-0.71	-0.10	59.55	32.30	3.42
20815	66003581	161439	92.23	47.68	1.12	-1	1.22	0.82	74.80	27.39	3.25
21120	68948418	161439	89.34	23.13	-0.05	-1	-0.86	1.37	38.91	18.10	2.75
21202	69949862	161439	92.90	30.64	1.69	-1	2.33	0.30	48.71	18.20	3.04
21878	76402031	161439	90.25	13.93	1.20	-1	1.74	0.43	44.47	30.56	3.16
21928	77020280	161439	91.31	7.44	1.85	-1	2.23	1.42	45.06	39.59	3.02
22153	79513631	161439	93.15	10.71	1.75	-1	1.95	1.51	48.88	42.71	3.33
23620	94269250	161439	95.64	32.65	1.67	-1	1.56	1.78	52.39	48.05	3.79